Optical Characterization and Fabrication of Transparent Y2O3 and (Gd,Lu)3Al5O12 Ceramics by Spark Plasma Sintering

李, 址煥

https://hdl.handle.net/2324/4784654

出版情報：Kyushu University, 2021, 博士（工学）, 課程博士
バージョン：
権利関係：

Ph. D. Thesis

放電プラズマ焼結による透光性 Y_2O_3 及び $(Gd, Lu)_3Al_5O_{12}$ セラミックスの作製と光学的特性評価

Optical Characterization and Fabrication of Transparent Y_2O_3 and $(Gd,Lu)_3Al_5O_{12}$ Ceramics by Spark Plasma Sintering

Department of Applied Science for Electronics and Materials
Interdisciplinary Graduate School of Engineering Sciences
Kyushu University

李 址煥
LEE JI HWOAN

Supervisor: Prof. Byung-Koog Jang

January, 2022

博士学位論文

放電プラズマ焼結による透光性 Y_2O_3 及び $(Gd, Lu)_3Al_5O_{12}$ セラミックスの作製と光学的特性評価

Optical Characterization and Fabrication of Transparent Y_2O_3 and $(Gd,Lu)_3Al_5O_{12}$ Ceramics by Spark Plasma Sintering

九州大学
大学院総合理工学府
量子プロセス理工学専攻

李 址煥
LEE JI HWOAN

指導教員： 張 炳國

2022 年　1 月

論文調査委員会

主査　九州大学　教授　張　炳國
副査　九州大学　教授　波多　聰
副査　九州大学　教授　島ノ江　憲剛

Abstract

As the representative transparent ceramic phosphors, sesquioxide ceramics (Y_2O_3, Lu_2O_3, and Sc_2O_3) and rare-earth aluminum garnets ($RE_3Al_5O_{12}$) have received significant attention as promising host materials for high-power solid-state lasers and scintillators. The characteristics of the spark plasma sintering (SPS) process, such as densification using an electric field and short sintering time, suppress the microstructure coarsening and act as a strength to achieve high transparency, so it is a very promising sintering technology in the fabrication of transparent ceramics. However, further research is required in the SPS process to solve the non-uniform sintering behavior and carbon contamination and simultaneously achieve microstructure control and high transparency. The main purpose of this thesis is that the SPS process with high sinterability is applied to transparent Y_2O_3 and $RE_3Al_5O_{12}$ ceramics to improve optical and microstructural characteristics. The densification behavior of the SPS process is investigated to decrease the sintering temperature and suppress the microstructure coarsening. Interpretation of the observed non-uniform sintering behavior and microstructure contributed significantly to examining the densification behavior of the SPS process. Research on the sintering parameters (heating rates, holding times, and loading schedule) and two-step profiles (heating and loading schedules) during the SPS process is also performed for achieving the improvement in optical and microstructural characteristics. The following is the accomplishment of this thesis.

In chapter 1, the general introduction of this study was presented. The background information to help understand the transparent ceramic materials such as Y_2O_3 and $RE_3Al_5O_{12}$ used as the starting materials and the SPS technology with FAST are included. In particular, the motivation and final objectives of this study and the main purpose of each chapter were briefly summarized.

In chapter 2, during SPS of Y_2O_3 ceramics, the evolution of non-uniform microstructure was observed, depending on the heating rate. At high heating rates, the sintered samples are apparently non-uniform to reveal opaque center and translucent periphery, and a difference in the grain size between the center and the periphery increases remarkably. The porosity and the pore size in the center also increase with increasing the holding times. The non-uniform microstructure is explained by using a concept of dynamic grain growth and defect diffusion from the periphery to the center under complicated electric field effects during SPS.

In chapter 3, transparent Y_2O_3 ceramics were successfully fabricated by SPS applying two-step pressure and heating profiles. After the first-step SPS at 1250°C, the second-step SPS, which had the highest transmittance, was completed at 1500°C. The two-step SPS improved the shrinkage behavior and was able to achieve sufficient densification without excessive coarsening. As a result, the transmittance was 80.6% at 1100 nm, which is close to the theoretical transmittance of 81.6%. The two-step SPS revealed a significant advantage in manufacturing ceramics that were transparent and had sufficient densification.

In chapter 4, during the SPS process of transparent Ce^{3+}:$(Gd,Lu)_3Al_5O_{12}$ ceramics, due to the carbon-rich environment with graphite components, it is known that carbon contamination and oxygen vacancies are introduced. The introduction of carbon contamination and oxygen vacancies directly affected the transmittance, and the annealing process mostly recovered the low transmittance of sintered samples. It also affected the luminescence characteristics to be reduced. Through the SPS process, consequently, the sintered samples were effectively densified, and the annealing could compensate for the drawback of SPS and enable better photoluminescence characteristics.

In chapter 5, transparent Ce^{3+}:$(Gd,Lu)_3Al_5O_{12}$ were fabricated by two-step SPS with microstructure control. The heating rate was changed from 50 to 5°C/min in two-step SPS at first-step temperature. At the initial stage of shrinkage, the holding time of the first-step SPS could induce densification by suppressing the coarsening. Compared with the single-step SPS, the two-step SPS showed a smaller grain size, and the grain size tended to decrease with decreasing the first-step temperature. The porosity was also lower than single-step SPS, and the lowest porosity was obtained at the first-step temperature of 1000°C, the starting point of shrinkage. The microstructure control of two-step SPS revealed the most improved transmittance in specimen TS-1000, and transmittance at 1000 nm was increased from 50.1% (SS-1250) to 56.5% (TS-1000).

The comprehensive experimental results and conclusions of each chapter of the Ph.D. thesis are summarized **in chapter 6**.

List of Figures

List of Tables

Contents

Chapter 1. General Introduction

1.1. Backgrounds

Conventional transparent materials include glasses, polymers, and alkali hydrides, all of which showed mechanical and chemical instability. Single crystals of some ceramics reveal optical transparency, and these are much stronger and more stable than their conventional counterparts. However, the fabrication of single crystals is usually called “growth” as it is mainly controlled by thermodynamic processes that are relatively slow. Furthermore, growing large single crystals is often challenging, especially for oxide materials with extremely high melting points, and the as-grown single crystals cannot be directly used because the growth process determines their shapes. Consequently, polycrystalline transparent ceramics have emerged as promising candidates to replace their single-crystal counterparts because of their outstanding advantages, including low cost, largescale production, malleability, and high mechanical properties. However, in polycrystalline transparent ceramics, the optical transparency is usually dependent on the extent of light scattering, as shown in Fig. 1.

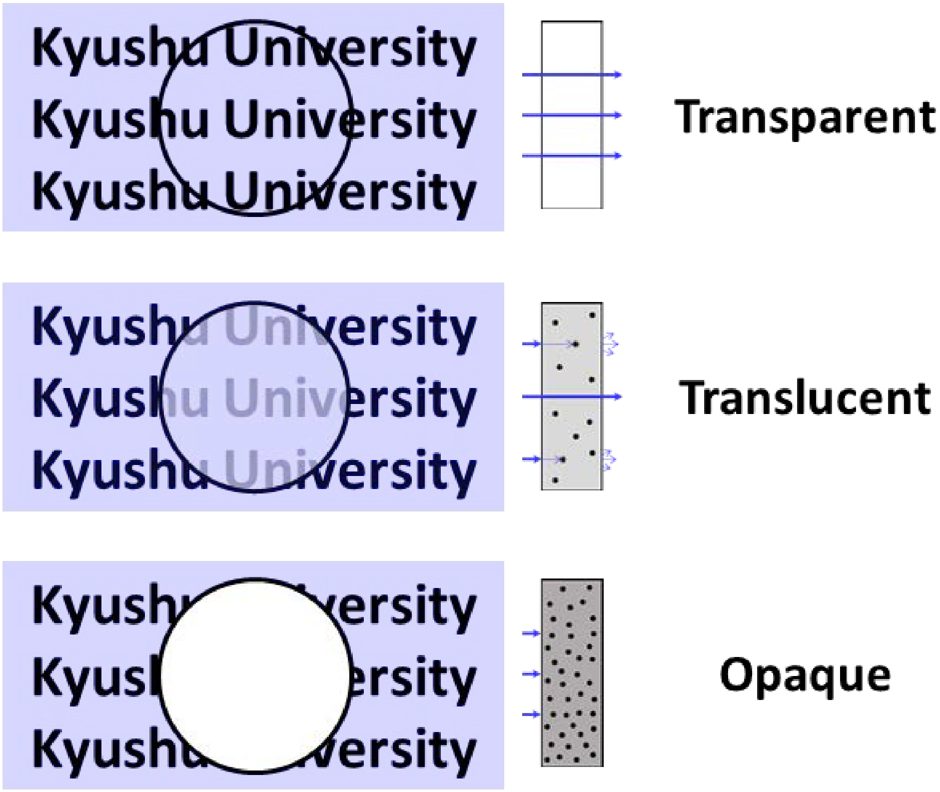

Fig. 1. Schematic diagram of optical transparency depending on the extent of light scattering by defects in polycrystalline transparent ceramics.

Microstructures of the polycrystalline ceramics have more sources of light scattering than single crystals, such as pores, grain boundaries, impurities, and birefringence effects, schematically summarized in Fig. 2 [1]. Of the factors that contribute to light scattering, scattering by pores is the main contributor to light attenuation in transparent ceramics. Near the surface of pores, light is reflected and refracted by both trapped air and the ceramic material, which has different optical properties. Therefore, porous ceramics are not transparent, whether the pores are inter-grained or intra-grained. Of the two-pore types, intra-grained pores are more challenging to remove, and their formation is closely related to the quality of the precursor powders, especially when using hard agglomerates.

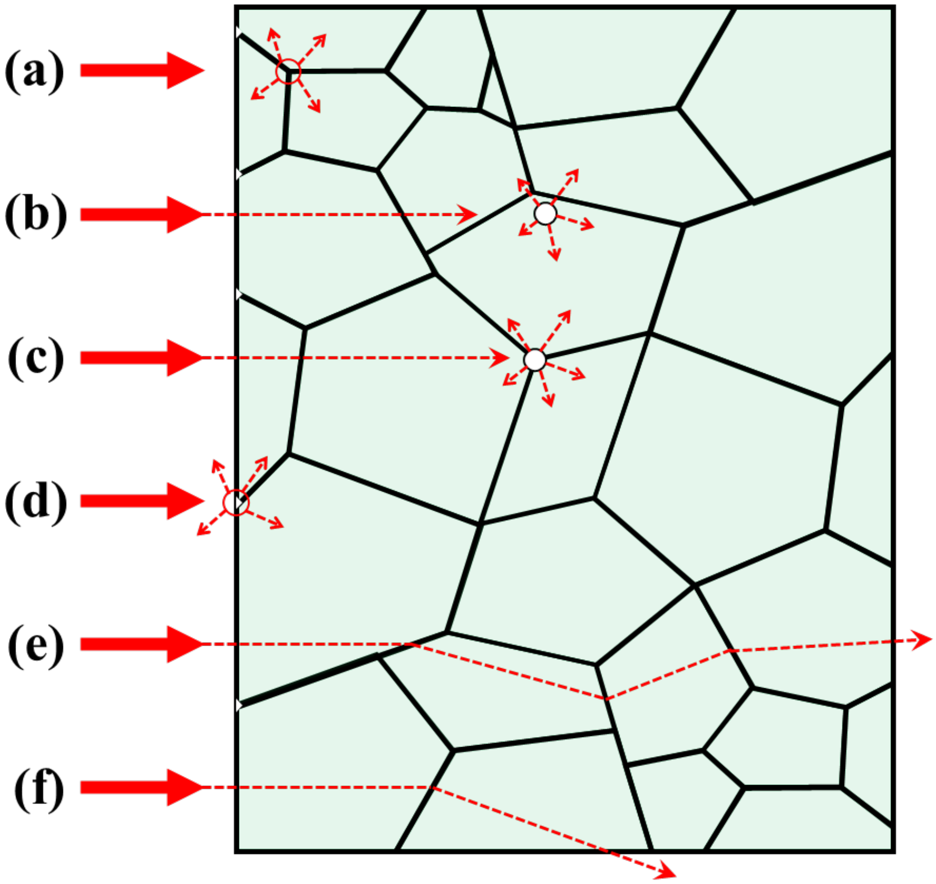

Fig. 2. Factors of light scattering in polycrystalline transparent ceramics. (a) Grain boundaries, (b) intra-granular pores, (c) inter-granular pores, (d) surfaces, and (e,f) refraction by grain boundaries by birefringence effects.

In ceramics, grains and grain boundaries are likely to have different properties; thus, interfaces act as scattering sources. Because grains are the main phase of ceramics, the properties of grain boundaries play a significant role in determining the transparency of ceramics, and thus controlling the quality of grain boundaries is an important strategy for achieving high optical transparency. Moreover, impurities are often located at grain boundaries, which increases the difference between the grains and boundaries and causes further light scattering. Therefore, precursor materials should have sufficiently high purities. However, when using sintering aids, there is a competitive effect between densification and the impurity concentration that should be optimized. Generally, the amount of sintering aids added to transparent ceramics is much lower than ceramics for other applications with requisite mechanical and electrical properties.

Not all materials can be used to make transparent ceramics as the grains in ceramics with low symmetric structures are optically anisotropic, which causes light to scatter when it travels across the grain boundaries. Therefore, as shown in Table 1, transparent ceramic materials must have highly symmetric crystal structures; the majority of transparent ceramics have a cubic system [2–4], and some materials with tetragonal and hexagonal structures can also be made into transparent ceramics, although these are more difficult to process. Consequently, the development of transparent ceramics is an important and exciting research topic [5].

Table 1. Representative transparent oxide ceramics and some of their basic physical properties.

Chemical Formula	**Crystal Structure**	**Lattice Constant (Å)**	**W_m**	**Density (g/cm^3)**	**T_m(°C)**	**T_b(°C)**	**Ref.**
Al_2O_3	Hexagonal	$a = 4.754$, $c = 12.99$	101.69	3.60	2054	2980	[6]
MgO	Cubic	$a = 4.217$	40.30	3.59	2852	3600	[7]
ZrO_2	Monoclinic (RT) / Tetragonal (> 1100°C) / Cubic (> 1900°C)	$a = 5.143$, $b = 5.194$, $c = 5.298$, $\beta = 99.218°$ / $a = 5.094$, $b = 5.174$ / $a = 5.105$	123.22	5.85	2680	4300	[8]
Y_2O_3	Cubic	$a = 10.6$	225.81	5.01	2430	4300	[9]
Sc_2O_3	Cubic	$a = 9.84$	138.20	3.86	2403	–	[10]
Lu_2O_3	Cubic	$a = 10.393$	397.93	9.42	2510	–	[11]
$Y_3Al_5O_{12}$	Cubic	$a = 12.02$	593.70	4.55	1950	–	[12]
$MgAl_2O_4$	Cubic	$a = 8.08$	142.26	3.60	2250	–	[13]

1.2. Transparent Ceramic Materials

1.2.1. Yttria (Y_2O_3)

Y_2O_3 ceramics have outstanding physical and chemical properties, such as excellent thermal conductivity (13.6 W/m·K at 25°C) and corrosion resistance, and transparent Y_2O_3 ceramics have inherent optical properties, which include a wide range of transparent wavelengths (0.2–8 μm) and a refractive index of approximately 1.935 [14]. Since Y_2O_3 has a cubic crystal structure with high symmetry, as shown in Fig. 3, it has the advantage of achieving optical transparency. Compared to yttrium aluminum garnet (YAG), Y_2O_3 is more promising as a scintillator because of its highly effective atomic number and high density [15]. Furthermore, Y_2O_3 is more suitable for high-power solid-state laser applications than YAG because it has higher thermal conductivity and a lower thermal expansion coefficient [16]. Potential applications of transparent Y_2O_3 ceramics also include IR domes, gas nozzles, refractory materials, semiconductor components, and NIR-visible upconverters [17–19]. Representative research reported on transparent Y_2O_3 ceramics are listed in Table 2.

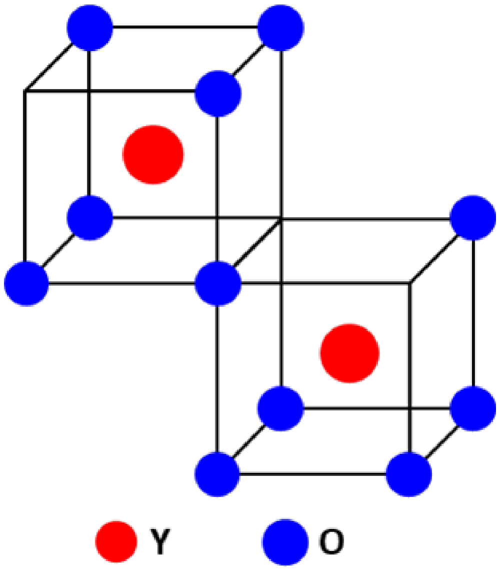

Fig. 3. Cubic crystal structure of Y_2O_3 ceramics with high symmetry.

Table 2. Sintering parameters and optical transmittance of representative research on transparent Y_2O_3 ceramics.

Powder Processing	**Sintering Parameters**	**Transmittance**	**Ref.**
Y_2O_3 from precipitation	Calcination: 1050°C/4 h, Pre-sintering: 1700°C/10°C/min, HIP: 1300°C/3 h/206 MPa	70% at 600 nm	[21]
Y_2O_3 from precipitation of carbonate	Calcination: 1100°C/4 h/3°C/min, Vacuum sintering: 1700°C/4 h/Vacuum:10^{-3} Pa	79% at 600 nm	[22]
Eu^{3+}:Y_2O_3 (0–5 at%) solid-state reaction	HP: 1580°C/8 h Pressure: 40 MPa	70% at 600 nm	[23]
Y_2O_3 commercial powder	CIP: 200 MPa, Pre-sintering: 1650°C/3 h/15°C/min, HIP: 1625°C/3 h/200 MPa	80% at 600 nm	[25]
Y_2O_3 commercial powder	HP: 1300–1550°C/3 h/20 MPa, HIP: 1450°C/5 h/180 MPa/Ar	83% at 1100 nm	[26]
Y_2O_3 commercial powder	SPS: 950–1050°C/0–8 h/2°C/min	55% at 1000 nm	[28]
Yb^{3+}:Y_2O_3 (0–50 at%) powder	SPS: 1250°C/1 h/82.7 MPa	78% at 1000 nm	[29]

Transparent Y_2O_3 ceramics were first reported 50 years ago [20]. These initial samples were obtained by hot-pressing under vacuum at 950°C and around 70–80 MPa for two days. Lithium fluoride was used as the sintering aid to ensure full densification of the ceramics and was eliminated during the sintering process. The optical transmittance of the HP-derived transparent Y_2O_3 ceramics was very close to that of single crystals. Transparent Y_2O_3 ceramics have been fabricated by pressure-less sintering in a vacuum or H_2 atmosphere [21,22]. For example, Saito et al. developed a simple method to synthesize Y_2O_3 powder with high sinterability, from which transparent ceramics could be obtained without the use of sintering aids [22]. This highly reactive Y_2O_3 powder was derived from fine, needle-shaped yttrium carbonate, synthesized by the precipitation of yttrium nitrate. After yttrium carbonate was calcined at 1100°C, the resultant Y_2O_3 powder had an average particle size of 0.1 μm and a small agglomeration size of 0.3 μm. Transparent Y_2O_3 ceramics were obtained by sintering at $\geq$ 1600°C, and while abnormal grain growth was not present, the optical transparency was still much lower than that of single crystals.

Transparent Y_2O_3 ceramics have also been fabricated using advanced sintering technologies, such as hot press (HP) [23,24], hot isostatic press (HIP) [25–27], and spark plasma sintering (SPS) [28–32]. For example, transparent Eu^{3+}-doped Y_2O_3 ceramics were developed without using sintering aids by HP at 40 MPa and 1580°C, which was determined to be the optimal sintering temperature [23]. While no sintering aid was added, the Eu dopant served as a sintering aid by controlling the ionic diffusivity and thus promoting the densification of Y_2O_3. As the concentration of Eu was increased from 0 to 5 at%, the optical attenuation and optical transmittance gradually decreased and increased, respectively.

Considerable research combined vacuum sintering with HIP to obtain transparent Y_2O_3 ceramics from a commercial powder with a high degree of agglomeration [25]. The HIP process was intended to eliminate the pores formed by vacuum sintering; therefore, the pre-sintering process was designed to restrict pores to the intergranular sites so that the HIP could easily remove them. Thus, an agglomerated powder with closely packed particles was used as the precursor to trap most pores in the intergranular areas. The optimal processing temperatures for pre-sintering and HIP were 1600°C and 1500°C, respectively. If the HIP temperature was too high, e.g., 1625°C, the samples were opaque because Ar molecules had diffused into the capsule. More recently, a considerable research reported that highly transparent Y_2O_3 ceramics with a mean grain size of 0.6 μm could be fabricated using a combination of HP and HIP with a commercial Y_2O_3 powder and ZrO_2 as the sintering aid [26]. The HP conditions were 1300–1550°C at 20 MPa for 3 h, and the HIP conditions were 1450°C at 180 MPa of Ar for 5 h. The optimal HP parameters were 1400°C for 3 h, which yielded ceramics with 83.4% and 78.3% in-line transmittance at 1100 nm and 400 nm, respectively. Fig. 4 shows photographs of Y_2O_3 ceramic samples that were hot-pressed at different temperatures.

Fig. 4. Optical appearances of HIP treated Y_2O_3 ceramics hot-pressed at 1300, 1350, 1400, 1450, 1500, and 1550°C (2 mm in thickness) [26].

Zn^{2+}-doped Y_2O_3 ceramics (1 mol%) were fabricated by SPS and systematically studied the influence of experimental parameters such as the heating rate, sintering temperature, holding time, and loading stress [28]. The optimal conditions for obtaining transparent Zn^{2+}-doped Y_2O_3 ceramics were heating at 2°C/min, sintering at 890°C, holding for 0.5 h, and applying 150–170 MPa of pressure shown in Fig. 5. The transmittance of these Zn^{2+}-doped

Y_2O_3 ceramics reached 65% at 600 nm.

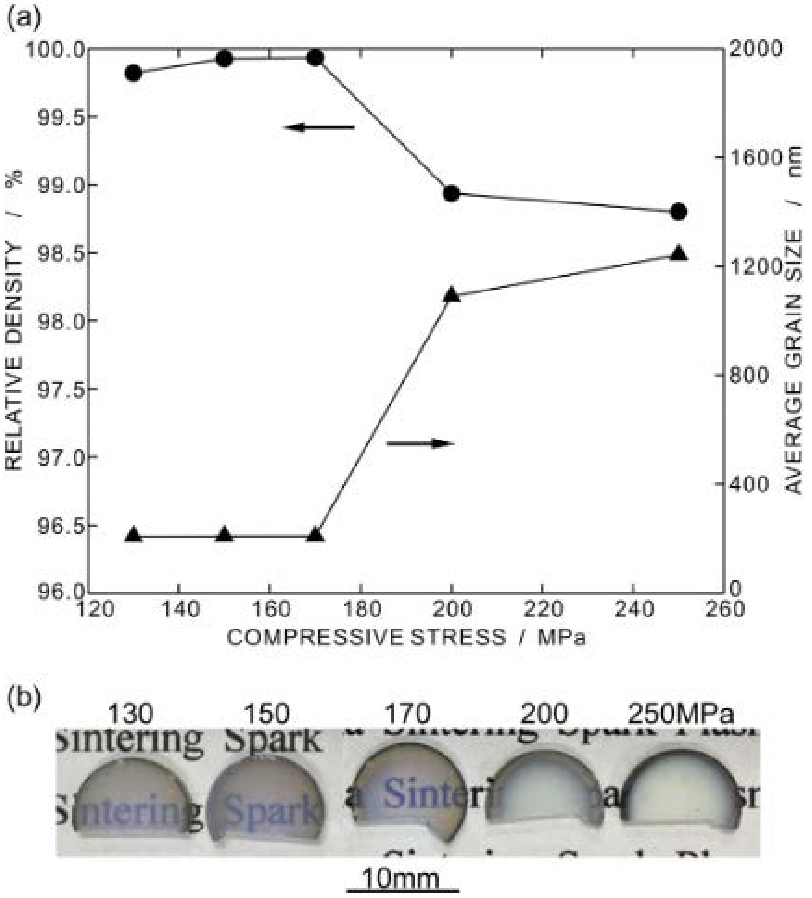

Fig. 5. (a) Relationship between relative density, and average grain size and (b) optical appearances of the Zn^{2+}:Y_2O_3 ceramics under the various mechanical pressures [28].

Yb^{3+}-doped Y_2O_3 ceramics were fabricated by SPS with rapid loading of mechanical pressure as 82.7 MPa at 1250°C [29]. The successfully doped Yb^{3+}:Y_2O_3 ceramics was investigated for the optimal condition of loading of mechanical pressure. Loading of 82.7 MPa in 1 min at 1250°C was led to a significant improvement of optical transmittance and achieved the 78% at 1030 nm as shown in Fig. 6.

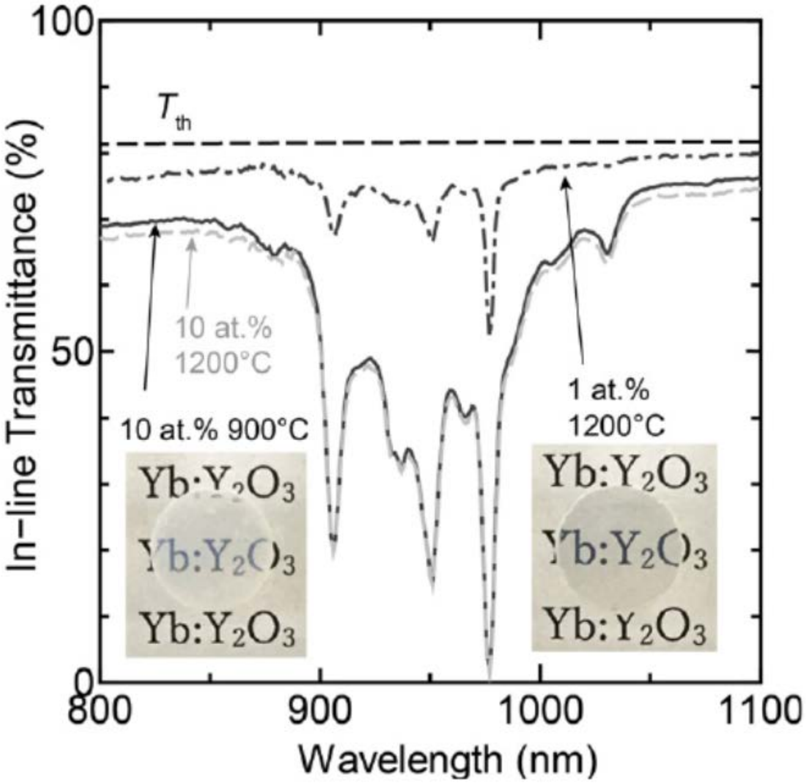

Fig. 6. The transmittance of SPSed 1 and 10 at% Yb^{3+}:Y_2O_3 ceramics with loading applied at 900°C and 1200°C. The SPSed samples were placed 10 mm above the text [29].

1.2.2. Rare-Earth Aluminum Garnets ($RE_3Al_5O_{12}$)

Rare-earth aluminum garnets (REAG) have been attracting long-term research interest as phosphors, solid-state lasers, and scintillators, among which yttrium aluminum garnet (YAG) and lutetium aluminum garnet (LuAG) might be the best known [33]. The REAG crystallizes in a body-centered cubic (BCC) crystal structure with the Ln atoms residing in the dodecahedral interstices built up via the Al–O polyhedral corner-sharing, as shown in Fig. 7. Owing to its high chemical and radiation stability, wide bandgap, and excellent radiation conversion efficiency, the REAG has proven to be one of the best hosts for the incorporation of rare-earth activators (such as Ce^{3+}, Nd^{3+}, Er^{3+}, Eu^{3+}, Tb^{3+}, Dy^{3+}, Etc.) for a wide range of optical applications. As well-known examples, Eu^{3+}, Tb^{3+}, and Ce^{3+} doped YAG are among the most important red, green, and yellow phosphors, respectively [34,35].

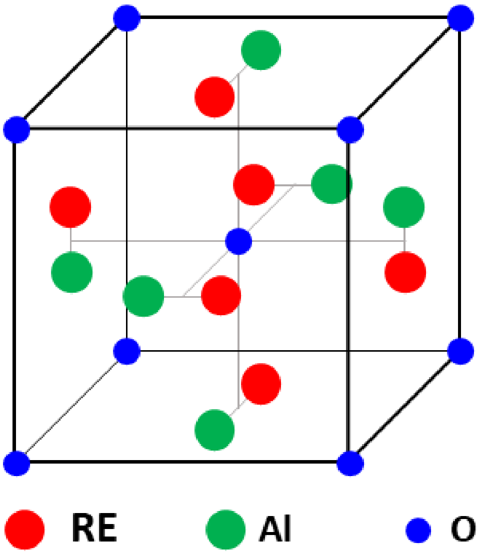

Fig. 7. BCC crystal structure of REAG ceramics with high symmetry.

Among the family of the garnet group, especially yttrium aluminate ($Y_3Al_5O_{12}$), also known as YAG, is one of the most important materials, which has a centrosymmetric cubic structure thus is isotropic [36]. The main applications of YAG are in solid-state lasers, but transparent YAG ceramics also have potential applications in high-temperature structural materials and fluorescent host materials because YAG has high thermal stability, high chemical stability, and homogenous optical properties [37,38]. In addition, since YAG has high X-ray stopping power by high theoretical density and physical reliability, it is the most promising candidate for scintillation application [39]. Representative research on YAG-based transparent ceramics are listed in Table 3.

Table 3. Sintering parameters and optical transmittance of representative research on transparent YAG ceramics.

Powder Processing	Sintering Parameters	Transmittance	Ref.
YAG, Solid-state reaction	CIP: 140 MPa, Vacuum sintering: 1500–1850°C/5 h/1.3X10^{-3} Pa	82% at 600 nm	[38]
1 at% Ho:YAG, 0.6 wt% TEOS, Solid-state reaction	CIP: 250 MPa, Vacuum sintering: 1760°C/20 h, Annealing: 1400°C/1 h	82% at 700 nm	[41]
YAG, MgO+CaO (0.2 mol%), Solid-state reaction	CIP: 210 MPa, Vacuum sintering: 1820–1840°C/8 h/10^{-6} Torr	80% at 600 nm	[43]
Nd:YAG (1 at%), 0.07 wt% SiO_2, Solid-state reaction	CIP: 200 MPa, Pre-sintering: 1650°C/0–6 h, HIP: 1650°C/1–6 h; 150 MPa	75% at 600 nm	[45]
Nd:YAG (2 at%), co-precipitation, 0.25 wt% LiF	SPS: 1100°C/3 min (100°C/min); 1250–1390°C/20 min (10°C/min); 28 MPa	75% at 700 nm	[46]
YAG commercial powder, 5 wt% LiF	SPS: 800–1450°C/20 min (50°C/min); 50 MPa	–	[47]
Er:YAG (0.5 at%) commercial powder	SPS: 1600°C (50°C/min); 30–70 MPa	–	[49]

Solid-state reaction methods are the most widely adopted process for fabricating transparent YAG ceramics from commercial or synthesized precursors of oxides or other compounds [40–45]. In 1995, Ikesue et al. used the solid-state reaction method to fabricate YAG and Nd:YAG transparent ceramics from Al_2O_3, Y_2O_3, and Nd_2O_3 synthesized by alkoxide hydrolysis, thermal pyrolysis, and oxalate precipitation, respectively [38]. The mixed powders were compacted and sintered at 1600–1850°C for 5 h under a 1.3×10^{-3} Pa vacuum. These transparent ceramics' optical properties and laser performance were comparable to those of single crystals.

Transparent YAG-based ceramics have also been produced using SPS, although SPS is not as famous for YAG ceramics as it is for other transparent ceramics [46–49]. Wang et al. used SPS to transform the metastable hexagonal $YAlO_3$ (YAH) phase of YAG to a transparent ceramic [48]. The transformation of the YAH phase of YAG at approximately 920°C was accompanied by particle rearrangement, which provided an additional densification mechanism. Furthermore, applied pressure also played an important role in promoting phase transformation. At 920°C and 80 MPa, as shown in Fig. 8, the in-line transmittance was 44% and 66% at 680 nm and 1000 nm, respectively. More importantly, the average grain size was as small as 380 nm. Generally, the transparent YAG ceramics fabricated using SPS have had relatively low optical transparency because of the contamination introduced by the direct contact between the samples and the dies; this contamination must be prevented to further utilize the SPS technique.

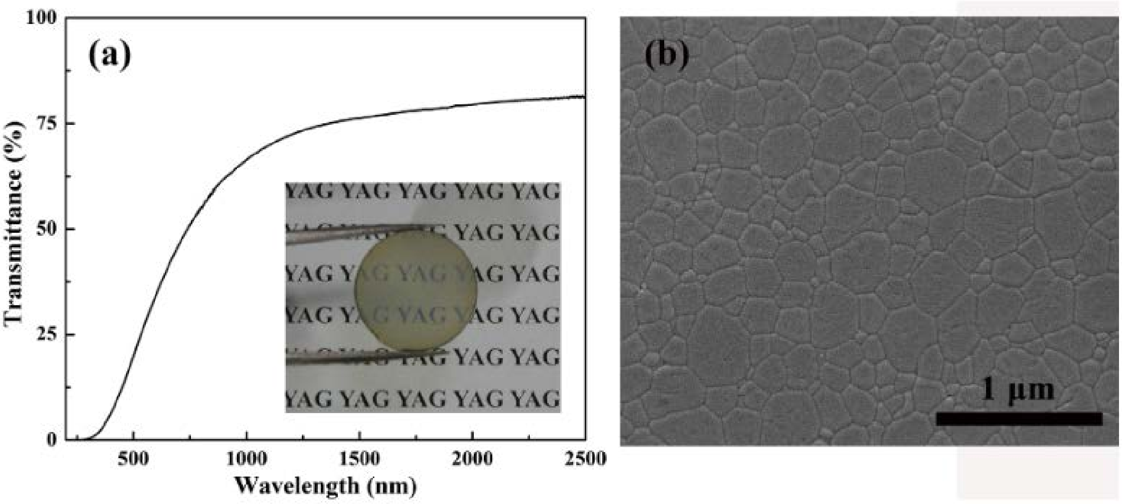

Fig. 8. (a) Optical transmittance and appearance of YAG ceramics sintered at 920°C under 80 MPa for 50 min. (b) SEM image of thermally etched surface of YAG ceramics.

When transparent ceramics are used for solid-state lasers, active components – most often rare earth elements – are added to the ceramic to achieve the desired wavelength. As mentioned earlier, the concentration of dopants in transparent ceramics is not limited by solubility. For example, as shown in Fig. 9, transparent Er:YAG ceramics with 1–90% Er^{3+} have been readily obtained using the solid-state reaction method and vacuum sintering technique [49]. The in-line transmittance of these Er:YAG ceramics was as high as 84% at 1100 nm, comparable to that of single crystals.

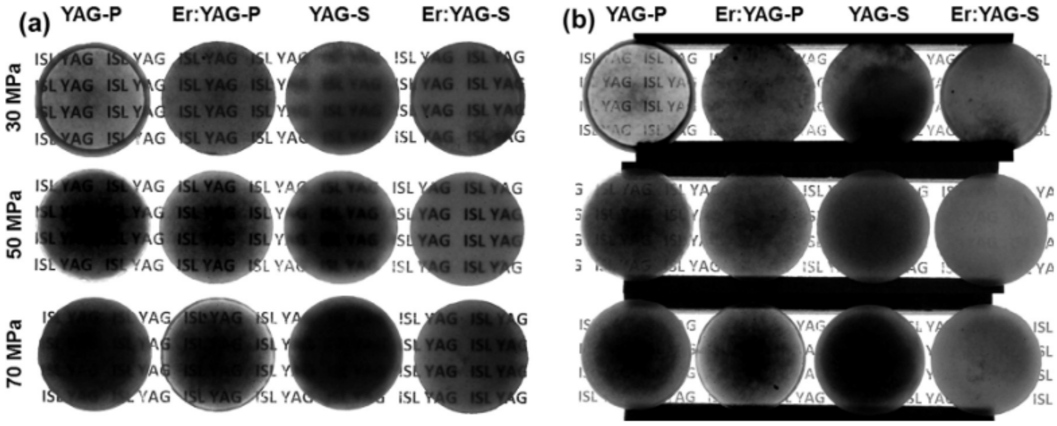

Fig. 9. Optical appearances of the sintered samples of each commercial powder fabricated by SPS under 30, 50, and 70 MPa, placed (a) on and (b) at 20 mm above a light table.

Recently, YAG is being considered for scintillation applications but has the disadvantages of insufficient theoretical density and X-ray stopping power. LuAG is more desirable but is of prohibitively high cost. In this regard, (Gd,Lu)AG solid solutions would be more desirable since Gd (atomic weight: 157.3) is much heavier than Y (atomic weight: 88.9), and the material is significantly cheaper than LuAG. Pure GdAG, however, is metastable and undergoes thermal decomposition to more stable $GdAlO_3$ perovskite and Al_2O_3 ($Gd_3Al_5O_{12} \rightarrow 3GdAlO_3 + Al_2O_3$) in the temperature range of ~1300–1500°C [50]. It is known that the occurrence and stability of compounds in the RE_2O_3–Al_2O_3 binary system heavily depend on the size of RE^{3+}, owing to lanthanide contraction, and Gd is the boundary element for the garnet structure to be formed [51]. The thermal decomposition severely retards GdAG-based phosphors and transparent ceramics developments. Considerable research supposed that the GdAG lattice can be effectively stabilized via doping with 10 at% or more of significantly smaller Lu^{3+} to form (Gd,Lu)AG solid solutions [52,53], which paved the way for the development of highly efficient (Gd,Lu)AG:Dy^{3+} phosphors in this work. Lu^{3+} was chosen as the stabilizer because it is optically inert and that it is the tiniest and heaviest lanthanide, which allows the most effective stabilization and higher theoretical density of the resultant garnet.

1.3. Sintering Technologies for Fabrication of Transparent Ceramics

Common optically transparent materials, such as glasses and polymers, have been widely used in industrial applications and daily life. However, these materials have relatively poor mechanical strengths and sometimes insufficient chemical and physical stabilities. Also, they usually possess relatively low melting temperatures and low resistance against the corrosive atmosphere, so they cannot be used for applications at high temperatures or another harsh environment. Ceramic materials, therefore, emerge as a powerful candidate for transparent materials used in high-temperature and/or corrosive environments. Single crystals of ceramics, such as sapphire (Al_2O_3) and YAG ($Y_3Al_5O_{12}$), are essentially optically transparent and have been in practical use for various industrial applications. However, the growth of single crystals requires very high temperatures and a long processing time, leading to expensive products and components. Hence, transparent polycrystalline ceramics are of practical importance in optical applications. The advantage of polycrystals is that they can be more extensive in dimensions and can be produced at lower temperatures, comparing to single crystals. In addition, functionalization of the ceramic sample by doping or manufacturing functionally graded materials can be more readily prepared for polycrystalline ceramics than single crystals. In contrast to single crystals, polycrystalline ceramics are generally opaque because of light-scattering sources as mentioned later. For attaining optical transparency in polycrystalline ceramics, it is necessary to eliminate residual pores and other defects from the sintered sample because such defects drastically deteriorate optical quality.

Various synthesis methods have made several efforts to eliminate residual defects from sintered samples by various synthesis methods. Improving sinterability is essential to minimize defects (residual pores in the sintered sample), leading to optical transparent ceramics so that researchers have optimized sintering conditions from raw powder synthesis to consolidation methods. As for sintering processes, pressure-assisted techniques such as hot-pressing (HP) and hot isostatic pressing (HIP) are widely employed to improve the sintered materials' quality and fabricate transparent ceramic samples. HIP synthesis is an effective technique to produce the transparent bulk ceramic sample. Because the synthesis of high-quality powders for transparent ceramics is not significantly different from that for other materials, which can be found widely in the reported research. It is essential to develop advanced sintering technology and apply the sintering technology under optimized conditions.

1.3.1. Field-Assisted Sintering Technology (FAST)

FAST has become necessary for the rapid fabrication of fully dense ceramic powders. Among these, the novel SPS and flash sintering (FS) techniques, or a combination of both were used for the superfast densification of ceramic nanoparticles within a few minutes. Although these two techniques differ in the voltage and current levels applied to the ceramic powder compact, hence in the process duration, they may exhibit similar electrical and thermal processes. Therefore, these techniques are appropriate for the fabrication of fully dense nano-crystalline ceramics using nanoparticle precursors. In this respect, the prime target is to fabricate a fully dense ceramic whose nano-crystalline character is preserved and affects its properties [54–58]. However, the preservation of the nano-crystalline character of the green powder compact to its dense counterpart is not straightforward and depends upon several material and process parameters.

1.3.1.1. Spark Plasma Sintering (SPS)

SPS is a newly developed method for obtaining fully dense and fine-grained transparent ceramics at low temperatures within short time durations [59–63]. It is also known as the FAST or pulsed electric current sintering (PECS). A schematic diagram of SPS equipment is graphically proposed in Fig. 10 (a). In normal hot pressing, heating is accomplished externally by heating a coil, while SPS uses a high-density current flux flowing through the powder compacts the punches and the die to cause Joule heating and discharge phenomena between each particle as shown in Fig. 10 (b). The SPS technique has a significant advantage over HIP and HP because it can complete the densification within a short duration [64]. Because of this, it is a potential technique to densify nanosized powders without the presence of significant grain coarsening that is unavoidable during the standard densification routes. The densification process in SPS is generally divided into three stages [54]. The packing of the particles characterizes the first stage, the second stage is related to a diffusion process accompanying the neck formation and grain sliding, and the final stage is the removal of pores mainly through the grain boundary. Applying pressure strongly affects the initial packing and densification in the second and third stages. High pressure is constantly applied in the typical SPS process. Heating rate is another important sintering parameter for densification in the second and third stages.

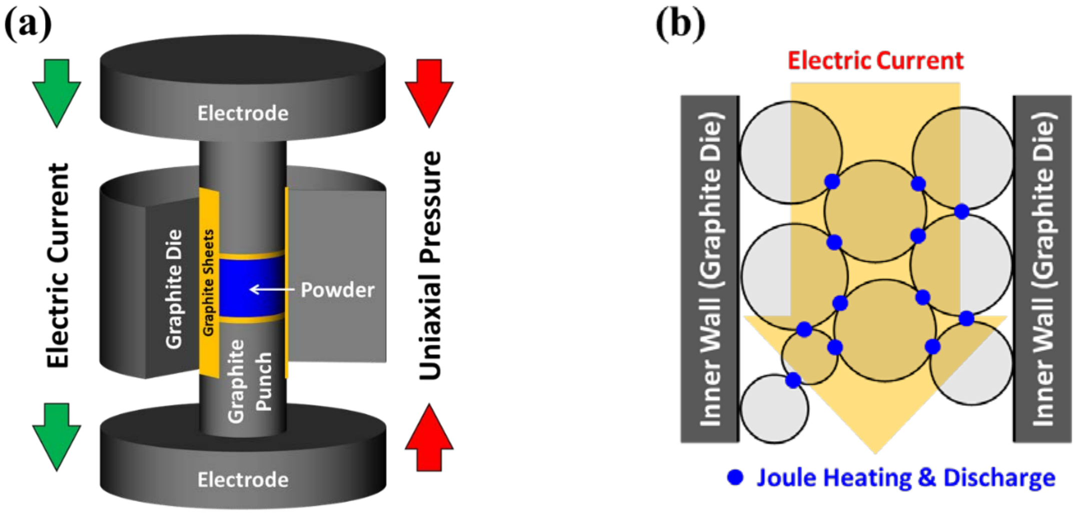

Fig. 10. Schematic diagrams of (a) equipment and (b) heating principle of SPS technology.

It was expected that electrical discharge plasma takes place between powder particles, resulting in localized and momentary heating of the particle surfaces [65]; self-heat generation by the electric discharge plasma between particles at an early stage of on-off DC pulse application would act on promoting sintering as shown in Fig. 11 [66]. In addition, it has been speculated that the surfaces of the particles are purified and activated due to the electric discharge plasma on the particle surfaces; the purified surface layers of the particles could melt and fuse forming necks between the particles [67]. However, the occurrence of the discharge has been questioned in recent years.

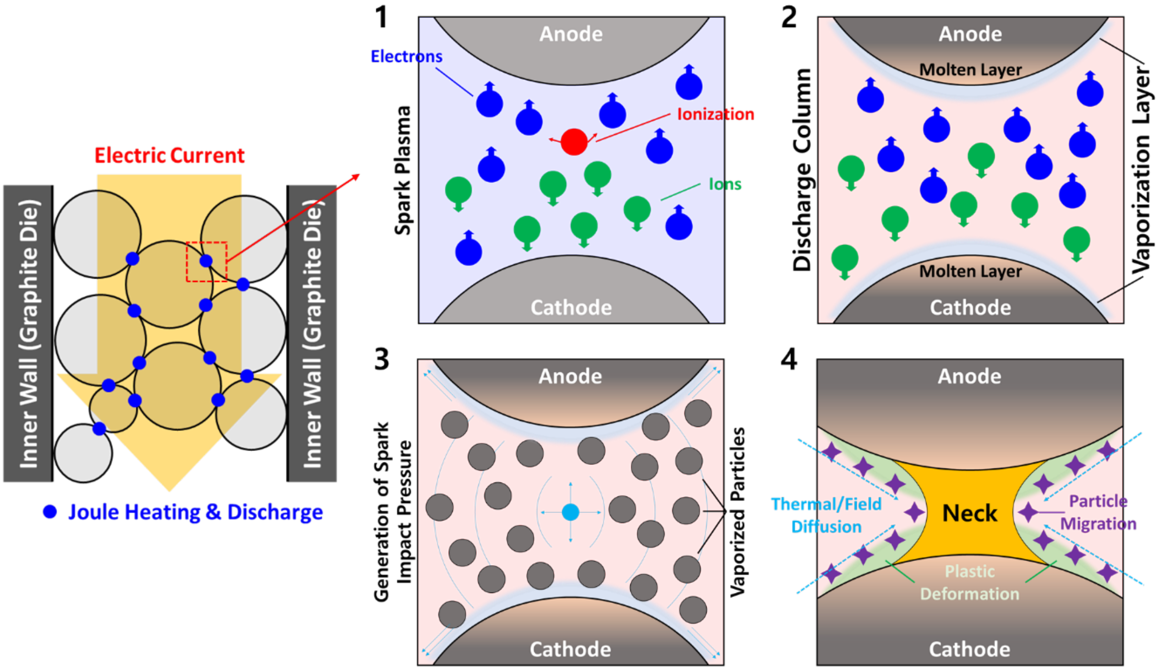

Fig. 11. Schematic diagram of promotion of densification process [66].

It is widely accepted that electric field can accelerate the densification of ceramics, while the primary purpose of imposed electric current in SPS is usually supposed to provide the required amount of resistive heating. For instance, DC electrical fields of approximately 20 V/cm lower the sintering temperature of 3 mol% yttria-stabilized tetragonal zirconia polycrystal (3Y-TZP) from 1400°C to 1300°C [68]. However, the origin of the electric field on the enhancement of mass transport is still unclear. In the case of SPS, the applied voltages are usually relatively low, lower than the required value to trigger electromigration. Recently, it has been reported that electric field/current can involve the formation of anion vacancies in ceramics [69]; electron energy loss spectrometry (EELS) analysis suggested that Y_2O_3 polycrystal consolidated by SPS exhibited a reduced state in comparison to Y_2O_3 sintered in air and a vacuum. Highly reduced states in other oxide ceramics densified under strong electric field or current have also been revealed by EELS analysis, as mentioned later. The role of DC field and/or current is still an open question, but it would seem that field/current can trigger the formation of ionic defects and consequently facilitate diffusional mass transport, leading to acceleration of densification of ceramic materials.

It was recently reported that transparent alumina with fine grains could also be obtained using the SPS technique [59–62]. Owing to the advantage of rapid heating, the alumina ceramics obtained by SPS had grain sizes and densities comparable to those of the HIPed ones [70,71]. For example, a fully dense (a relative density of 100 wt%) alumina with a grain size of 0.5 mm was obtained at 1200°C by SPS in Fig. 12 [59].

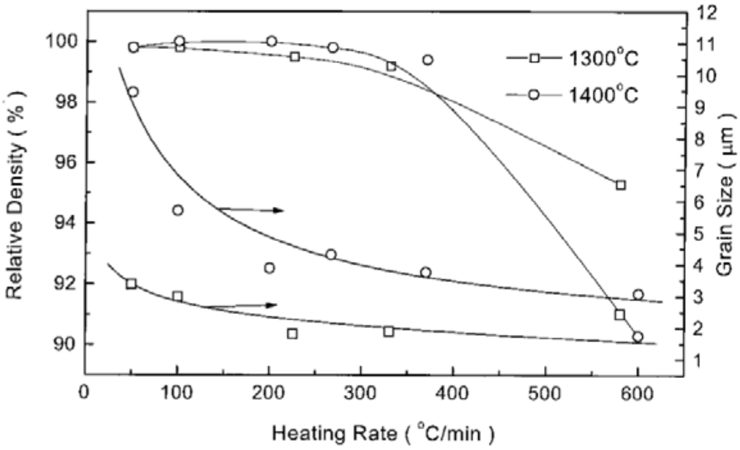

Fig. 12. Influence of heating rate on densification and grain size in fully densified Al_2O_3 ceramics fabricated by SPS at 1200°C. [59].

The SPS technique can be employed to sinter polycrystalline alumina disks and fabricate hemispherical domes [55]. As demonstrated by Jiang et al. [72], the fabrication of transparent polycrystalline alumina domes could be obtained by combining sintering and forming into one step in minutes instead of hours needed when using conventional methods, as shown in Fig. 13. This forming method provides an unprecedented opportunity to make optically transparent domes at much lower costs.

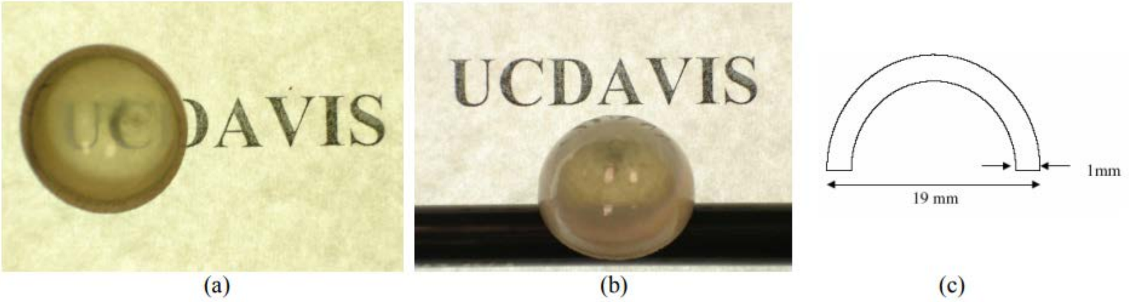

Fig. 13. Transparent dome made of polycrystalline Al_2O_3 by using SPS technique showing (a) clear image of bottom words; (b) surface quality; (c) dimensions [72].

Much research and development efforts are still required to use transparent ceramics produced by SPS for industrial applications. Fundamental investigations on the origin of enhanced densification in SPS are needed from an atomistic point of view; a significant number of experimental results strongly indicated that some ionic defect reactions are involved during SPS processing. Effects of electrical current/field on mass transport, reactivity, microstructure evolution, and final chemical and physical properties are still remained to be understood. To control thermal/electrical conduction and stress distribution/mass transportation inside the die during SPS processing, new experimental techniques such as direct measurement of field strength inside a material and theoretical analyses such as finite element method (FEM) calculations must be employed. On the other hand, for promoting transparent ceramics produced by SPS to industrial use, not only the improvement of physical/chemical properties but also upscaling of products and homogenization of microstructure are key technologies.

Using the electro/magnetic fields pioneers new and unexpected technologies of SPS. In addition, nanometer-scaled and defect-free microstructures attained by the SPS improve mechanical strength and enable superplastic deformation, and near-net-shape forming of the SPSed transparent ceramics. Scale-up of components size and improvement in desirable properties of optically transparent ceramics through the development of SPS devices and progress in fundamental research on the process will advance the industrial applications for transparent ceramics in the near future.

1.3.1.2. Flash Sintering (FS)

FS has received much international attention in recent as a drastic, almost instantaneous sintering process, which can be classified into FAST. Raj and co-workers have demonstrated 3 mol% Y_2O_3-stabilized tetragonal ZrO_2 polycrystals (3Y-TZP) can be fully densified at 850°C within 5 s under an electric field of 120 V/cm [73], while the same material can be usually densified by conventional, pressure-less sintering in the air at 1400–1500°C for several hours. The abrupt densification at relatively low sintering temperature is called the FS, in distinction from FAST, in which the enhancement of densification is more gradual than FS. Fig. 14 shows the typical process of the FS [74].

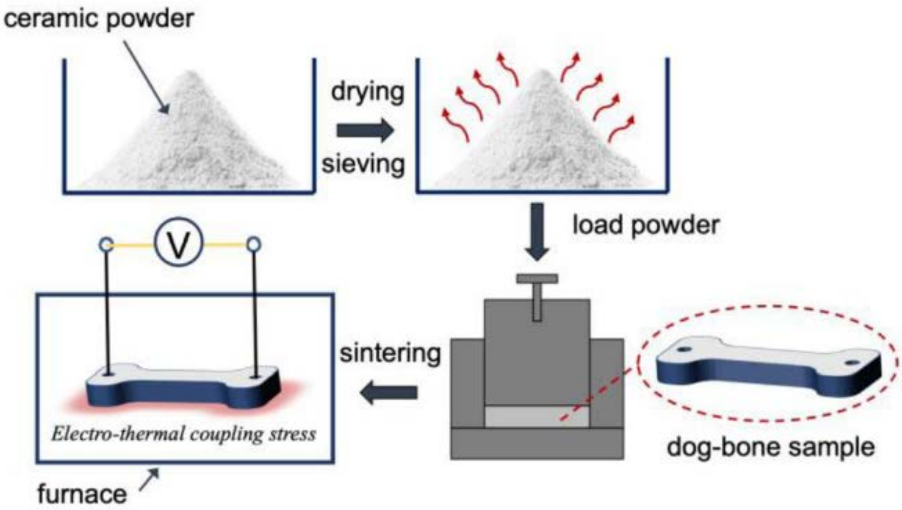

Fig. 14. Schematic diagram of the typical process of the FS experiment [74].

A strong DC or AC electric field is applied to green compact by electric power supply through platinum wires. The furnace temperature is raised at a constant heating rate. Beyond threshold field strength and furnace temperature, the electric conductivity of the green compact abruptly increases, and electric current through the material accordingly increases. The almost instantaneous densification consequently takes place. The densification curves in 3Y-TZP sintered under different DC fields as a function of furnace temperature are depicted in Fig. 15 [73]. In this figure, the linear shrinkage data presented in ref. [73] were converted to relative density values. As shown in Fig. 15, abrupt densification of TZP occurred under the DC fields of higher than 60 V/cm, and the sintering temperature decreased with the increasing field strength. The FS is characterized by almost rapid densification (typically occurs in just a few seconds) and a nonlinear increase in electric conductivity under a threshold condition of temperature and applied field [73,75]. The nature of FS is fundamentally different from FAST, in which fields lead to a gradual enhancement in the sintering without any change in the specimen conductivity. Abrupt densification at low temperature by FS has been demonstrated in various ceramics [76].

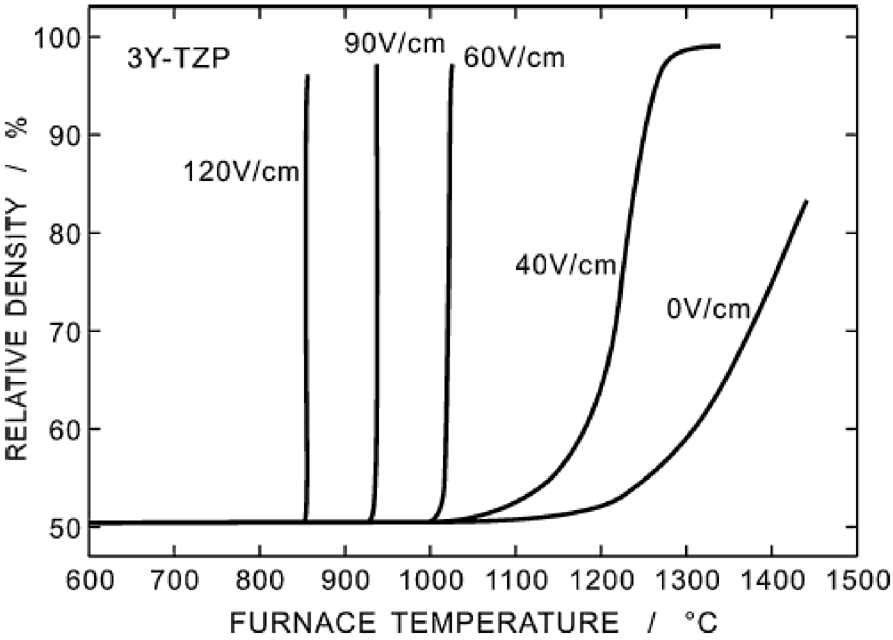

Fig. 15. The densification curves in 3Y-TZP sintered under different DC fields (0, 40, 60, 90, and 120 V/cm) [73] as a function of furnace temperature.

The FS technique can be applied to various oxide and non-oxide ceramics, even low-sinterability materials such as Y_2O_3. For instance, DC fields greater than 300 V/cm can trigger FS in undoped Y_2O_3 [77]. Conventional sintering requires very high temperatures, typically > 1600°C as noted above, and a vacuum or hydrogen atmosphere. However, by applying an electric field of 1000 V/cm, a dense Y_2O_3 polycrystal was obtained at 985°C in less than 10 s [78]. Nevertheless, full densification is still difficult to be accomplished by the FS. A typical example of the suppressed final density was seen in the flash sintering of $BaTiO_3$. Under a strong electric field beyond a critical value, flash sintering posed electric discharge damage in $BaTiO_3$ samples, resulting in a low density of the sintered sample with several residual pores and tunnel-like physical damages [79,80]. In addition, crystalline thin layers were generated along $BaTiO_3$ grain boundaries near the electric discharged damage [81]. The Ba/Ti cation ratio of the secondary crystalline phases was Ti-excess, indicating that Ba cations tended to evaporate because of the excess heat yielded by the discharging.

At present, it is still challenging to produce transparent ceramics by the FS process. In addition, limited shape and dimensions of material are also disadvantages of the FS, as well as SPS so far. In contrast to the several disadvantages, the FS is a promising method because of the short sintering time and low sintering temperature, and the number of reports on the FS and related phenomena has significantly increased in recent years. It is expected to develop translucent or transparent ceramic samples by the FS with short-time and low-temperature synthesis.

1.4. Motivation and Objectives

To improve the optical properties and mechanical/thermal stability of transparent ceramic phosphors, many research groups have made efforts with the SPS process as advanced sintering technology. However, it may be challenging to obtain transmittance close to the theoretical value due to the low sintering temperature and short sintering time, which are the advantages of the SPS process. Although the SPS process allows direct heating by an electric field, it has often been reported that residual pores due to rapid densification and a temperature gradient inside the powder compacts are concomitantly occurred, deteriorating optical transparency, or inducing non-uniform appearances and microstructures. In addition, since SPS equipment is typically composed of graphite components, it has been reported that sintering is performed in a carbon-rich environment and reducing atmosphere, with fatal consequences of carbon contamination and oxygen vacancy for the optical properties.

The main purpose of this study is to improve the optical properties by supplementing the disadvantages, such as non-uniform sintering behavior, residual pores, and carbon contamination, that the SPS process may have for the fabrication of transparent Y_2O_3 and $RE_3Al_5O_{12}$ ceramics as lasers and scintillators. Therefore, the evolution of non-uniform sintering behavior is first investigated by the detailed microstructural and spectroscopic analysis on the horizontal direction of sintered samples. Next, to improve the optical/mechanical/thermal properties of transparent Y_2O_3 and $RE_3Al_5O_{12}$ ceramics, the microstructure refinement or control is made possible by applying a two-step profile to the SPS process. The two-step profile can achieve primary densification in the first-step sintering while suppressing microstructural coarsening due to the relatively low temperature. In addition, in the second-step sintering, it is possible to achieve full densification and removal of residual pores for a relative density of more than 99%. The sintering process is divided into two parts to promote densification uniformity and efficiency, and a two-step profile has already been proposed for several sintering technologies. However, research applied to the SPS process has been rarely reported. As research is required to fabricate the transparent ceramic phosphors and improve their properties, improving the non-uniform sintering behavior and the microstructure control by applying the two-step sintering profile to the SPS process can sufficiently prove the originality and value of this study.

In a broad sense, among the transparent ceramic phosphors, this study consists of 2 parts, such as transparent Y_2O_3 ceramics for laser application in chapters 2 and 3 and transparent Ce^{3+}:$(Gd,Lu)_3Al_5O_{12}$ ceramics for scintillators in chapters 4 and 5. The main purpose of each chapter is briefly presented below.

In chapter 2, the main purpose is to investigate non-uniform sintering behavior by demonstrating defect diffusion to the center and matter diffusion to the periphery through detailed microstructural and spectroscopy analysis.

Chapter 3 is mainly focused on that a two-step heating and pressure profile, determined based on the range to which shrinkage occurs via the SPS shrinkage curve, is applied to improve the optical transparency of transparent Y_2O_3 ceramics to the theoretical value.

In chapter 4, the main purpose is to investigate the correlation between the optical properties and carbon contamination according to the annealing process for restoring the optical properties deteriorated due to carbon contamination of a negative effect in the SPS process.

Chapter 5 is focused on the improvement of the optical property of transparent Ce^{3+}:$(Gd,Lu)_3Al_5O_{12}$ ceramics with microstructure control by a two-step SPS profile. In the two-step profile, the primary densification and the suppression of the excessive coarsening are achieved at first-step sintering, and the full densification and removal of residual pores are accompanied at the second-step sintering.

References

[1] A. Ikesue, Y.L. Aung, Ceramic laser materials, Nat. Photonics, 2 (2008) 721–727.

[2] J. Sanghera, S. Bayya, G. Villalobos, et al., Transparent ceramics for high-energy laser systems, Opt. Mater. 33 (2011) 511–518.

[3] J. Sanghera, W.H. Kim, G. Villalobos, et al., Ceramic Laser Materials, Mater. 5 (2012) 258–277.

[4] J. Sanghera, W.H. Kim, G. Villalobos, et al., Ceramic laser materials: Past and present, Opt. Mater. 35 (2013) 693–699.

[5] A. Krell, T. Hutzler, K. Klimke, Transmission physics and consequences for materials selection, manufacturing, and applications, J. Eur. Ceram. Soc. 29 (2009) 207–221.

[6] P. Zhao, H. Zhao, J. Yu, et al., Crystal structure and properties of Al_2O_3-Cr_2O_3 solid solutions with different Cr_2O_3 contents, Ceram. Int. 44 (2018) 1356–1361.

[7] A. Mondal, S. Ram, Reconstructive phase formation of ZrO_2 nanoparticles in a new orthorhombic crystal structure from an energized porous $ZrO(OH)_2\cdot xH_2O$ precursor, Ceram. Int. 30 (2004) 239–249.

[8] E. Djurado, P. Bouvier, G. Lucazeau, Crystallite Size Effect on the Tetragonal-Monoclinic Transition of Undoped Nanocrystalline Zirconia Studied by XRD and Raman Spectrometry, J. Solid State Chem. 149 (2000) 399–407.

[9] M. Aghazadeh, A.A.M. Barmi, H.M. Shiri, S. Sedaghat, Cathodic electrodeposition of $Y(OH)_3$ and Y_2O_3 nanostructures from chloride bath. Part II: Effect of the bath temperature on the crystal structure, composition and morphology, Ceram. Int. 39 (2013) 1045–1055.

[10] J.G. Li, T. Ikegami, T. Mori, Fabrication of transparent Sc_2O_3 ceramics with powders thermally pyrolyzed from sulfate, J. Mater. Res. 18 (2003) 1816–1822.

[11] J. Zeler, L.B. Jerzykiewicz, E. Zych, Flux-Aided Synthesis of Lu_2O_3 and Lu_2O_3:Eu–

Single Crystal Structure, Morphology Control and Radioluminescence Efficiency, Mater. 7 (2014) 7059–7072.

[12] J. Li, Y. Pan, F. Qiu, et al., Synthesis of nanosized Nd:YAG powders via gel combustion, Ceram. Int. 33 (2007) 1047–1052.

[13] S. Takahashi, A. Kan, H. Ogawa, Microwave dielectric properties and crystal structures of spinel-structured $MgAl_2O_4$ ceramics synthesized by a molten-salt method, J. Eur, Ceram. Soc. 37 (2017) 1001–1006.

[14] Y. Nigara, M. Ishigame, T. Sakurai, Infrared Propertied of Yttrium Oxide, J. Phys. Soc. Jpn. 30 (1971) 453–458.

[15] A. Fukabori, T. Yanagida, J. Pejchal, et al., Optical and scintillation characteristics of Y_2O_3 transparent ceramic, J. Appl. Phys. 107 (2010) 073501.

[16] A. Pirri, G. Toci, B. Patrizi, M. Vannini, An overview on Yb-doped transparent polycrystalline sesquioxide laser ceramics, IEEE J. Sel. Top. Quantum Electron. 24 (2018) 1602108.

[17] X. Hou, S. Zhou, T. Jia, et al., Investigation of up-conversion luminescence properties of RE/Yb co-doped Y_2O_3 transparent ceramic (RE=Er, Ho, Pr, and Tm), Phys. B: Condens. Matter 406 (2011) 3931–3937.

[18] A.L. Micheli, D.F. Dungan, J.V. Mantese, High-Density Yttria for Practical Ceramic Applications, J. Am. Ceram. Soc. 75 (1992) 709–711.

[19] J. Iwasawa, R. Nishimizu, M. Tokita, et al., Plasma-Resistant Dense Yttrium Oxide Film Prepared by Aerosol Deposition Process, J. Am. Ceram. Soc. 90 (2007) 2327–2332.

[20] R.A. Lefever, J. Matsko, Transparent yttrium oxide ceramics, Mater. Res. Bull. 2 (1967) 865–869.

[21] K. Serivalsatit, B. Kokuoz, B.Y. Kokuoz, et al., Synthesis, processing, and properties of submicrometer-grained highly transparent yttria ceramics, J. Am. Ceram. Soc. 93 (2010)

1320–1325.

[22] N. Saito, S.I. Matsuda, T. Ikegami, Fabrication of transparent yttria ceramics at low temperature using carbonate-derived powder, J. A. Ceram. soc. 81 (1998) 2023–2028.

[23] S.R. Podowitz, R. Gaume, R.S. Feigelson, Effect of Europium Concentration on Densification of Transparent Eu:Y_2O_3 Scintillator Ceramics Using Hot Pressing, J. Am. Ceram. soc. 93 (2010) 82–88.

[24] L. Gan, Y.J. Park, H.N. Kim, et al., The effects of the temperature and pressure on ZrO_2-doped transparent yttria ceramics fabricated by a hot-pressing method, Opt. Mater. 71 (2017) 109–116.

[25] J. Mouzon, A. Maitre, L. Frisk, et al., Fabrication of transparent yttria by HIP and the glass-encapsulation method, J. Eur. Ceram. Soc. 29 (2009) 311–316.

[26] L.L. Zhu, Y.J. Park, L. Gan, Fabrication and characterization of highly transparent Y_2O_3 ceramics by hybrid sintering: A combination of hot pressing and a subsequent HIP treatment, J. Eur. Ceram. Soc. 38 (2018) 3255–3260.

[27] X. Li, Y. Xu, X. Mao, et al., Investigation of optical, mechanical, and thermal properties of ZrO_2-doped Y_2O_3 transparent ceramics fabricated by HIP, Ceram. Int. 44 (2018) 1362–1369.

[28] H. Yoshida, K. Morita, B.N. Kim, et al., Low-Temperature Spark Plasma Sintering of Yttria Ceramics with Ultrafine Grain Size, J. Am. Ceram. soc. 94 (2011) 3301–3307.

[29] H. Furuse, S. Nakasawa, H. Yoshida, et al., Transparent ultrafine Yb^{3+}:Y_2O_3 laser ceramics fabricated by spark plasma sintering, J. Am. Ceram. Soc. 101 (2018) 694–702.

[30] H. Zhang, B.N. Kim, K. Morita, et al., Fabrication of Transparent Yttria by High-Pressure Spark Plasma Sintering, J. Am. Ceram. Soc. 94 (2011) 3206–3210.

[31] C.W. Park, J.H. Lee, S.H. Kang, et al., Characteristics of Y_2O_3 transparent ceramics rapidly processed using spark plasma sintering, J. Ceram. Process. Res. 18 (2017) 183–

187.

[32] Z. Hu, X. Xu, J. Wang, et al., Fabrication and spectral properties of Dy:Y_2O_3 transparent ceramics, J. Eur. Ceram. Soc. 38 (2018) 1981–1985.

[33] H. Yagi, T. Yanagitani, H. Yoshida, et al., The optical properties and laser characteristics of Cr^{3+} and Nd^{3+} co-doped $Y_3Al_5O_{12}$ ceramics. Opt. Laser Technol. 39 (2007) 1295–1300.

[34] X. Li, Q. Li, J. Wang, S. Yang, Synthesis of YAG:Eu phosphors with spherical morphology by solvo-thermal method and their luminescent property, Mater. Sci. Eng. B 131 (2006) 32–35.

[35] J.J. Zhang, J.W. Ning, X.J. Liu, et al., Synthesis of ultrafine YAG:Tb phosphor by nitrate–citrate sol–gel combustion process, Mater. Res. Bull. 38 (2003) 1249–1256.

[36] G. Xu, X. Zhang, W. He, et al., Preparation of highly dispersed YAG nano-sized powder by co-precipitation method, Mater. Lett. 60 (2006) 962–965.

[37] A. Ikesue, T. Kinoshita, K. Kamata, K. Yoshida, Fabrication and Optical Properties of High-Performance Polycrystalline Nd:YAG Ceramics for Solid-State Lasers, J. A. Ceram. Soc. 78 (1995) 1033–1040.

[38] A. Ikesue, I. Furusato, K. Kamata, Fabrication of Polycrystalline, Transparent YAG Ceramics by a Solid-State Reaction Method, J. Am. Ceram. Soc. 78 (1995) 225–228.

[39] C.H. Kim, W.H. Lee, A. Melis, et al., A Review of Inorganic Scintillation Crystals for Extreme Environments, Cryst. 11 (2021) 669.

[40] J. Li, Y. Wu, Y. Pan, et al., Solid-state-reactive fabrication of Cr,Nd:YAG transparent ceramics: the influence of raw material, J. Ceram. Soc. Jpn. 116 (2008) 572–577.

[41] T. Zhou, L. Zhang, Z. Li, et al., Toward vacuum sintering of YAG transparent ceramic using divalent dopant as sintering aids: Investigation of microstructural evolution and optical property, Ceram. Int. 43 (2017) 3140–3146.

[42] Y.L. You, L.H. Qi, H.Z. Miao, W. Pan, Preparation of transparent YAG ceramics via a

modified solid-state reaction method, Rare Metal Mater. Eng. 42 (2013) 348–350.

[43] W.X. Zhang, J. Zhou, W.B. Liu, et al., Fabrication, properties and laser performance of Ho:YAG transparent ceramic, J. Alloys Compd. 506 (2010) 745–748.

[44] X. Chen, T. Lu, N. Wei, et al., Fabrication and photoluminescence properties of Cr:YAG and Yb,Cr:YAG transparent ceramic, Opt. Mater. 49 (2015) 330–336.

[45] L. Chretien, L. Bonnet, R. Boulesteix, et al., Influence of hot isostatic pressing on sintering trajectory and optical properties of transparent Nd:YAG ceramics, J. Eur. Ceram. Soc. 36 (2016) 2035–2042.

[46] X. Zhang, G. Fan, W. Lu, et al., Effect of the spark plasma sintering parameters, LiF additive, and Nd dopant on the microwave dielectric and optical properties of transparent YAG ceramics, J. Eur. Ceram. Soc. 36 (2016) 2767–2772.

[47] A. Katz, E. Barraud, S. Lemonnier, et al., Role of LiF additive on spark plasma sintered transparent YAG ceramics, Ceram. Int. 43 (2017) 15626–15634.

[48] R. Wang, Y. Wang, Z. Fu, et al., Spark plasma sintering of transparent YAG ceramics assisted by the YAH–YAG phase transformation, J. Eur. Ceram. Soc. 36 (2016) 2153–2156.

[49] A. Katz, E. Barraud, S. Lemonnier, et al., Influence of powder physicochemical characteristics on microstructural and optical aspects of YAG and Er:YAG ceramics obtained by SPS, Ceram. Int. 43 (2017) 10673–10682.

[50] T. Shishido, K. Okamura, S. Yajima, $Gd_3Al_5O_{12}$ Phase Obtained by Crystallization of Amorphous $Gd_2O_3·5/3Al_2O_3$, J. Am. Ceram. Soc. 61 (1978) 373–375.

[51] M. Mizuno, T. Yamada, T. Noguchi, Phase Diagram of the System Al_2O_3-Sm_2O_3 at High Temperature, Yogyo-Kyokaishi 85 (1977) 374–379.

[52] J.K. Li, J.G. Li, Z.J. Zhang, et al., Effective lattice stabilization of gadolinium aluminate garnet (GdAG) via Lu^{3+} doping and development of highly efficient (Gd,Lu)AG:Eu^{3+}

red phosphors, Sci. Technol. Adv. Mater. 13 (2012) 065007.

[53] J.K. Li, J.G. Li, Z.J. Zhang, et al., Gadolinium Aluminate Garnet ($Gd_3Al_5O_{12}$): Crystal Structure Stabilization via Lutetium Doping and Properties of the $(Gd_{1-x}Lu_x)_3Al_5O_{12}$ Solid Solutions (x = 0–0.5), J. Am. Ceram. Soc. 95 (2012) 931–936.

[54] U.A. Tamburini, J.E. Garay, Z.A. Munir, Fast low-temperature consolidation of bulk nanometric ceramic materials, Scr. Mater. 54 (2006) 823–828.

[55] D. Jiang, D.M. Hulbert, J.D. Kuntz, et al., Spark plasma sintering: A high strain rate low temperature forming tool for ceramics, Mater. Sci. Eng. A 463 (2007) 89–93.

[56] O. Guillon, J.G. Julian, B. Dargatz, et al., Field-Assisted Sintering Technology/Spark Plasma Sintering: Mechanisms, Materials, and Technology Developments, Adv. Eng. Mater. 16 (2014) 830–849.

[57] D.N.F. Muche, J.W. Drazin, J. Mardinly, et al., Colossal grain boundary strengthening in ultrafine nanocrystalline oxides, Mater. Lett. 186 (2017) 298–300.

[58] G. Philippot, M. Albino, R. Epherre, et al., Local Distortions in Nanostructured Ferroelectric Ceramics through Strain Tuning, Adv. Electron. Mater. 1 (2015) 1500190.

[59] Z.J. Shen, M. Johnsson, Z. Zhao, M. Nygren, Spark plasma sintering of alumina, J. Am. Ceram. Soc. 85 (2002) 1921–1927.

[60] N. Roussel, L. Lallemant, B. Durand, et al., Effects of the nature of the doping salt and of the thermal pre-treatment and sintering temperature on spark plasma sintering of transparent alumina, Ceram. Int. 37 (2011) 3565–3573.

[61] B.N. Kim, K. Hiraga, K. Morita, H. Yoshida, Spark plasma sintering of transparent alumina, Scr. Mater. 57 (2007) 607–610.

[62] S. Grasso, C.F. Hu, G. Maizza, et al., Effects of pressure application method on transparency of spark plasma sintered alumina, J. Am. Ceram. Soc. 94 (2011) 1405–1409.

[63] L.Q. An, A. Ito, T. Goto, Two-step pressure sintering of transparent lutetium oxide by

spark plasma sintering, J. Eur. Ceram. Soc. 31 (2011) 1597–1602.

[64] R. Chaim, R. Marder, C. Estournes, Optically transparent ceramics by spark plasma sintering of oxide nanoparticles, Scr. Mater. 63 (2010) 211–214.

[65] M. Tokita, Trends in Advanced SPS Spark Plasma Sintering Systems and Technology, J. Soc. Powd. Technol. 30 (1993) 790–804.

[66] Z.Y. Hu, Z.H. Zhang, X.W. Cheng, et al., A review of multi-physical fields induced phenomena and effects in spark plasma sintering: Fundamentals and applications, Mater. Des. 191 (2020) 108662.

[67] N. Tamari, T. Tanaka, K. Tanaka, et al., Effect of Spark Plasma Sintering on Densification and Mechanical Properties of Silicon Carbide, J. Ceram. Soc. Jpn. 103 (1995) 740–742.

[68] D. Yang, H. Conrad, Enhanced sintering rate of zirconia (3Y-TZP) by application of a small AC electric field, Scr. Mater. 63 (2010) 328–331.

[69] B.N. Kim, K. Hiraga, K. Morita, H. Yoshida, Effects of heating rate on microstructure and transparency of spark-plasma-sintered alumina, J. Eur. Ceram. Soc. 29 (2009) 323–327.

[70] M. Suarez, A. Fernandez, J.L. Menendez, R. Torrecillas, Grain growth control and transparency in spark plasma sintered self-doped alumina materials, Scr. Mater. 61 (2009) 931–934.

[71] Y. Aman, V. Garnier, E. Djurado, Influence of green state processes on the sintering behaviour and the subsequent optical properties of spark plasma sintered alumina, J. Eur. Ceram. Soc. 29 (2009) 3363–3370.

[72] D. Jiang, D.M. Hulbert, U.A. Tamburini, et al., Spark plasma sintering and forming of transparent polycrystalline Al_2O_3 windows and domes, Window and Dome Technologies and Materials X 6545 (2007) 654509.

[73] M. Cologna, B. Rashkova, R. Raj, Flash Sintering of Nanograin Zirconia in < 5 s at 850°C, J. Am. Ceram. Soc. 93 (2010) 3556–3559.

[74] H. Zhou, X. Li, Y. Zhu, et al., Review of flash sintering with strong electric field, High Volt. (2021) in press. https://doi.org/10.1049/hve2.12080

[75] R. Raj, M. Cologna, J.S.C. Francis, Influence of Externally Imposed and Internally Generated Electrical Fields on Grain Growth, Diffusional Creep, Sintering and Related Phenomena in Ceramics, J. Am. Ceram. Soc. 94 (2011) 1941–1965.

[76] C.E.J. Dancer, Flash sintering of ceramic materials, Mater. Res. Express. 3 (2016) 102001.

[77] H. Yoshida, Y. Sakka, T. Yamamoto, et al., Densification behaviour and microstructural development in undoped yttria prepared by flash-sintering, J. Eur. Ceram. Soc. 34 (2014) 991–1000.

[78] J.C. M'Peko, J.S.C. Francis, R. Raj, Field-assisted sintering of undoped $BaTiO_3$: Microstructure evolution and dielectric permittivity, J. Eur. Ceram. Soc. 34 (2014) 3655–3660.

[79] A. Uehashi, H. Yoshida, T. Tokunaga, et al., Enhancement of sintering rates in $BaTiO_3$ by controlling of DC electric current, J. Ceram. Soc. Jpn. 123 (2015) 465–468.

[80] H. Yoshida, A. Uehashi, T. Tokunaga, et al., Formation of grain boundary second phase in $BaTiO_3$ polycrystal under a high DC electric field at elevated temperatures, J. Ceram. Soc. Jpn. 124 (2016) 388–392.

[81] Y. Nakagawa, H. Yoshida, A. Uehashi, et al., Electric current-controlled synthesis of $BaTiO_3$, J. Am. Ceram. Soc. 100 (2017) 3843–3850.

Chapter 2. Non-Uniform Sintering Behavior in Transparent Y_2O_3 during SPS

2.1. Introduction

Among the ceramic materials that can be applied to laser applications, single-crystalline Y_2O_3 has been researched worldwide [1–4]. It has suitable properties for laser applications (high thermal conductivity, chemical stability, and low phonon energy) and has the advantage of being easily doped with rare-earth ions. However, polycrystalline ceramic laser technology is emerging to overcome the technology and cost problems caused by single-crystal [5–8]. Compared with single-crystal ceramics, the merit of polycrystalline transparent ceramics is that they can be fabricated in larger volumes to obtain high-power lasers, and even a complicated shape can be applied to various types of gain media.

The fabrication of polycrystalline transparent ceramics with high oscillation efficiency requires ceramic processes that include appropriately synthesized powder and sintering technologies with advanced sinterability. Recently, vacuum sintering, hot isostatic pressing (HIP), spark plasma sintering (SPS), and flash sintering (FS) have been developed to remove residual pores effectively [9–12]. Compared with conventional sintering, the SPS technology that combines uniaxial pressure with heating by an electrical current has a great potential for fabricating functional laser ceramics [1]. Due to the direct heating of the mold and powder by electric current, full densification at low temperatures and fine microstructures can be obtained [13–20]. Rapid densification and fine microstructures, which are advantages of SPS, improve the mechanical and optical properties of transparent ceramics.

However, in attempting to maximize the advantages of SPS, some problems in the SPS process have been observed when sintering at lower temperatures and higher heating rates. Various research groups have reported this problem investigating transparent ceramics with

SPS, and the appearance of a non-uniformly sintered sample has been observed. For example, in the Al_2O_3 and Y_2O_3 fabricated by SPS, non-uniform sintering behavior was reported at various temperatures (1000–1200°C) [18–20]. However, as for the phenomena causing the appearance of the sintered sample to be different, the reasons and processes claimed by each group are different. For the first time, Grasso et al. [18] reported that the opaque portion of the center caused by the residual pores affected the formation of non-uniform sintering behavior. They proposed that the main factor for the residual pores is the temperature gradient caused by the low thermal conductivity of the starting powder (alumina) and the high heating rate of the SPS process. Next, Ratzker et al. [19,20] proposed that because a stress gradient exists in powder compacts due to a significantly high loaded pressure (500 MPa), the difference in grain growth between the center and the periphery was a major factor in the non-uniform sintering behavior. When Y_2O_3 was sintered at a high heating rate of 20°C/min, a white and opaque portion formed at the center, and a change in appearance was observed. Scanning electron microscopy (SEM) observation revealed that the white and opaque portion in the center area had noticeably increased grain sizes and intergranular pores [21]. It was confirmed that non-uniform sintering is related to differences in microstructures.

In the various ceramic materials produced by SPS, a significant difference in the appearance of the sintered sample according to the heating rates and loaded pressure has been reported. In previous work, the non-uniform sintering behavior of SPSed Y_2O_3 was induced by non-uniform coarsening between the center and the periphery caused by the movement of defects and increased grain boundary mobility. However, the reasons claimed by the various groups were inappropriate to explain the non-uniform sintering behavior. First, it was considered that the temperature gradient that occurred within a 10 mm diameter would be insufficient to induce the significant difference in grain size between the center and the periphery obtained in the present work. Therefore, the main mechanism (Grasso et al. [18])

was excluded because it was inappropriate for interpreting the non-uniform sintering behavior in the present work. Since the non-uniform sintering behavior occurred even though a conventional loaded pressure (80 MPa) was applied, the proposed interpretation (Ratzker et al. [19,20]) that the stress gradient resulting from significantly high loaded pressure (500 MPa) was the main factor is inappropriate. Currently, the demonstration of the assumption was also insufficient.

The main purpose of this study is to investigate non-uniform sintering behavior with the demonstration of the assumption as the defect diffusion to the center and matter diffusion to the periphery. Through detailed microstructural and spectroscopy analysis, the electric field effects led the defects generation and diffusion into the center region, resulting in accelerating the grain boundary mobility and coarsening the microstructure. The differences in the extent of microstructure coarsening induced the non-uniform sintering behavior with an opaque portion in the center.

2.2. Experimental Procedure

The starting powder was commercial Y_2O_3 powder (99.99%, UU-type; Shin-Etsu Rare Earth, Japan) with a manufacturer-determined average particle size of 0.1–0.3 μm. The as-received Y_2O_3 powder was densified with an SPS machine to obtain dense and translucent Y_2O_3 under a vacuum atmosphere of 10 Pa. The powder (0.6 g per sintered Y_2O_3) was directly sintered in a vacuum without any pretreatment, using a graphite mold with an inner diameter of 10 mm. The sintering temperature (1000°C) and pressure (80 MPa) were fixed, and the heating rates and holding times were varied. Up to 600°C, the mold was heated at a 50°C/min, and then at 5 and 20°C/min. After reaching the sintering temperature (1000°C), the sintered Y_2O_3 was cooled after holding for 2, 5, 20, and 60 min. The optical appearance of the sintered Y_2O_3 varied with the heating rate and holding time, so it was set as a variable. Heating was conducted using direct current (DC) pulses without zero current, and the temperature was measured using a thermocouple in the non-through hole of the mold. The mold was covered with carbon felt to reduce heat dissipation. For transmission electron microscopy (TEM) analysis of each region in the non-uniformly sintered Y_2O_3, a thicker sintered Y_2O_3 was fabricated in addition. Y_2O_3 powder (1.5 g) was sintered at 1000°C with a heating rate of 5°C/min under 80 MPa and then cooled after holding for 20 min.

Both sides of the sintered Y_2O_3 were mirror polished, and Fourier-transform infrared (FT-IR) spectra were measured in a range of 1000–4000 cm^{-1} using an FT-IR spectrometer (Nicolet 6700 FT-IR Spectrometer, Thermo Fisher Scientific, USA). In order to analyze the cross-section, the sintered Y_2O_3 was cut into two pieces at intervals of 2 mm. The two pieces were mirror polished, and one of the pieces was thermally etched at 850°C for 2 h in the air for SEM analysis. The polished surfaces were observed via SEM (SU-8000, Hitachi, Japan). The porosity and pore distribution were evaluated from area fractions of pores on SEM photographs. In order to analyze the carbon and undefined materials, Raman spectra were collected by a laser Raman spectrometer (NRS-4100, JASCO, Japan). For a cross-sectional TEM observation, thin foil specimens of the sintered Y_2O_3 were prepared using a focused ion beam milling method. The cross-sectional observation was performed using TEM equipment (TITAN^{TM} X-FEG, Thermo Fisher Scientific, USA) operated at an acceleration voltage of 300 kV.

2.3. Results and Discussion

2.3.1. Appearance and Microstructure of Each Sintered Y_2O_3

The appearances of sintered Y_2O_3 at various heating rates (5 and 20°C/min) and holding times (0, 5, 20, and 60 min) are shown in Fig. 16. Various factors such as heating rates, holding times, and mold materials affect various ceramic materials sintered with SPS technology. In the case of Al_2O_3 and $MgAl_2O_4$ sintered by SPS, a significant difference has been reported in the appearance of the sintered sample according to the heating rate. Besides, in the SPS of Lu_2O_3, a discussion on the difference between the loaded pressures and the heating rates has been reported. In the present work, the heating rates and holding times, which had a significant influence, were set as main variables. At a low heating rate (5°C/min), uniform sintering behavior was observed every holding time. On the other hand, at a high heating rate (20°C/min), sintered Y_2O_3, held for more than 5 min at 1000°C, had a non-uniform appearance and microstructure. In the non-uniformly sintered Y_2O_3, a white and opaque portion was created at the center, while the periphery of the sintered Y_2O_3 was translucent. Irrespective of each sintering behavior, the center region sintered at both heating rates was sufficiently densified at the early holding stage (0 min), as shown in Fig. 16. Non-uniform sintering behavior then occurred with longer holding times in Y_2O_3 sintered at a high heating rate (20°C/min). It can be interpreted that the sintering of Y_2O_3 proceeded sufficiently for both heating rates, although some other factors produce opaque parts during sintering at 20°C/min.

XRD patterns of SPSed Y_2O_3 ceramics at 1000°C with various heating rates (5 and 20°C/min) and holding times (20 and 60 min). Despite the different heating rates and sintering behavior, only Y_2O_3 peaks were detected in all samples. No differences were observed either in the order of the intensities of the major peaks and the full-width at half maximum (FWHM). The XRD pattern proves that it is purely composed of Y_2O_3 ceramics regardless of the heating rate and sintering behavior, as shown in Fig. 17.

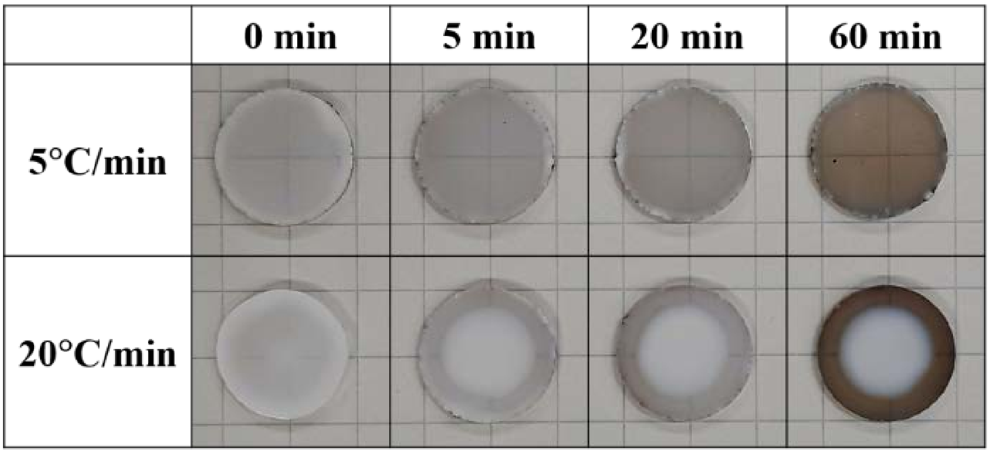

Fig. 16. Optical appearances of SPSed Y_2O_3 ceramics at 1000°C with various heating rates (5 and 20°C/min) and holding times (0, 5, 20, and 60 min).

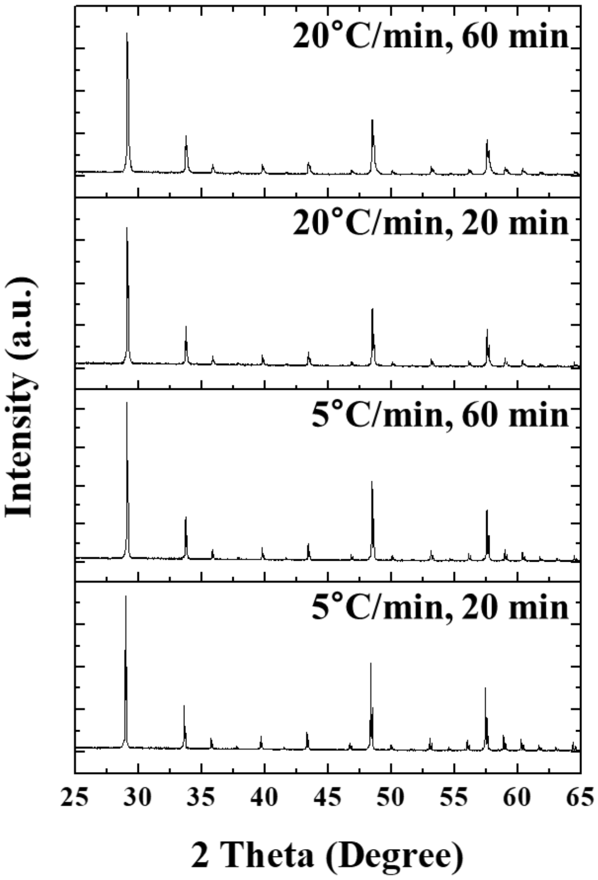

Fig. 17. XRD patterns of SPSed Y_2O_3 ceramics at 1000°C with various heating rates (5 and 20°C/min) and holding times (20 and 60 min).

The main goal of the present work was to analyze the difference in microstructure according to the heating rate. The two specimens sintered for 20 min at different heating rates (5 and 20°C/min) were suitable candidates because of apparent differences. The cross-section of the sintered Y_2O_3 was divided into four-point parts with a distance between each point of 1.5 mm from the center "1" to the periphery "4," as shown in the schematic diagram of Fig. 18 (a). The Y_2O_3 sintered at a heating rate of 20°C/min in Fig. 18 (c) shows different pore sizes and porosities depending on the region (center or periphery). The periphery (c-4) shows a smaller pore size and lower porosity, while the opposite tendency is observed at the center (c-1). In addition, the pore size was clearly observed to decrease (125 → 47 nm), as well as the porosity decrease (11.3 → 1.4%) from the center (c-1) to the periphery (c-4). Notably, no difference in pore distribution was observed in uniformly sintered Y_2O_3 with a heating rate of 5°C/min in Fig. 18 (b). This result sufficiently supports the interpretation that defects moved to the center, and subsequently, mass transfer to the periphery occurred.

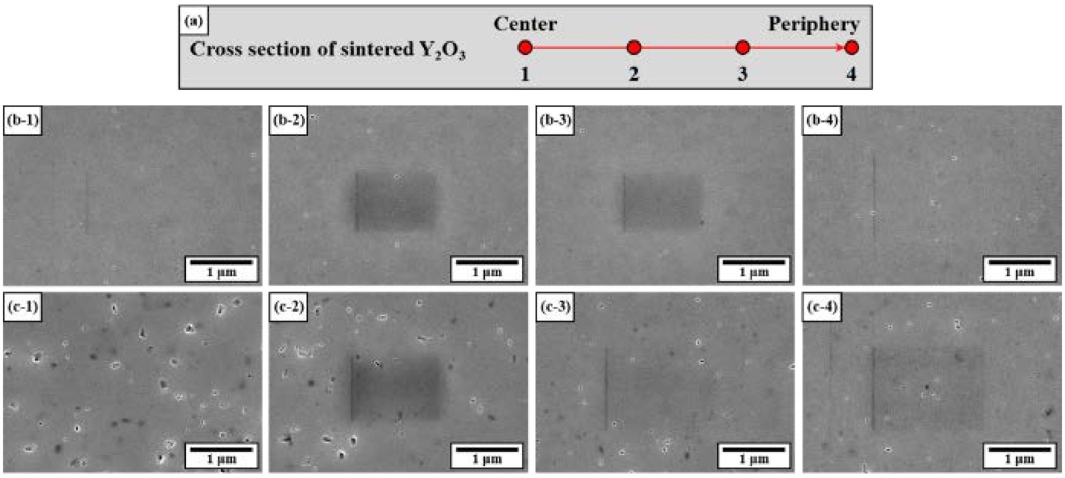

Fig. 18. (a) Schematic diagram of positions 1, 2, 3, and 4 in the cross-sectional SEM specimens, and SEM images of sintered Y_2O_3 at 1000°C with 5°C/min (b) and 20°C/min (c) for 20 min.

For non-uniformly sintered Y_2O_3, a sintered Y_2O_3 approximately 1.8 mm thicker than previous specimens (about 0.8 mm) was fabricated to analyze the detailed microstructures. The sintered Y_2O_3 with a thickness of 0.8 mm was so small that it was impossible to prepare specimen pieces for each region. Therefore, Y_2O_3 was thickly sintered to a thickness of 1.8 mm, was fabricated to prepare specimen pieces for each region. The additional sintered Y_2O_3 was consolidated by heating to 1000°C at 5°C/min for 20 min. SEM and optical images of the microstructure for each region prior to detailed microstructural analysis (TEM) are summarized in Fig. 19. A white and opaque portion in the center and translucent portions on the periphery were observed in Fig. 19 (a). The microstructures at the center and periphery are shown in Fig. 19 (b, c), respectively. From the above results, in the case of sintered Y_2O_3 with a thickness of 0.8 mm, uniformly sintered Y_2O_3 was obtained by sintering at a low heating rate (5°C/min). However, in the case of thicker sintered Y_2O_3 (1.8 mm), non-uniform sintering behavior occurred despite the heating rate being the same (5°C/min). With the same sintering conditions, the sintering behavior varies depending on the thickness of the sintered sample or the amount of powder. The SPS proceeds by passing an electric current corresponding to the heating rate. When the heating rate is high or the amount of loaded powder is large, a stronger electric current and a higher current density are applied to the SPS process. Since rapid densification is accompanied by high current density during the SPS process, despite the sintering conditions being the same, the sintered Y_2O_3 with a thickness of 1.8 mm was sintered non-uniformly at a low heating rate (5°C/min). A summary of the microstructural properties is as follows: the average grain size, d; the porosity, f; and the average pore size, p; were, respectively, d = 432 nm, f = 14.4%, and p = 104 nm at the center region, while they were d = 163 nm, f = 2.8%, and p = 29 nm in the periphery region. The difference in porosity between the center (f = 14.4%) and the periphery (f = 2.8%) was driven by the effect of mass transfer from the center to the periphery and the diffusion of defects to the center [21].

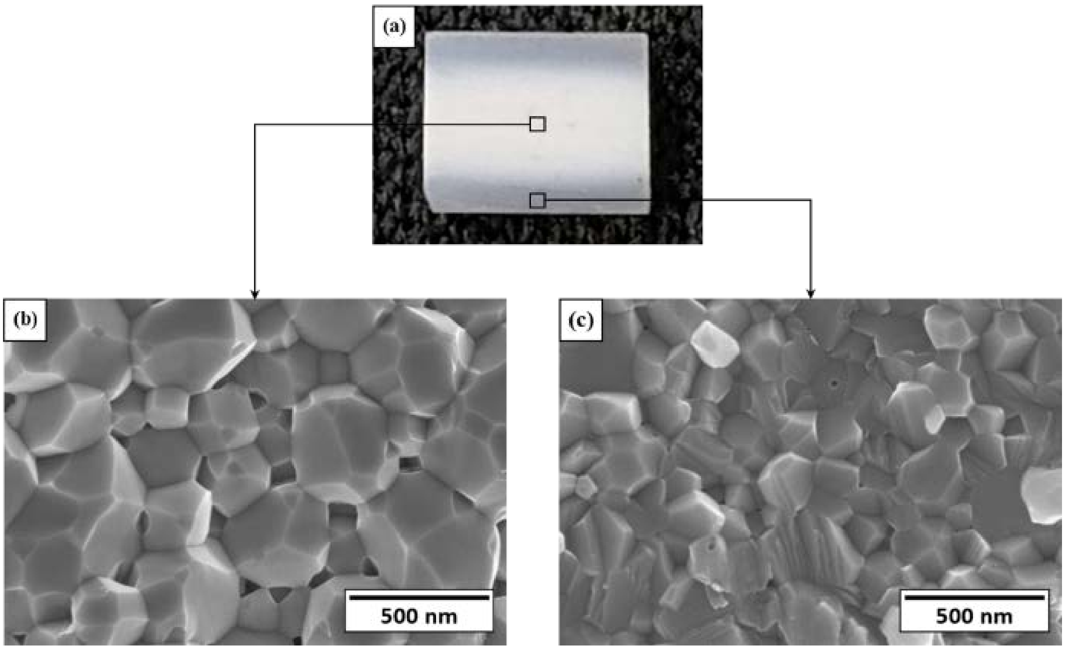

Fig. 19. Optical (a) and cross-sectional SEM images at the center (b) and periphery (c) of non-uniformly sintered Y_2O_3 at 1000°C with a 5°C/min heating rate for 20 min.

In addition to the SEM analysis above, a TEM analysis was performed to investigate the more detailed microstructures of the sintered Y_2O_3. The microstructure of the center is shown in Fig. 20 (a, b), and that of the periphery is shown in Fig. 20 (c, d); the magnification in Fig. 20 (a, c) is higher than that in Fig. 20 (b, d). The TEM analysis also provided detailed porosity, pore size, and pore distribution. In the center region (Fig. 20 (a, b)), all of the pores were located at grain boundary junctions (intergranular pores), and the average pore size (p = 115 nm) and porosity (f = 11.2%) were significantly larger than those at the periphery (Fig. 20 (c, d)). On the other hand, the pore sizes in the periphery region are 1–30 nm, and these tiny pores tend to be distributed within the grains. The high-magnification TEM image of the periphery for Fig. 20 (c, d) shows that pores of 1–30 nm are distributed within each grain. With TEM analysis at high magnification, such intragranular pores were not observed in the center region, and intragranular pores were predominant at the periphery. This result suggests noticeable microstructural coarsening in the center region but very little in the periphery region: in the center region, the grains and pores increased in size significantly due to the dramatic coarsening.

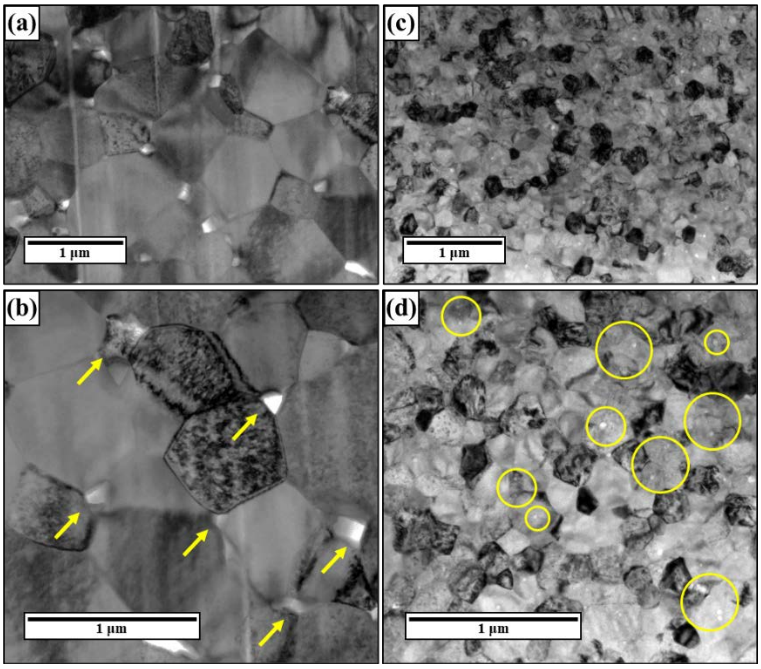

Fig. 20. TEM images of the center (a, b) and periphery (c, d) regions in sintered Y_2O_3 at 1000°C for 20 min at 5°C/min. The magnification in (b, d) is higher than that in (a, c).

2.3.2. Interpretation and Discussion of Non-Uniformly Sintered Y_2O_3

The mechanism for the non-uniform sintering behavior proposed in the present work differs from that of the other groups. Grasso et al. [18] proposed that the main factor for the residual pores is the temperature gradient caused by the low thermal conductivity of the starting powder (alumina) and the high heating rate of the SPS process. It was considered that the temperature gradient occurring within a 10 mm diameter would be insufficient to induce the significant difference in grain size between the center and the periphery obtained in the present work. Compared to the experiments of Ratzker et al. [19,20], because the non-uniform sintering behavior occurred even though a conventional loaded pressure (80 MPa) was applied, the proposed interpretation that the stress gradient resulting from significantly high loaded pressure

(500 MPa) was the main factor is inappropriate. A modified mechanism was proposed to interpret the non-uniform sintering behavior in the present work appropriately.

Through SEM and TEM analysis, it was possible to sufficiently demonstrate the differences in microstructures related to non-uniform sintering behavior [21]. As with the TEM image of the periphery region (Fig. 20 (d)), lots of residual defects have been proven by the numerous tiny pores (yellow arrows in Fig. 20 (d)) in the grain. This is because the residual defects of sintered Y_2O_3 were transformed into numerous tiny pores. When there are a lot of residual defects inside rapidly densified Y_2O_3 due to the high heating rate, more defects diffuse into the center compared with the periphery [21]. In the SPS process using an electric field, lots of defects are known to increase grain boundary mobility. For this reason, the center region, in which the number of defects is higher than in the periphery region, has rapid grain growth and increased grain boundary mobility, as shown in Fig. 21. Due to rapid grain growth and increased grain boundary mobility, significant coarsening was induced, and grain and pore size were increased in the center region. Finally, during the sintering process, coarsening was more dominant than densification in the center region, and unlike in the periphery region, a dramatically coarsened microstructure was created. Based on the above analysis results, it was possible to discuss the differences in the appearance of the sintered Y_2O_3. Sintering the Y_2O_3 at a high heating rate (20°C/min) led to dramatic coarsening in the center compared with the periphery. Not only did the grain size increase, but the pore size and porosity also increased significantly. That is why this dramatic coarsening occurred noticeably in the center, resulting in an opaque appearance. Consequently, non-uniform sintering behavior occurred with significant differences in the microstructure and appearance between the center and periphery.

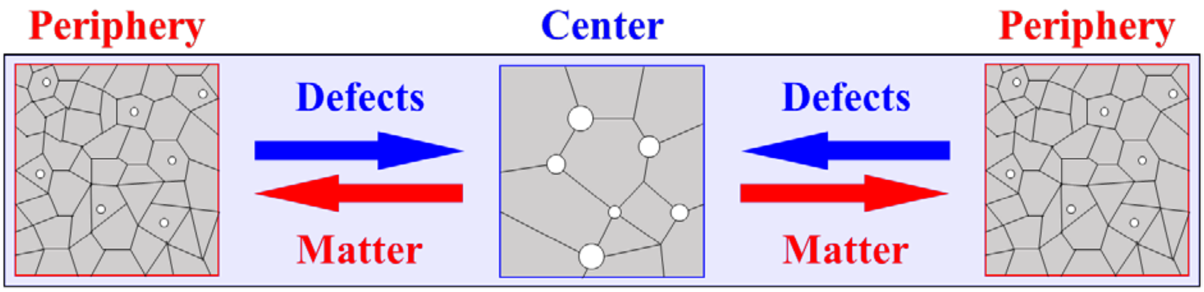

Fig. 21. Schematic diagram of microstructural evolution in non-uniform sintering behavior

Although the fabrication of transparent Y_2O_3 ceramics with similar SPS conditions has not yet been achieved, the possibility of preventing non-uniform sintering behavior is suggested. The carbon contamination and incidental oxygen vacancies were the major factors in accelerating matter and defect diffusion by strong electric fields in the non-uniformly sintered Y_2O_3. Therefore, suppressing carbon contamination and incidentally occurring oxygen vacancies may prevent non-uniform sintering behavior.

2.3.3. Spectroscopic Analysis

FT-IR spectra of SPSed Y_2O_3 at different heating rates (5 and 20°C/min) for 60 min showed the most obvious difference, so those are shown in Fig. 22. Two strong absorption peaks around 1500 cm^{-1} were most noticeable among all the spectra. Two peaks were observed irrespective of the heating rates and correspond to the C-O bond stretching vibration and bending belonging to the carbonate [25]. For the low heating rate (5°C/min), no absorption peaks were observed except for those around 1780 and 1500 cm^{-1}. Both peaks correspond to the C-O bond of the carbonate. The IR transmittance graph of the low heating rate (5°C/min) shows the same trend as that of the typical pattern of commercial Y_2O_3 [26]. However, in the case of the high heating rate (20°C/min), a difference was observed as compared to the typical IR transmittance graph of Y_2O_3. The peaks located at 2555 and 2950 cm^{-1} were very weakly detected at the low heating rate but clearly detected at the high heating rate. For the low heating rate, the strong absorption peak located at 3560 cm^{-1} was not observed at all, but the intensity increased significantly and became apparent as the heating rate increased. This peak is the O-H stretching band of H_2O. The reason is that H_2O adsorbed to the initial Y_2O_3 powder was not sufficiently removed and was trapped inside in the process of rapid densification due to the high heating rate. Additionally, two C-O bonding peaks corresponding to the carbonate were weakly detected around 1875 and 1780 cm^{-1}. The peaks corresponding to the carbonate were strongly detected in the non-uniformly sintered Y_2O_3 at the high heating rate, while the peaks were indistinct in the uniformly sintered Y_2O_3 at the low heating rate. Notably, a peak around 2340 cm^{-1} corresponded to CO_2 and was strongly detected in the non-uniformly sintered Y_2O_3. It was concluded that the SPS process, which was performed in a carbon-rich environment, inadvertently introduced carbon, and the carbon reacted with the O-H bands involved in the starting powder and was detected as carbonate and CO_2.

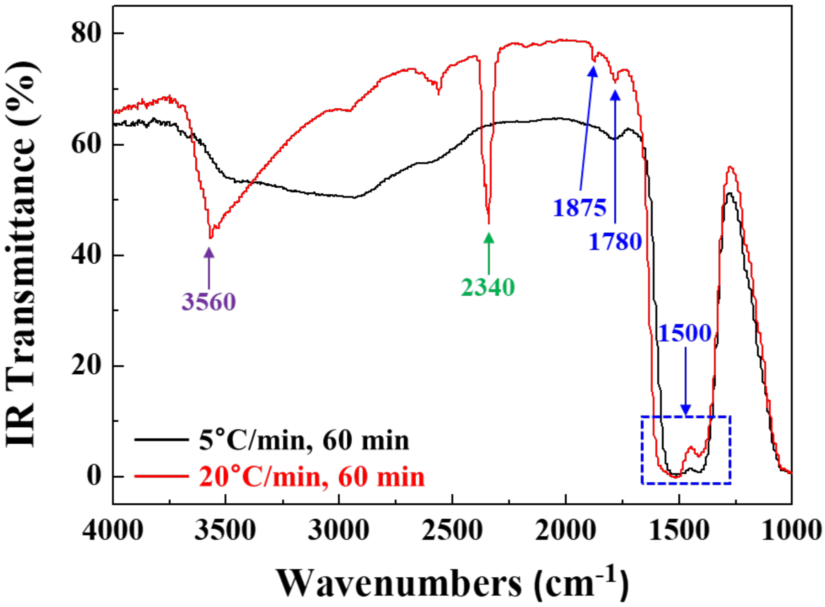

Fig. 22. FT-IR spectra of Y_2O_3 ceramics sintered at 1000°C for 60 min with 5°C/min (black profile) and 20°C/min (red profile).

Raman spectroscopy was performed, as shown in Figs. 23 and 24 depending on the heating rates, for a detailed analysis of carbon, because one can predict the introduction of carbon from a graphite punch, die, and carbon paper. Among all the Raman spectra, the same spectrum as that of the Y_2O_3 powder was detected in the peak at 2450 cm^{-1} and in the range below 1150 cm^{-1}. A difference in peak position depending on heating rates, a critical factor influencing the evolution of the sintering behavior, was not observed; only a small difference in intensity was observed. Results for a low heating rate (5 °C/min) with no appreciable differences in the intensities of the two broad bands detected in the 3000–3500 and 2100–2600 cm^{-1} ranges are shown in Fig. 23. In a high heating rate (20°C/min), which may occur the non-uniform behavior, the two broad bands of periphery region were significantly grew in Fig. 24. Two broad bands corresponding to O-H and C-O rapidly grew at the periphery in the non-uniformly sintered samples, which was consistent with the FT-IR spectra in Fig. 22. The non-uniform sintering behavior due to the high heating rates affected not only the microstructure but also the extent of carbon contamination and carbonate reaction; consequently, the sudden increase of O-H and C-O bands resulted in non-uniform appearances. In the Raman spectroscopy, no differences in the positions or existence of the peaks were observed irrespective of the heating rate, but as the holding time increased, the intensity of the wideband corresponding to O-H and C-O strains increased. In general, carbon contamination occurs as sintering proceeds in the SPS process. As a result, the amount of carbon contamination increases, and the reaction to the carbonate increases with the holding time.

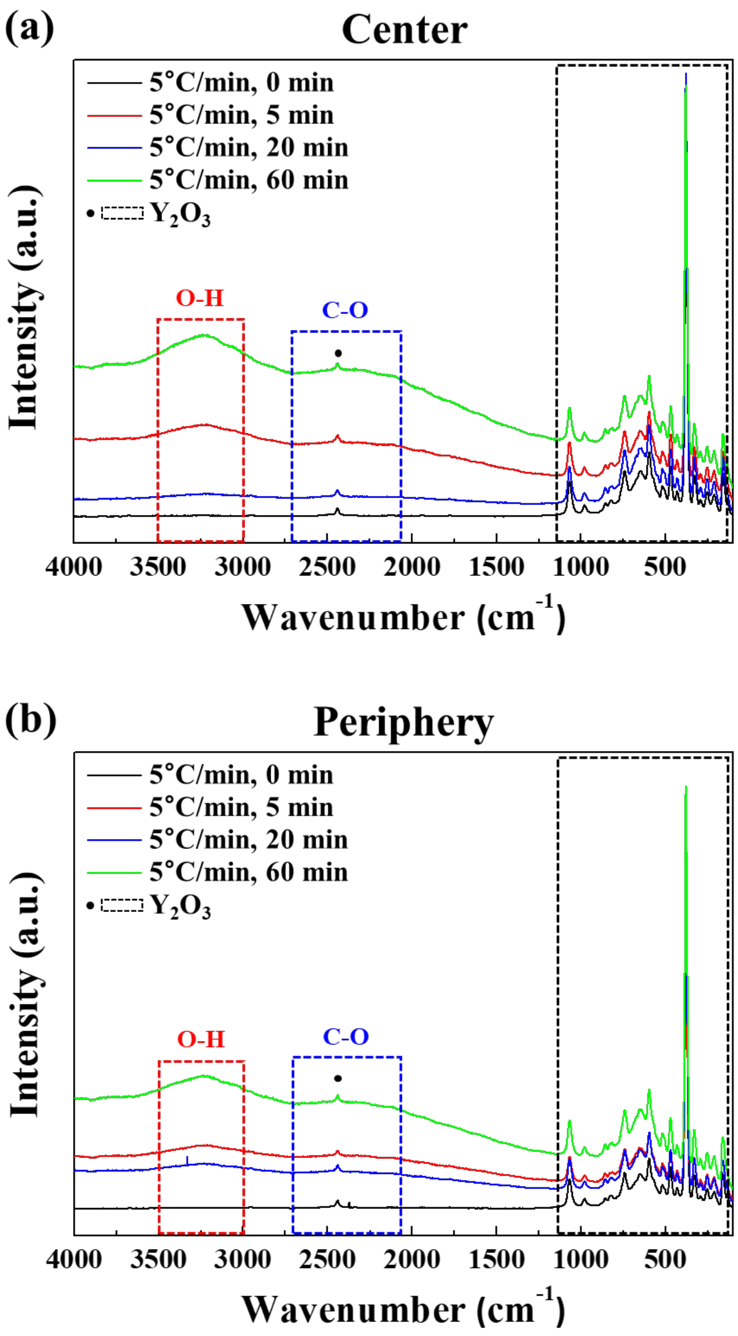

Fig. 23. Raman spectra of sintered Y_2O_3 in the (a) center and (b) periphery regions at 5°C/min for various holding times (0, 5, 20, and 60 min). Black rectangles drawn with broken lines indicate the peaks from Y_2O_3, red rectangles denote the O-H band, and blue rectangles denote the C-O band.

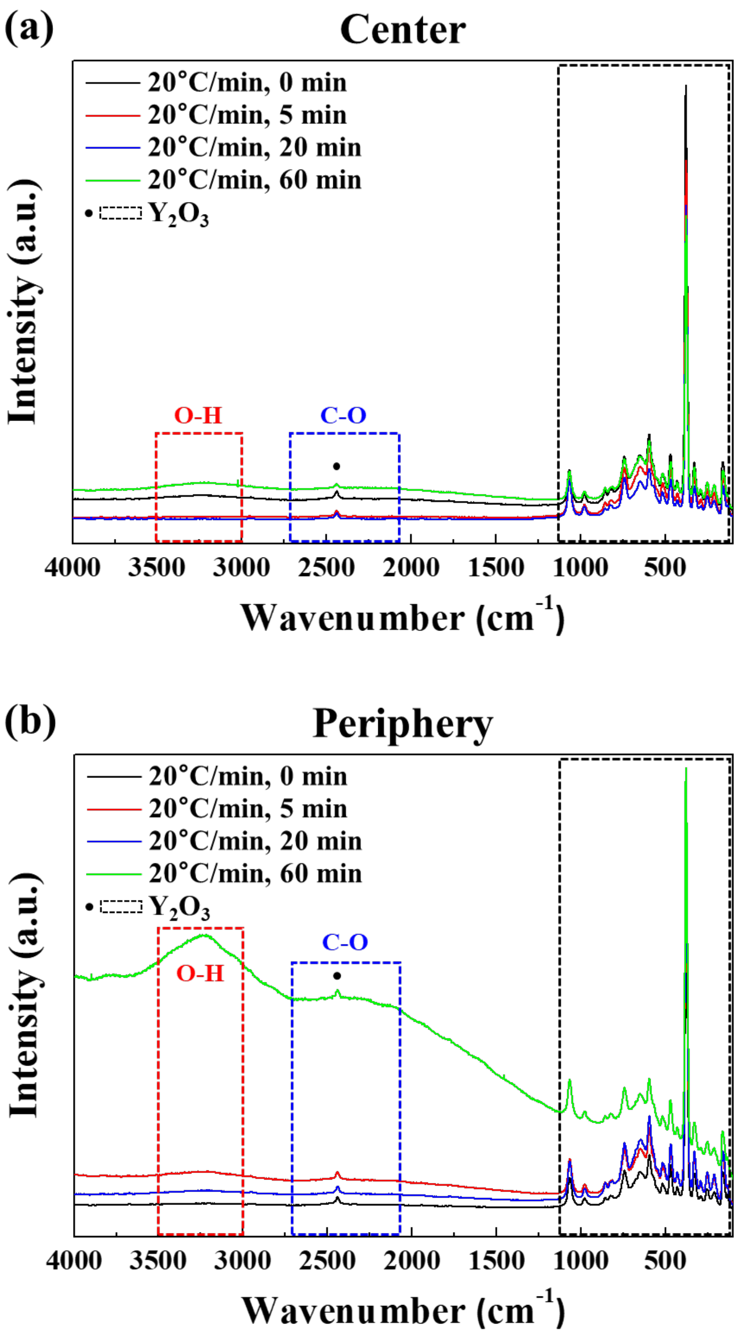

Fig. 24. Raman spectra of sintered Y_2O_3 in the (a) center and (b) periphery regions at 20°C/min for various holding times (0, 5, 20, and 60 min). Black rectangles drawn with broken lines indicate the peaks from Y_2O_3, red rectangles denote the O-H band, and blue rectangles denote the C-O band.

2.4. Conclusions

The non-uniform microstructure of SPSed Y_2O_3 was investigated by microstructural (SEM, TEM) and spectroscopic (FT-IR, Raman spectroscopy) analysis. In the SPS process with high heating rates, the non-uniform sintering behavior of Y_2O_3 was observed and accompanied by the differences in the appearances and microstructures. From the center to the periphery, the pore size, porosity, and grain size significantly decreased, and it was concluded that defects and pores gathered at the center, contrate to a uniformly sintered Y_2O_3. Due to the electric and magnetic fields in the SPS process, the defects lead to increased grain boundary mobility and coarsening. The center region's relatively large number of defects accompanied the rapid grain growth and coarsened microstructure. Consequently, during the SPS process, the coarsening was more dominant than the densification in the center and, unlike in the periphery, dramatically coarsened microstructures were induced. A carbon-rich environment unintentionally introduced the carbon, and it reacted with the -OH involved in the starting powder and was detected as the carbonate and CO_2. As the holding time increased, the intensity of the wide band corresponding to O-H and C-O strains increased. As a result, the amount of carbon contamination increased, and the reaction to the carbonate increased with the holding time.

References

[1] S. Ghosh, A. H. Chokshi, P. Lee, R. Raj, A huge effect of weak dc electrical fields on grain growth in zirconia, J. Am. Ceram. Soc. 92 (2009) 1856–1859.

[2] D. Yang, R. Raj, H. Conrad, Enhanced sintering rate of zirconia (3Y-TZP) through the effect of a weak dc electric field on grain growth, J. Am. Ceram. Soc. 93 (2010) 2935–2937.

[3] S. Nekahi, F.S. Moghanlou, M. Vajdi, et al., Microstructural, thermal and mechanical characterization of TiB_2-SiC composites doped with short carbon fibers, Int. J. Refractory Metal. Hard Mater. 82 (2019) 129–135.

[4] R. Chaim, Densification mechanisms in spark plasma sintering of nanocrystalline ceramics, Mater. Sci. Eng. A 443 (2007) 25–32.

[5] W. Chen, U.A. Tamburini, J.E. Garay, et al., Fundamental investigations on the spark plasma sintering/synthesis process 1. Effect of dc pulsing on reactivity, Mater. Sci. Eng. A 394 (2005) 132–138.

[6] U.A. Tamburini, S. Gennari, J.E. Garay, Z.A. Munir, Fundamental investigations on the spark plasma sintering/synthesis process 2. Modelling of current and temperature distributions, Mater. Sci. Eng. A 394 (2005) 139–148.

[7] H. Yoshida, K. Morita, B.N. Kim, er al., Reduction in sintering temperature for flash-sintering of yttria by nickel cation-doping, Acta Mater. 106 (2016) 344–352.

[8] R. Chaim, M. Kalina, J.Z. Shen, Transparent yttrium aluminum garnet (YAG) ceramics by spark plasma sintering, J. Eur. Ceram. Soc. 27 (2007) 3331–3337.

[9] F. Shayesteh, S.A. Delbari, Z. Ahmadi, et al., Influence of TiN dopant on microstructure of TiB_2 ceramic sintered by spark plasma, Ceram. Int. 45 (2019) 5306–5311.

[10] L.L Zhu, Y.J. Park, L. Gan, et al., Fabrication and characterization of highly transparent Er:Y_2O_3 ceramics with ZrO_2 and La_2O_3 additives, Ceram. Int. 43 (2017) 13127–13132.

[11] O. Guillon, J. Gonzalez-Julian, B. Dargatz, et al., Field-assisted sintering technology/spark plasma sintering: Mechanisms, Materials, and Technology Developments, Advanced Eng. Mater. 16 (2014) 830–849.

[12] O. Guillon, C. Elsasser, O. Gutfleisch, et al., Manipulation of matter by electric and magnetic fields: Toward novel synthesis and processing routes of inorganic materials, Mater. Today 21 (2018) 527–536.

[13] H. Yoshida, K. Morita, B.N. Kim, et al., Low-temperature spark plasma sintering of yttria ceramics with ultrafine grain size, J. Am. Ceram. Soc. 94 (2011) 3301–3307.

[14] R. Chaim, M. Levin, A. Shlayer, C. Estournes, Sintering and densification of nanocrystalline ceramic oxide powders: a review, Advances in Applied Ceram. 107 (2008) 159–169.

[15] H. Zhang, B.N. Kim, K. Morita, et al., Fabrication of transparent yttria by high-pressure spark plasma sintering, J. Am. Ceram. Soc. 94 (2011) 3206–3210.

[16] R. Chaim, A. Shlayer, C. Estournes, Densification of nanocrystalline Y_2O_3 ceramic powder by spark plasma sintering, J. Eur. Ceram. Soc. 29 (2009) 91–98.

[17] H. Furuse, S. Nakasawa, H. Yoshida, et al., Transparent ultrafine Yb^{3+}:Y_2O_3 laser ceramics fabricated by spark plasma sintering, J Am Ceram Soc. 101 (2018) 694–702.

[18] B.N. Kim, K. Hiraga, K. Morita, et al., Microstructure and optical properties of transparent alumina, Acta Mater. 57 (2009) 1319–1326.

[19] S. Grasso, C. Hu, G. Maizza, et al., Effects of pressure application method on transparency of spark plasma sintered alumina, J. Am. Ceram. Soc. 94 (2011) 1405–1409.

[20] B.N. Kim, K. Hiraga, S. Grasso, et al., High-pressure spark plasma sintering of MgO-doped transparent alumina, J. Japan Ceram. Soc. 120 (2012) 116–118.

[21] B.N. Kim, K. Hiraga, K. Morita, et al., Dynamic grain growth during low-temperature spark plasma sintering of alumina, Scripta Mater. 80 (2014) 29–32.

[22] K. Morita, B.N. Kim, H. Yoshida, et al., Distribution of carbon contamination in $MgAl_2O_4$ spinel occurring during spark-plasma-sintering (SPS) processing: I – Effect of heating rate and post-annealing, J. Eur. Ceram. Soc. 38 (2018) 2588–2595.

[23] B. Ratzker, A. Wagner, M. Sokol, et al., Optical and mechanical properties of transparent alumina fabricated by high-pressure spark plasma sintering J. Eur. Ceram. Soc. 39 (2019) 2712–2719.

[24] B.N. Kim, A. Dash, Y.W. Kim, et al., Low-temperature spark plasma sintering of alumina by using SiC molding set, J. Ceram. Soc. Japan 124 (2016) 1141–1145.

[25] M. Michálek, M. Michálková, G. Blugan, J. Kuebler, Effect of carbon contamination on the sintering of alumina ceramics, J. Eur. Ceram. Soc. 38 (2018) 193–199.

[26] M.A. Clark, T.H. Alden, Deformation enhanced grain growth in a superplastic Sn-1% Bi alloy, Acta Mater. 21 (1973) 1195–1206.

Chapter 3. Fabrication of Highly Transparent Y_2O_3 by Two-Step SPS

3.1. Introduction

Y_2O_3 is one ceramic material used extensively in industrial applications due to its excellent optical, electrical, and thermal properties [1]. Particularly, transparent Y_2O_3 ceramics exhibits outstanding optical transmission over a wide range of wavelengths, with an excellent signal-to-noise ratio [2]. In addition, as a host material of high-powder laser gain media, research on transparent polycrystalline Y_2O_3 is actively conducted [3–5]. Facilitating laser oscillation for transparent ceramic requires light transmittance equivalent to a single crystal, which is close to the theoretical value. Laser oscillation is difficult because oscillation hardly occurs even if only 0.1% of pores remain in transparent functional ceramics. It is difficult to make transparent ceramics manufactured only by sintering using powder as a raw material due to the difficulty of completely removing pores. Thus, various sintering techniques have been developed to fabricate high-quality transparent polycrystalline ceramics. Among them, spark plasma sintering (SPS), which is also called field-assisted sintering technology (FAST) or pulsed electric current sintering (PECS), can be applied to fabricate highly densified pellets using advanced sinterability efficiently. In the SPS process, due to mechanical pressure and electrical current applications, full densification can be achieved at lower temperatures with finer microstructures, as compared to the conventional sintering process [6–8]. However, some serious problems have also been reported, including non-uniform sintering [9–11]. When Al_2O_3 and Y_2O_3 were sintered at high heating rates, non-uniform appearance and microstructure of the translucent periphery and opaque center were observed. The opaque central region contains many large pores, significantly lowering optical transmission. In order to fabricate transparent ceramics for optical applications, such pores should be removed, and uniform sintering should be achieved.

Considerable research to improve the uniformity and optical properties of sintered samples by optimizing the detailed conditions of the SPS process has been reported [12–16]. There is also a fundamental solution to the problem of decreasing the heating rate or changing the holding times; however, research has reported applying the two-step sintering method, which has been applied in conventional sintering, in the SPS technology. First, a two-step sintering profile can be applied to SPS technology in terms of the applied pressure. Talimian et al. [12] suggested that applying pressure in the critical temperature range (1150–1250°C) is very effective at preventing carbon contamination, producing uniformity of sintered samples, and removing residual defects. Furuse et al. [13,14] reported applying pressure up to 82.7 MPa between 900–1200°C during the SPS process. As a result, excellent transparency close to the theoretical transmittance was obtained in Yb-doped Y_2O_3 sintered samples. In the case of loading the maximum pressure before heating, high stresses may concentrate at small regions where the powders contact each other, forming strong bonds between particles. The formation of strong bonds easily increases the number of residual pores, which lowers in-line transmittance by increasing the number of closed pores. In contrast, the significant improvement of transmittance can be achieved by reducing the residual pores, which may occur by enhanced matter diffusion and plastic deformation caused by high-temperature loading. Therefore, the loading pressure at high temperatures has proven to be enhanced transmittance effectively. Next, some research has been reported that densification and transparency could be improved by applying a two-step heating profile [15,16]. In the results reported by Nanko's group [15,16], after achieving sufficient densification with minimal grain growth when the first-step temperature was lower than the second-step (main) temperature, sufficient densification and excellent transparency could be obtained by removing the residual defects at the second-step temperature.

The main objective of this chapter is that a two-step heating and pressure profile, determined based on the range to which shrinkage occurs *via* the SPS shrinkage curve, is applied to fabricate a transparent Y_2O_3 ceramic. In the two-step pressure profile, the high-temperature loading of maximum pressure (80 MPa) improved the densification behavior, and as a result, an improvement in transmittance of 80.6% was achieved close to the theoretical value (81.6% at 1100 nm). Compared to the single-step SPS profile, the two-step heating and pressure profiles effectively solved the problems of non-uniformity and residual defects and are expected to be applied as a more suitable sintering profile for the fabrication of highly transparent ceramics.

3.2. Experimental Procedure

Commercial Y_2O_3 powder (99.99%, YY-13-20-0240, Rare Metallic Co. Ltd., Japan) with a manufacturer-determined average particle size of 4 ± 1 μm was jet-milled using an ultra-high-pressure wet-type atomizer (NanoVaterTM, Pacific Technology Corp., Japan). Jet-milled Y_2O_3 powder was dried in an oven for 48 h, followed by sieving with a 250-mesh screen. The sieved Y_2O_3 powder (1.0 g per sintered Y_2O_3) was consolidated with an SPS machine (LABOX-315, SinterLand Inc., Japan) for dense and transparent Y_2O_3 under a vacuum atmosphere (10 Pa). The powder was consolidated using a graphite mold with an inner diameter of 10 mm and the mold was covered with carbon felt to reduce heat dissipation. The inner wall of the graphite die was covered, and the surfaces of the punches were also separated from the powder by graphite sheets. During the SPS process, the temperature was measured using a pyrometer in the non-through hole of the mold.

In the case of the single-step SPS profile, a mechanical pressure of 80 MPa (6.5 kN) was loaded from the beginning and was maintained until before cooling. The powder compact was heated to 800°C with a heating rate of 20°C/min, and to 1500°C (sintering temperature) with 5°C/min. After reaching to sintering temperature, the powder compact was held for 20 min. Cooling was proceeded to 1100°C for 10 min, to 800°C for 5 min, and to 25°C for 5 min. In this experiment, the two-step SPS profile (heating and pressure profiles) optimized to fabricate the transparent Y_2O_3 is as follows. In the first-step SPS, the powder compact was heated to 800°C with a heating rate of 20°C/min, to 1250°C with 5°C/min and was held for various holding times (0, 30, 60, and 120 min). After the holding time at first-step, the temperature was increased to second-step temperature (1300, 1400, 1500, and 1600°C) with 5°C/min and held for 20 min under the 80 MPa. Then, sintered Y_2O_3 was cooled to 1100°C for 10 min, to 800°C for 5 min, and to 25°C for 5 min. In the early stage of the SPS process, the pressure for maintaining current conductivity was 6.36 MPa (0.5 kN) before heating. The main mechanical pressure was increased to 80 MPa (6.5 kN) between 800–1250°C for 90 min. The sintering conditions and specimen names are summarized in Table 4. To remove the carbon contamination and oxygen vacancies in sintered Y_2O_3 ceramics, further heat treatment (annealing) was carried out at 1000°C for 30 h in an air atmosphere using a box furnace.

Table 4. Experimental conditions (two-step pressure and heating profile) of SPSed Y_2O_3 ceramics.

Specimen Name	**Heating Profile**	
	Holding time at 1st step (1250°C)	**Sintering temperature at 2nd step**
T1300-30	30 min	1300°C
T1400-30	30 min	1400°C
T1500-30	30 min	1500°C
T1600-30	30 min	1600°C
S1500	-	1500°C
T1500-0	0 min	1500°C
T1500-60	60 min	1500°C
T1500-120	120 min	1500°C

Both sides of the SPSed and annealed Y_2O_3 were ground to a thickness of around 1 mm and mirror polished. Fourier-transform infrared (FT-IR) spectra were measured in a range of 2–9.5 μm using an FT-IR spectrometer (Nicolet 6700 FT-IR Spectrometer, Thermo Fisher Scientific Inc., USA). The XRD analysis was carried out for the Y_2O_3 powder and sintered Y_2O_3 using an X-ray diffractometer (SmartLab SE, Rigaku Co., Japan). In-line transmittance (ILT) measurements were conducted using a double-beam spectrophotometer (SolidSpec-3700DUV, Shimazu Co. Ltd., Japan) equipped with an integrating sphere. To analyze the cross-section, the sintered Y_2O_3 was cut, and mirror polished. The specimens for scanning electron microscopy (SEM) were thermally etched at 1000°C for 10 h in the air. The polished surfaces were observed by SEM (SU-8000, Hitachi Ltd., Japan).

3.3. Results and Discussion

3.3.1. Appearance and Microstructure of SPSed Y_2O_3

Fig. 25 shows the Y_2O_3 ceramics after annealing, through which characters are visible. The characters are most clearly seen through specimen T1500-60, and characters behind specimen T1500-30 were clearly observed the second time. Among the specimens depending on the second-step temperature (T1300-30, T1400-30, T1500-30, and T1600-30), the second-step temperatures of T1300-30 and T1400-30 were insufficient compared to 1500°C; as a result, the characters were clear. On the other hand, because of over-sintering T1600-30, which was sintered at 1600°C (second-step temperature), the characters were not clear, and carbon contamination was not fully eliminated after annealing at 1000°C for 30 h. Thus, the second-step temperature (the main sintering temperature) was selected as the reference temperature of 1500°C. Characters behind specimen S1500, which was SPSed with a single-step profile, and specimen T1500-0, which was SPSed with a two-step pressure profile, were less clear than specimen T1500-30. The clearest characters were observed in the T1500-60 specimen; as a result, among the various holding times at the first-step, 60 min produced the best appearance.

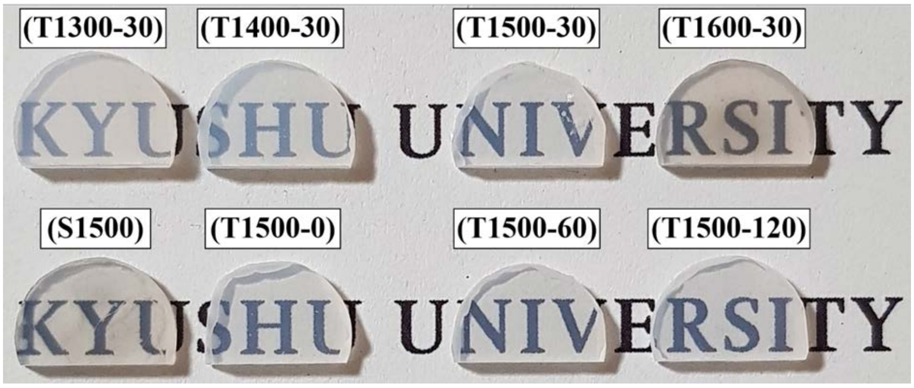

Fig. 25. Optical appearances of Y_2O_3 ceramics sintered with various sintering temperature and profiles summarized in Table 4.

The microstructure after annealing is shown in Fig. 26. With the second-step temperature, the grain size increased from 1.2 μm at 1300°C to 4.3 μm at 1600°C. Due to the same second-step temperature (1500°C), the grain sizes of specimen T1500-0, T1500-30, T1500-60, T1500-120, and S1500 were almost similar as shown in the SEM image. In all the specimens, the significant pores were observed very rarely, and any secondary phase particles were not observed at all. Because the pore is an important factor in discussing transmittance, the pore size was measured as follows. The specimen T1500-30 was about 180 nm, T1500-60 was less than 100 nm, T1500-120 was about 270 nm, and S1500 was about 340 nm. In the two-step profile, primary densification is achieved by suppressing excessive coarsening (grain and pore growth) at the relatively low temperature in first-step sintering, then fully densified microstructure is obtained in the second-step sintering. Therefore, in a specimen sintered with a two-step profile, smaller pore size was able to obtain compared to a single-step profile. The smaller pore size can be expected to have better transmittance in transparent ceramics.

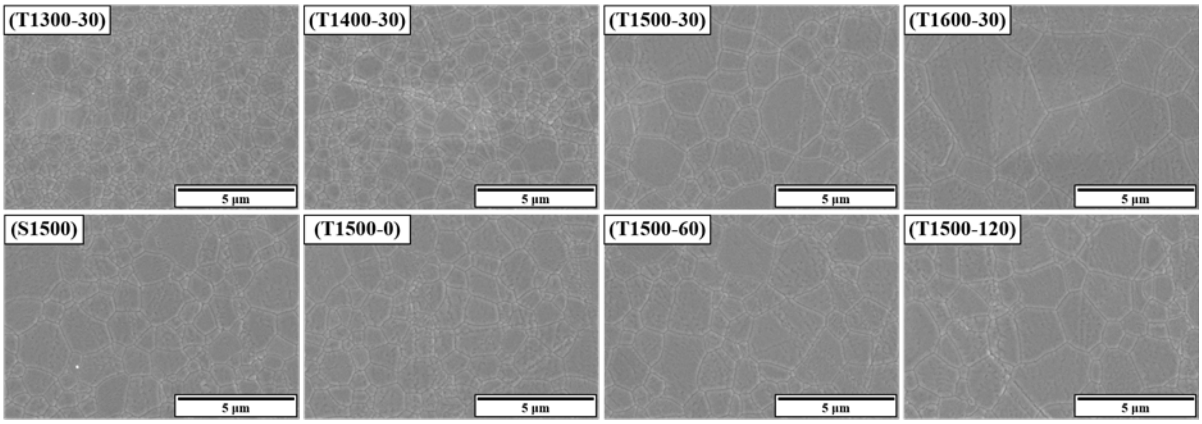

Fig. 26. SEM images of Y_2O_3 ceramics sintered with various sintering temperature and profiles summarized in Table 4.

Depending on the second-step temperature, the X-ray diffraction patterns of the Y_2O_3 powder and two-step SPSed Y_2O_3 ceramics are shown in Fig. 27. All diffraction patterns coincided with the pure cubic Y_2O_3 phase (JCPDS cards No. 41-1105). In addition, depending on the second-step temperature and SPS profiles, the second-phase peaks, phase transformation, and peak shifting were not observed.

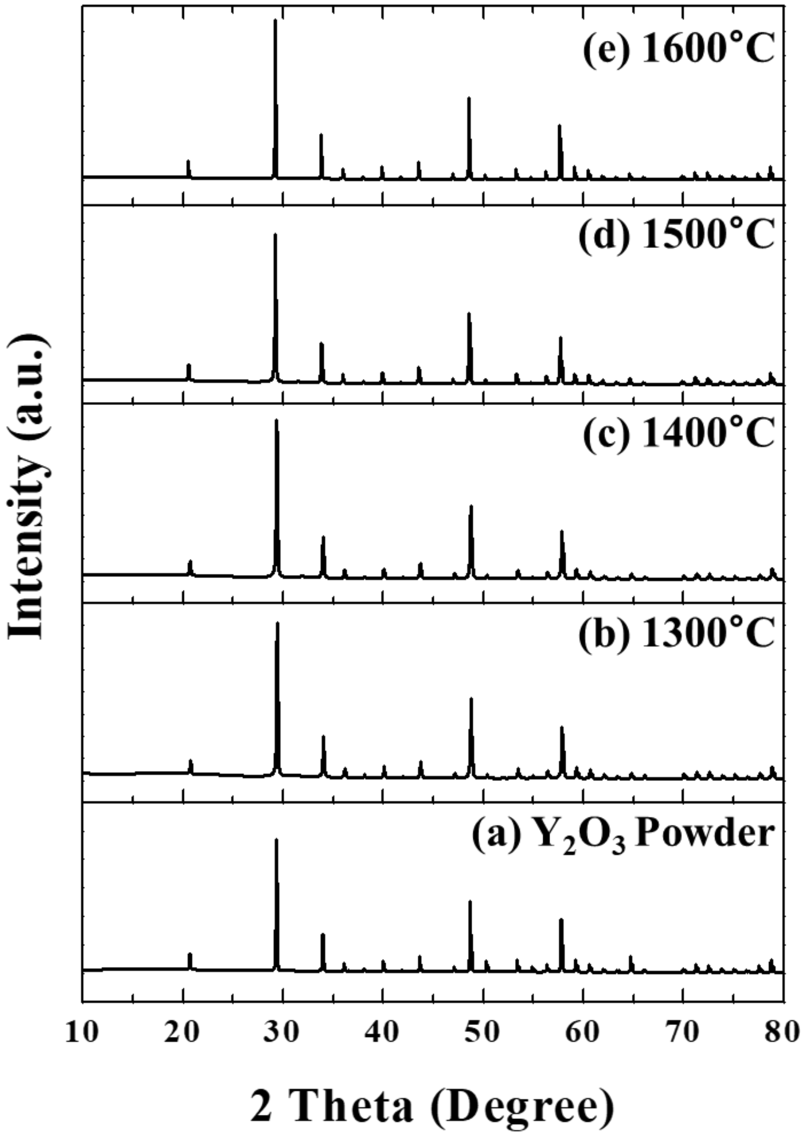

Fig. 27. XRD patterns of (a) Y_2O_3 powder and two-step SPSed Y_2O_3 ceramics depending on second-step temperatures of (b) 1300°C, (c) 1400°C, (d) 1500°C, and (e) 1600°C.

Through the observation of appearances and microstructures, because the second-step temperature of 1500°C and the first-step holding time of 60 min showed the clearest characters, these conditions might be considered the most optimized conditions for transparent Y_2O_3 ceramics. Among all specimens, the T1500-30, the two-step SPS at 1500°C; S1500, the single-step SPS; T1500-0, the SPS with a two-step pressure profile; the T1500-60, the two-step SPS with the first-holding time of 60 min was mainly discussed in regard to the fabrication of transparent Y_2O_3 ceramics using two-step SPS.

3.3.2. Shrinkage Behavior During SPS of Y_2O_3 Ceramics

In the SPS process, the temperature, punch displacement, and pressure were plotted against time to analyze the difference between the single-step profile and the two-step profile in Fig. 28. For the single-step, Y_2O_3 powder was heated to 800°C at 20°C/min with 80 MPa applied at the start and then heated to 1500°C at 5°C/min. In Fig. 28 (a), shrinkage is observed to begin at about 800°C and to stop at about 1250°C. Through the shrinkage curve of the single-step profile, the pressurization range of 800–1250°C was selected, and first-step sintering temperature could be set to 1250°C. Based on the results of the single-step profile, a two-step SPS profile was established, which is shown as a graph in Fig. 28 (b). Additional shrinkage which further improved the transmittance to theoretical transmittance, was observed at the holding stage of first-step sintering in Fig. 28 (b), at nearly 7000 s.

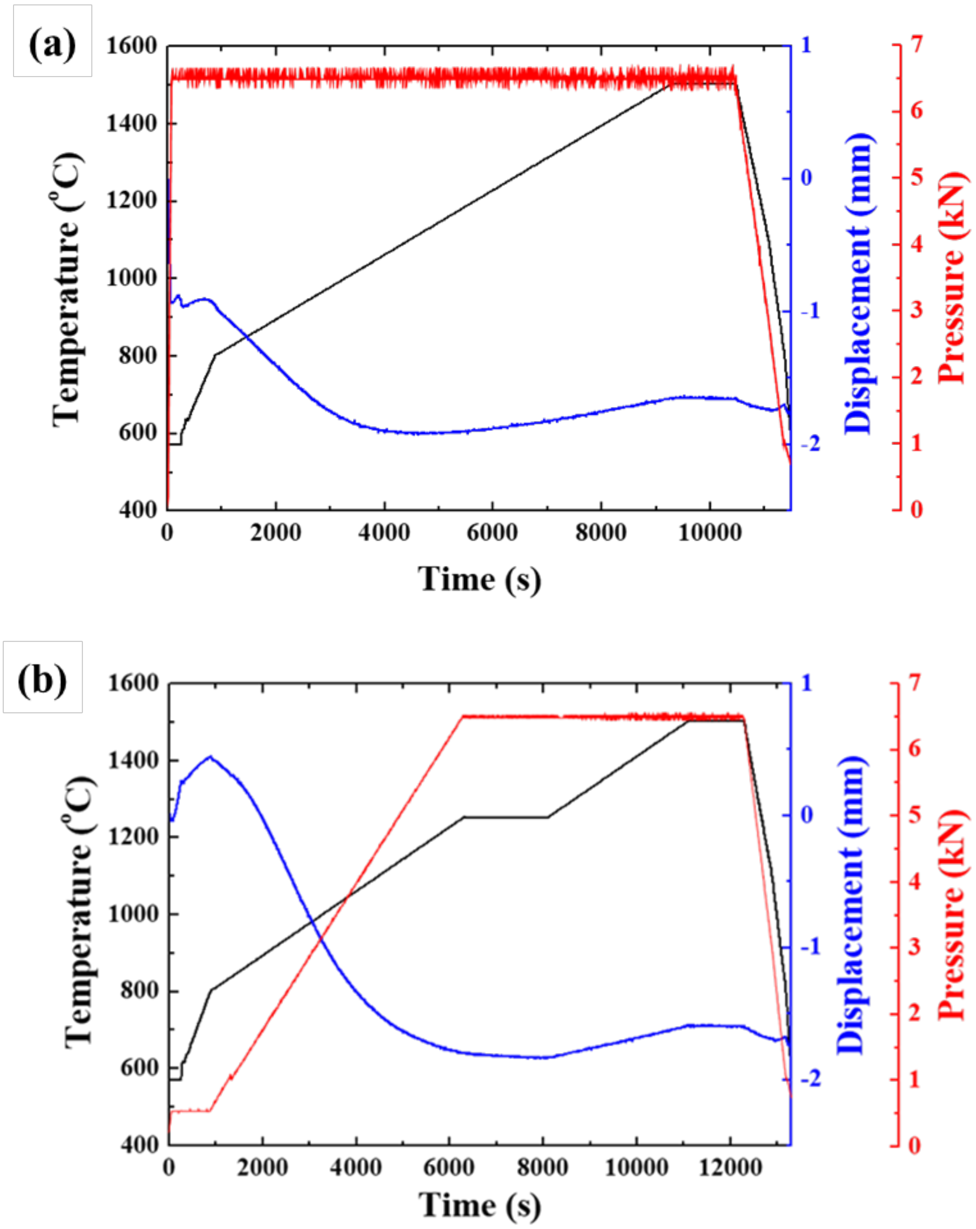

Fig. 28. SPS curve of Y_2O_3 ceramics sintered at 1500°C for 20 min with (a) single-step profile (S1500) and (b) two-step profile (T1500-30).

The shrinkage behavior of both profiles was compared by graph, with the x-axis as temperature in Fig. 29. In the case of the single-step profile, where pressure was applied from the beginning, nearly half of the total shrinkage occurs artificially in the early stage of the SPS process. However, since the two-step profile was heated with relatively low pressure (6.36 MPa), the shrinkage curve was observed to differ from that of the single-step profile. By applying maximum pressure (80 MPa) in the range (800–1250°C) where the shrinkage is actively occurring by thermal energy and atomic diffusion, the amount of shrinkage in the effective shrinkage range was significantly increased as compared to the single-step profile. In the case of loading the maximum pressure before heating (single-step profile), high stresses may concentrate in small regions where the powders contact each other and form strong bonds between each particle. In contrast, because of the enhanced matter diffusion and plastic deformation caused by high-temperature loading, the amount of shrinkage of the two-step profile was improved [13,14]. As shown in the optical image of all specimens (Fig. 25), the reason for better transparency with the two-step profile was investigated using shrinkage curves.

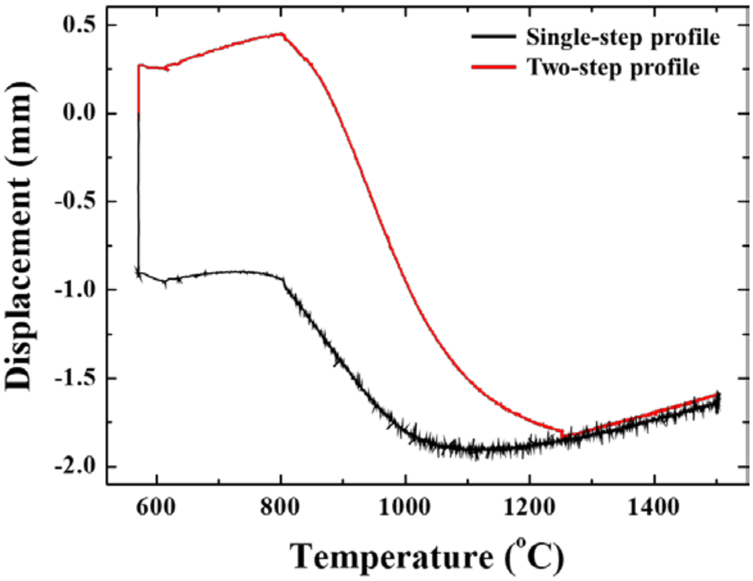

Fig. 29. Displacement curves of Y_2O_3 ceramics sintered at 1500°C for 20 min with single-step profile (S1500) and two-step profile (T1500-30).

3.3.3. Optical Properties

The infrared transmittance spectra of the SPSed Y_2O_3 ceramics were measured using FT-IR analysis and to be discussed are shown in Fig. 30. The thicknesses of the four specimens that were considered important are as follows. The specimen T1500-30 was 1.032 mm, T1500-

60 was 1.052 mm, T1500-120 was 1.043 mm, and S1500 was 1.036 mm. As a result of observing the specimens after annealing at 1000°C for 30 h, spectra with the same pattern were obtained for all the specimens. In all the specimens, strong absorption peaks corresponding to the C–O stretching vibration of the carbonate phase were detected in the range of 6.5–7 μm, and the intensity was different as shown in Fig. 30. These strong absorption peaks are due to the carbon unintentionally introduced by the carbon-rich environment of the SPS process [17,18]. The process that the C–O stretching vibration of carbonate phase unintentionally remains is as follows. Due to the SPS process conducted in a carbon-rich environment, carbon is unintentionally introduced into the sintered sample and reacts with oxygen in the Y_2O_3 lattice to form oxygen vacancy. In this process, the introduced carbon goes deep inside through the open pores as a CO gas phase, and it is encapsulated or precipitated as a solid phase in the closed pores. As a result, sintered samples with decolorized or darken optical appearance are observed [19–21]. For removing carbon contamination and oxygen vacancy that unintentionally occurred during the SPS process, an additional heat treatment (annealing) was performed at 1000°C for 10 h in an air atmosphere. Through the annealing process, trapped CO gas and precipitated carbon solid phase was transformed to CO_2 gas by reacting with external oxygen, and the optical appearance of the as-sintered sample was recovered as shown in Fig. 25. The transformed CO_2 gas reacts with metal oxide phase (Y_2O_3), so a carbonate phase is formed and detected in the FT-IR spectra as shown in Fig. 30 [19–21]. The specimen S1500 SPSed at 1500°C with the single-step profile had an IR transmittance that was significantly lower than that of other specimens. All other specimens had a maximum IR transmittance of over 80%, and the highest IR transmittance was obtained in T1500-60 (first-step holding time: 60 min). Through the FT-IR spectra, the holding time at the first-step sintering temperature was evaluated. Thus, the holding time at the first-step sintering of 60 min has slightly higher IR transmittance as compared to results as 30 and 120 min. To achieve close to theoretical

transmittance, first-step sintering needs to continue for 60 min. According to the FT-IR results, it can be concluded that the IR transmittance of Y_2O_3 SPSed with a two-step profile is superior to that with a single-step profile.

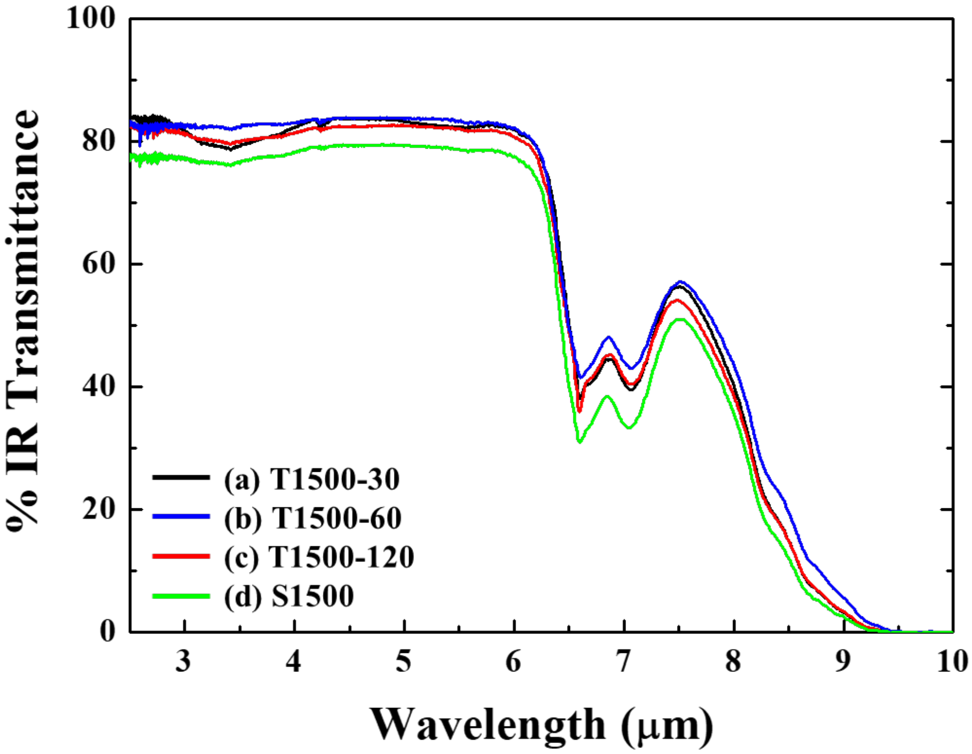

Fig. 30. FT-IR spectra of sintered Y_2O_3 ceramics after annealing at 1000°C for 30 h. (a) T1500-30, (b) T1500-60, (c) T1500-120, and (d) S1500.

Fig. 31 shows the in-line transmittance (ILT) as a function of the incident light wavelength measure in the range between 240 and 1600 nm. For comparison with each sample and theoretical transmittance, the ILT value in Fig. 31 was normalized to a thickness of 1 mm. Based on Beer-Lambert law, the intensity of light decreases exponentially with the depth x in the material via following Eq. (1),

$$I_x = I_{in} e^{-\mu x} \qquad (1)$$

where I_x is the intensity of light after traveling a depth of x inside the material, I_{in} is the initial intensity of light and μ is the linear attenuation coefficient. Transmittance T_x of an x mm thick sample is defined as following Eq. (2),

$$T_x = \frac{I_x}{I_{in}} = e^{-\mu x} \tag{2}$$

Consider T_0 is the transmittance of a 1 mm thick sample, Normalized transmittance to 1 mm thick sample was calculated via Eq. (3) [16].

$$T_0 = e^{-\mu} \rightarrow T_0 = T_x^{1/x} \tag{3}$$

Because this is the range in which the detector and the light source are changed, the noise was observed at around 900 nm. Prior to discussing the in-line transmittance of the SPSed Y_2O_3 ceramics, the theoretical transmittance can be calculated from the following equations, (4) and (5) [22].

$$ILT = (1 - Rs)\exp(-\gamma d) \tag{4}$$

$$Rs = \frac{2R}{1+R\prime}\ with\ R' = \left(\frac{n-1}{n+1}\right)^2 \tag{5}$$

Rs is the reflection losses at the surfaces at normal light incidence, and *d* is the thickness of the specimen. γ means the total scattering coefficient. The reflection losses, *Rs*, are determined by the refractive index, *n*, of polycrystalline Y_2O_3, which is a fundamental physical parameter of materials. The refractive index of Y_2O_3 is given by Eq. (6) [22,23].

$$n^2 - 1 = \frac{2.578\lambda^2}{\lambda^2 - 0.1387^2} + \frac{3.935\lambda^2}{\lambda^2 - 22.936^2} \tag{6}$$

The approximate transparency was confirmed in the optical image (Fig. 25), but a detailed comparison was possible through the normalized ILT graph as shown in Fig. 31. In this chapter, measuring the ILT of the four specimens, which are being discussed as necessary, the best ILT curve was obtained in T1500-60 sintered at the first-step temperature for 60 min. Following the same trend as the FT-IR result, the holding time of 60 min showed the highest ILT, as compared to 30 and 120 min. In addition, the two-step profile showed better results than the single-step profile. The specimen T1500-30 (about 180 nm), T1500-60 (less than 100 nm), and

T1500-120 (about 270 nm) sintered with a two-step profile had smaller pore sizes compared to the single-step profile (about 340 nm) as shown in the microstructure (Fig. 26). Since pore size is a crucial factor that negatively affects light scattering, specimen T1500-60 had the best ILT curve and, the S1500 had the worst ILT curve. In addition, T1500-120 had an ILT similar to that of the single-step profile at 800 nm or less. This is because excessive holding time caused excessive sintering in the first-step sintering, and not densification as well as coarsening occurred.

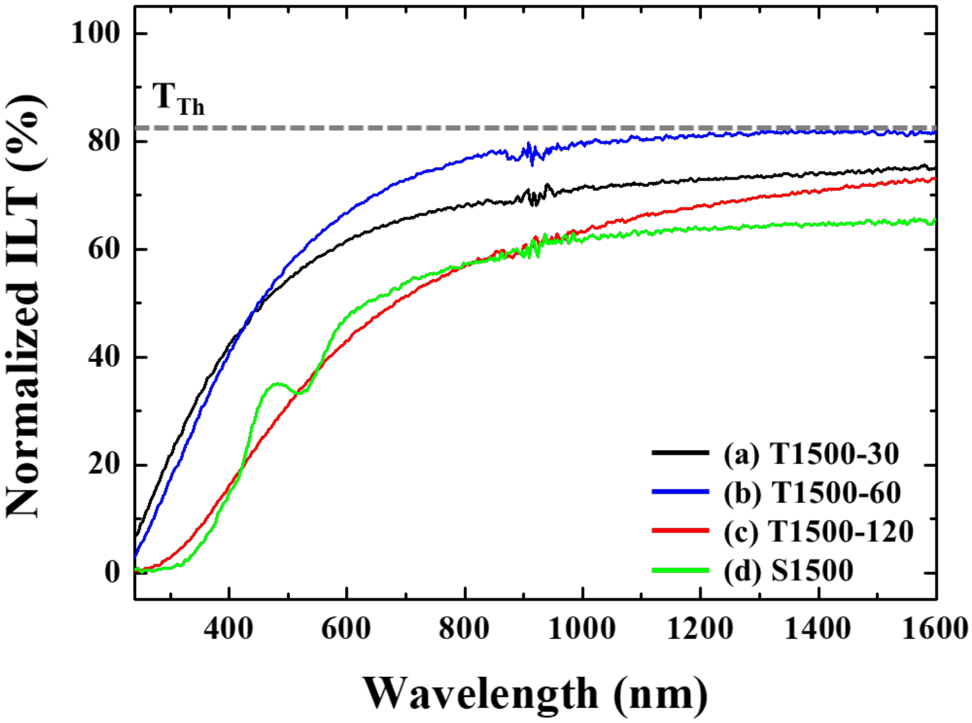

Fig. 31. In-line transmittance (ILT) of sintered Y_2O_3 ceramics after annealing at 1000°C for 30 h. The ILT value was normalized to a thickness of 1 mm. (a) T1500-30, (b) T1500-60, (c) T1500-120, and (d) S1500.

Next, as compared to the theoretical transmittance (81.6%) at 1100 nm, the ILT value of the T1500-60 was 80.6%, which was closest to the theoretical transmittance. The theoretical transmittance is a value determined by the structure and refractive index of each material.

However, polycrystalline ceramics are composed of many grains, and grain boundaries and pores exist. Since such grain boundaries or pores act as critical factors that decrease transmittance due to their defects, the ILT is inevitably lower than that of the theoretical transmittance. Therefore, the specimen T1500-60 with the smallest pore size and few pores observed showed the highest ILT value, but slightly lower than the theoretical transmittance. In addition to light scattering due to pores, which is very rarely observed, the C–O stretching vibration of carbonate phase detected in the FT-IR spectra (Fig. 30) causes light scattering even though it is very weak, so the ILT value close to theoretical transmittance could not be achieved. The single-step profile had an ILT value of 63.1%, which was significantly less than the theoretical transmittance. Although it was already a fully densified Y_2O_3 ceramic, an ILT close to the theoretical transmittance could be obtained through the two-step SPS profile. The significant improvement of transmittance can be achieved by reducing the residual pores, which may occur by enhanced matter diffusion and plastic deformation caused by high-temperature loading. The ILT of the two-step SPS profile could be improved with efficient pressurization (800–1250ºC), which can be verified from the shrinkage curve in Fig. 29. In addition, the two-step SPS profile was able to produce an ILT value of 80.6%, which is close to the theoretical transmittance, due to the suppression of excessive grain growth while achieving sufficient densification with a holding time of 60 min in first-step SPS.

3.4. Conclusions

In this chapter, the fabrication of transparent Y_2O_3 ceramics was successfully accomplished using SPS technology with a two-step pressure and heating profile. The optical image revealed that all the specimens were transparently sintered, and no secondary phase or phase transformation was observed in the XRD analysis. In addition, SEM analysis showed that densification occurred sufficiently in all the specimens, but the distribution of the ILT was significant. However, applying the two-step pressure and heating profile to the SPS technology significantly improved the ILT (63.1% (single-step profile) → 80.6% (two-step profile)). The two-step pressure profile, applying a pressure of 80 MPa in the range of 800–1250°C, improved the shrinkage behavior of the SPS process. In addition, the two-step heating profile of first-step sintering (@ 1250°C for 60 min) and second-step sintering (@ 1500°C for 20 min) not only achieved sufficient densification but also had the effect of suppressing excessive coarsening such as grain and pore growth.

References

[1] J. Dhanaraj, R. Jagannathan, T.R.N. Kutty, C.H. Lu, Photoluminescence characteristics of Y_2O_3:Eu^{3+} nanophosphors prepared using sol-gel thermolysis, J. Phys. Chem. B 105 (2001) 11098–11105.

[2] R.M. Sova, M.J. Linevsky, M.E. Thomas, F.F. Mark, High-temperature infrared properties of sapphire, AlON, fused silica, yttria, and spinel, Infrared Phys. Technol. 39 (1998) 251–261.

[3] H.M. Oh, Y.J. Park, H.N. Kim, et al., Effect of powder milling routes on the sinterability and optical properties of transparent Y_2O_3 ceramics, J. Eur. Ceram. Soc. 41 (2021) 775–780.

[4] G. Stanciu, L. Gheorghe, F. Voicu, et al., Highly transparent Yb:Y_2O_3 ceramic obtained by solid-state reaction and combined sintering procedures, Ceram. Int. 45 (2016) 3217–3222.

[5] S. Sattayaporn, G. Aka, P. Loiseau, et al., Optical spectroscopic properties, 0.946 and 1.074 μm laser performances of Nd^{3+}-doped Y_2O_3 transparent ceramics, J. All. Compd. 711 (2017) 446–454.

[6] R. Chaim, Densification mechanisms in spark plasma sintering of nanocrystalline ceramics, Mater. Sci. Eng. A 443 (2007) 25–32.

[7] H. Yoshida, K. Morita, B.N. Kim, et al., Reduction in sintering temperature for flash-sintering of yttria by nickel cation-doping, Acta Mater. 106 (2016) 344–352.

[8] B.N. Kim, K. Hiraga, K. Morita, et al., Dynamic grain growth during low-temperature spark plasma sintering of alumina, Scr. Mater. 80 (2014) 29–32.

[9] K. Morita, B.N. Kim, H. Yoshida, et al., Distribution of carbon contamination in $MgAl_2O_4$ spinel occurring during spark-plasma-sintering (SPS) processing: I–effect of heating rate and post-annealing, J. Eur. Ceram. Soc. 38 (2018) 2588–2595.

[10] B. Ratzker, A. Wagner, S. Kalabukhov, et al., Non-uniform microstructure evolution in transparent alumina during dwell stage of high-pressure spark plasma sintering, Acta Mater. 199 (2020) 469–479.

[11] J.H. Lee, B.N. Kim, B.K. Jang, Non-uniform sintering behavior during spark plasma sintering of Y_2O_3, Ceram. Int. 46 (2020) 4030–4034.

[12] A. Talimian, V. Pouchly, H.F. El-Maghraby, et al., Transparent magnesium aluminate spinel: Effect of critical temperature in two-stage spark plasma sintering, J. Eur. Ceram. Soc. 40 (2020) 2417–2425.

[13] H. Furuse, S. Nakasawa, H. Yoshida, et al., Transparent ultrafine Yb^{3+}:Y_2O_3 laser ceramics fabricated by spark plasma sintering, J. Am. Ceram. Soc. 101 (2018) 694–702.

[14] K. Morita, B.N. Kim, H. Yoshida, et al., Effect of loading schedule on densification of $MgAl_2O_4$ spinel during spark plasma sintering (SPS) processing, J. Eur. Ceram. Soc. 32 (2012) 2303–2309.

[15] M. Nanko, K.Q. Dang, Two-step pulsed electric current sintering of transparent Al_2O_3 ceramics, Adv. Appl. Ceram. 113 (2014) 80–84.

[16] H.H. Nguyen, M. Nanko, Densification and grain growth of large-sized polycrystalline Al_2O_3 during a two-step pulsed electric current sintering process, Mater. Trans. 59 (2018) 1610–1615.

[17] A. Gupta, N. Brahme, D.P. Bisen, Electroluminescence and photoluminescence of rare earth (Eu,Tb) doped Y_2O_3 nanophosphor, J. Lumin. 155 (2014) 112–118.

[18] S. Kumar, H. Tripathi, J. Sharma, U. Batra, Structural, morphological, and opto-electrical properties of $Y_{2-x}Yb_xO_3$ nanoparticles synthesized using co-precipitation method, Int. J. Appl. Ceram. Technol. 18 (2021) 12–23.

[19] S.M. Yong, D.H. Choi, K.S. Lee, et al., Study on carbon contamination and carboxylate group formation in Y_2O_3-MgO nanocomposites fabricated by spark plasma sintering, J.

Eur. Ceram. Soc. 40 (2020) 847–851.

[20] K. Morita, B.N. Kim, H. Yoshida, et al., Distribution of carbon contamination in oxide ceramics occurring during spark-plasma-sintering (SPS) processing: II - Effect of SPS and loading temperatures, J. Eur. Ceram. Soc. 38 (2018) 2596–2604.

[21] E.M. Kock, M. Kogler, T. Bielz, et al., In Situ FT-IR Spectroscopic Study of CO_2 and CO Adsorption on Y_2O_3, ZrO_2, and Yttria-Stabilized ZrO_2, J. Phys. Chem. C 117 (2013) 17666–17673.

[22] R. Apetz, M.P.B. Bruggen, Transparent alumina: A light-scattering model, J. Am. Ceram. Soc. 86 (2003) 480–486.

[23] M. Stuer, P. Bowen, M. Cantoni, et al., Nanopore characterization and optical modeling of transparent polycrystalline alumina, Adv. Funct. Mater. 22 (2012) 2303–2309.

Chapter 4. Fabrication of Ce^{3+}:$(Gd,Lu)_3Al_5O_{12}$ by SPS

4.1. Introduction

Recently, scintillation materials based on rare-earth aluminate garnets ($Ln_3Al_5O_{12}$, LnAG), represented by $Y_3Al_5O_{12}$ (YAG) and $Lu_3Al_5O_{12}$ (LuAG), have been studied. The advantages of the wide bandgaps, excellent chemical and thermal stabilities and high light transmittance in a wide spectral region are suitable characteristics for scintillation purposes [1–4]. The materials can be applied in white light-emitting diodes (white LEDs), environmental monitoring, geological surveying, medical imaging, security scanning, etc. [5,6]. In the phosphor field, YAG:Ce^{3+} is widely used to conversion blue to yellow light to produce white LEDs. In addition, transparent YAG:Ce^{3+} ceramics, which have extremely high luminescence efficiency and short decay times (tens of nanoseconds), might be used as advanced scintillators for medical x-ray detectors [7,8]. Scintillation materials usually need high theoretical density, but YAG has low theoretical density and not enough stopping power. Conventionally Gd_2O_3 and Y_2O_3 have a similar price, but Gd^{3+} has a higher atomic weight than Y^{3+}. For the above reasons, Ce^{3+}-doped GdAG materials have the potential to be ideal scintillator materials. In the Ce^{3+}-doped GdAG materials, Ce^{3+} doping causes instability of the garnet structure and a decreased decomposition temperature. In order to prevent decomposition, some researchers have proposed the doping of significantly smaller Lu^{3+} to reduce the average size of Ln^{3+} for structure stabilization [9,10]. This proposed doping of Lu^{3+} can lead to high theoretical density and retain the excellent luminescence properties of Ce^{3+}. As a result, it may yield new yellow phosphor and scintillation materials for optical and medical imaging applications.

In addition, to overcome the above problems related to lowered thermal decomposition temperature, lowering the sintering temperature by applying an advanced sintering technique is also one alternative. Among the many sintering techniques, spark plasma sintering (SPS) is the one that improves sinterability and can sinter transparent ceramics efficiently. During SPS, the electric field enhances densification by improving diffusion by suppressing grain growth and/or softening particle surfaces [11–14]. Direct heating of the mold and powder by the electric current enables rapid heating, full densification, and fine microstructures at low temperatures [15–19]. High densities and fine microstructures, which are advantages of SPS, improve ceramics' mechanical and optical properties. SPS could be used to fabricate fully dense transparent ceramics with fine microstructures at relatively low temperatures [20]. Recently, the reported paper attempted to sinter and characterize the LuAG ceramic samples via SPS. The LuAG samples were sufficiently sintered, and their transparency, morphology, and mechanical properties were studied [21]. However, despite the highly advanced sintering technology, SPS tends to show significant variations in characteristics such as density, microstructure, and transmittance of the sintered sample depending on the sintering conditions. For example, the formation of oxygen vacancies and microstructural defects within the sintered samples is enhanced in Al_2O_3 and $MgAl_2O_4$ ceramics depending on the SPS conditions (e.g. heating rate) [22,23]. Therefore, much research and caution are required in transparent ceramic materials when preparing for the sintering or determining the sintering conditions.

The main purpose of this study is the fabrication of Ce^{3+}:$(Gd,Lu)_3Al_5O_{12}$ ceramics at a relatively low temperature of 1300°C with fully densified microstructure by the SPS process. In addition, the correlation between the optical properties and carbon contamination according to the annealing process was investigated to restore the optical properties deteriorated due to carbon contamination of a negative effect in the SPS process.

4.2. Experimental Procedure

Ln_2O_3 (Ln = Gd, and Lu, 99.99% pure, Huizhou Ruier Rare Chemical Hi-Tech Co. Ltd., Huizhou, China), $Ce(NO_3)_3 \cdot 6H_2O$ (99.99% pure, Huizhou Ruier Rare Chemical Hi-Tech Co. Ltd.) and alum ($NH_4Al(SO_4)_2 \cdot 12H_2O$, > 99% pure, Zhenxin Chemical Reagent Factory, Shanghai, China) were used in this experiment as rare-earth and aluminum sources. The oxide materials were dissolved in a proper amount of nitric acid for the preparation of $Ln(NO_3)_3$ stock solution. A carbonate precursor was then precipitated by dropwise adding a mixed solution containing stoichiometric amounts of the nitrates and alum into a solution of ammonium bicarbonate. After collection and drying, the precursor was calcined at 1100°C for 4 h in air, during which carbonate was converted into oxide through thermal decomposition. The final heat-treatment was conducted at 1000°C for 4 h in Ar/H_2 (5 vol% of H_2) to suppress Ce^{3+} oxidation [9,10]. As a result, it was confirmed that the content of Ce^{3+} (82.3%) and Ce^{4+} (17.7%) were detected in the $[(Gd_{0.6}Lu_{0.4})_{0.99}Ce_{0.01}]_3Al_5O_{12}$ powder by XPS analysis [24,25].

The synthesized $(Gd,Lu)_3Al_5O_{12}:Ce^{3+}$ powder was consolidated with an SPS machine (LABOX-315, Sinter Land, Japan) to obtain dense and translucent samples. The powder was sintered in vacuum using a graphite mold with a 10 mm inner diameter. The sintering temperature (1300°C) and pressure (80 MPa) were fixed, and holding times were varied (0, 5, 20, 60, and 300 min). Up to 1000°C, the mold was heated at a rate of 50°C/min, and then at 10°C/min. The temperature was measured using a pyrometer in the non-through hole of the mold. The mold was covered with carbon felt to reduce heat dissipation. Further heat treatment (annealing) was conducted to analyze the luminescence characteristics according to the microstructure change. The annealing temperature was 1300°C, and the holding time was 2 h in air.

The sintered and annealed samples were mirror polished and thermally etched at 1100°C for 2 h in air. The polished surfaces and fracture surfaces were observed using a scanning electron microscope (SEM, SU-8000, Hitachi). The porosity was obtained by measuring the porous area in SEM images. The grain size was calculated by measuring the average cross-section area per grain and by assuming spherical grains. The grain size is an apparent one in cross section, so that it was multiplied by 1.225 to determine the true grain size [25]. For measurement of the total transmittance, both surfaces of the sintered sample were carefully mirror polished with diamond paste and finished with a 1 μm paste. The total transmittance measurements were conducted using a double-beam spectrophotometer (SolidSpec-3700DUV, Shimazu Co. Ltd., Japan) equipped with an integrating sphere. The photoluminescence (PL) spectra (wavelength accuracy: ± 1 nm) of the phosphors were collected at room temperature using an FP-6500 fluorospectrophotometer (JASCO, Japan) equipped with a 60 mm diameter integrating sphere (Model ISF-513, JASCO) and a 150 W Xe lamp as the excitation source. Monochromatization of the excitation and emission lights was achieved with a Rowland concave grating (1800 grooves mm^{-1}). Optical measurements were conducted under identical conditions for all of the samples, with slit widths of 5 nm for both the excitation and emission sides. Spectral responses of the equipment were corrected in the range of 220–850 nm with a Rhodamine-B solution (5.5 g in ethylene glycol) and a standard light source unit (ECS-333, JASCO) as references.

4.3. Results and Discussion

4.3.1. Compositional and Microstructural Analysis

Fig. 32 shows XRD patterns of the $[(Gd_{0.6}Lu_{0.4})_{0.99}Ce_{0.01}]_3Al_5O_{12}$ ceramics, which were sintered at 1300°C for 0, 5, 20, 60, and 300 min before and after annealing at 1300°C for 2 h. The diffraction peaks were well-indexed with the cubic structure of the GdAG garnet (JCPDS No. 1-73-1371) and in each case the sharp diffractions imply high crystallinity of the sintered and annealed samples [9]. It was reported by Li et al. that, under 1 at% of Ce^{3+} doping, crystallization of GdAG was promoted by Lu^{3+} incorporation [9]. Regardless of the holding time and annealing effects, no obvious peak shifting, and phase transformation were observed before/after annealing as compared to the JCPDS card. In addition, the sintering temperature of 1300ºC provided enough energy for crystallization. This result could be proved by that of Li et al. [9], who reported that, in the case of $(Gd,Lu)Al_5O_{12}$ garnet powder synthesis, the phase transformation to the garnet phase is completed at 1300°C. Therefore, after SPS at 1300°C, it was concluded that the sintered sample was sufficiently crystallized because it consisted of pure garnet phase. However, it was confirmed that the grain size of annealed samples slightly increased and the amount of oxygen vacancy decreased because the peaks became sharper as a whole, and noise of 20° or less was reduced [26].

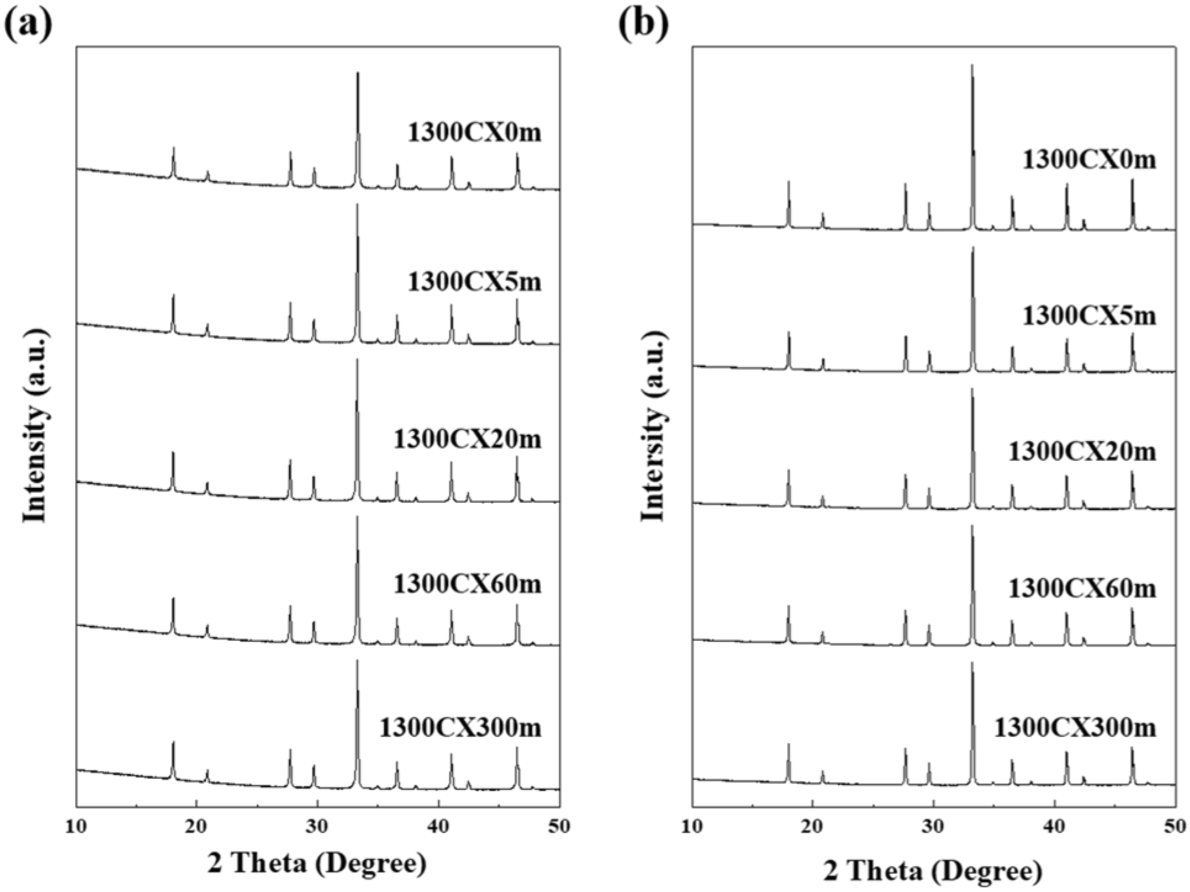

Fig. 32. XRD patterns of (a) as-sintered samples at 1300°C for 0, 5, 20, 60, and 300 min and (b) annealed samples at 1300°C for 2 h in air atmosphere.

The SEM images of as-sintered samples at 1300°C for various holding times (0, 5, 20, 60, and 300 min) are shown in Fig. 33. Significant pores were not observed in the SEM images in Fig. 33 and 34, but a denser microstructure was obtained through the annealing process (Fig. 34). Regardless of annealing, the sintered samples were sufficiently densified.

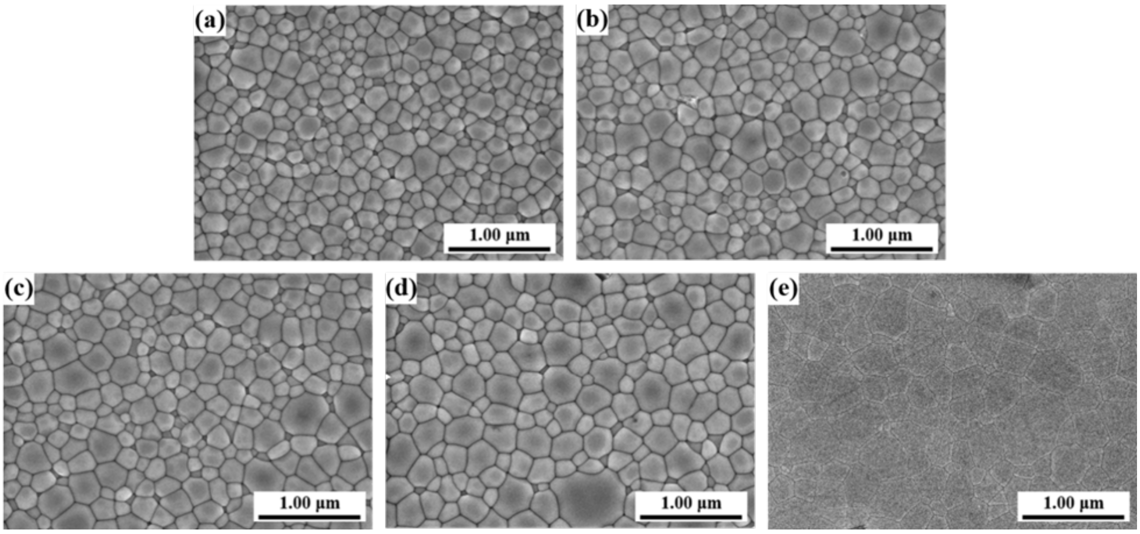

Fig. 33. SEM images of as-sintered samples at 1300°C for (a) 0 min, (b) 5 min, (c) 20 min, (d) 60 min, and (e) 300 min under the 80 MPa.

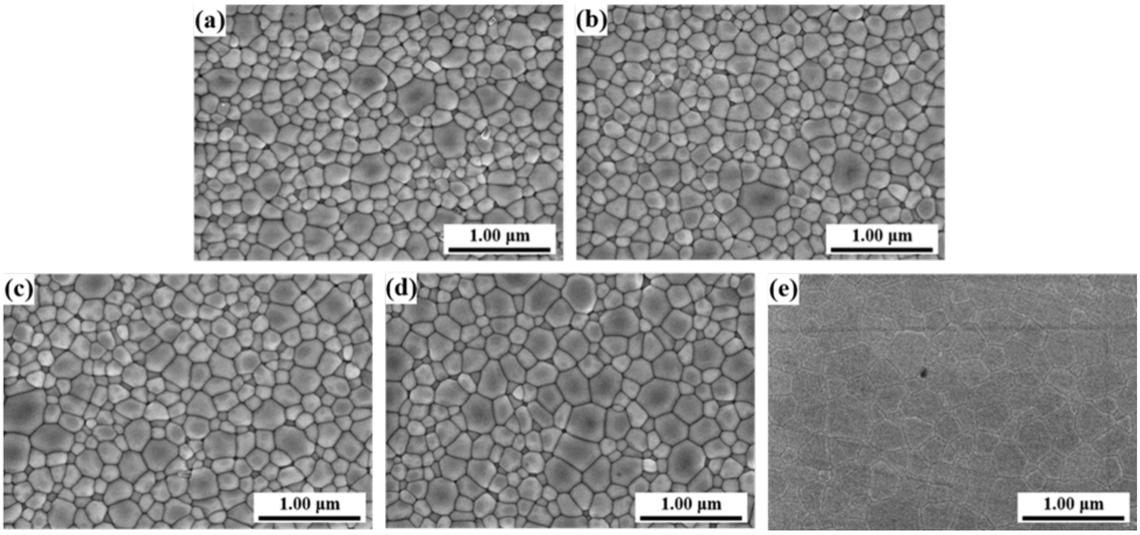

Fig. 34. SEM images of annealed samples at 1300°C for (a) 0 min, (b) 5 min, (c) 20 min, (d) 60 min, and (e) 300 min under the 80 MPa.

As the holding time increased, the grain size increased as expected and it can be seen that a lot of grain growth occurred at the early stage of holding during the sintering in Fig. 35 (a). Porosity also tended to decrease rapidly initially, and after a holding time of 20 min, only a small decrease in porosity was observed in Fig. 35 (b). In this study, SPSed samples showed rapid grain growth and porosity reduction (densification) at the initial stage of sintering. Annealing was conducted to analyze the effect of the microstructure change and correlations with the microstructure, transmittance, and luminescence properties depending on the heat treatment. Through the Fig. 35, after annealing, the slightly occurred grain growth and densification were observed despite annealing at the same temperature as the sintering temperature. There were no significant differences in microstructure before and after annealing. In this chapter, there are two main reasons for this phenomenon. The first reason is that the energy for atomic diffusion was not enough during the annealing process. Although the temperature was the same in sintering and annealing process, the energy for atomic diffusion of the SPS process is higher due to the SPS technology in which an electric field and mechanical pressure are simultaneously applied. For this reason, it was judged that the microstructure of the sintered sample sufficiently densified by the SPS technology could not be changed. The second reason is that energy was consumed to remove carbon contamination and oxygen vacancies. The primary purpose of the annealing process is to minimize the changes in microstructure and eliminate carbon contamination and oxygen vacancies. Therefore, the thermal energy of the annealing process is consumed in the lattice with oxygen vacancies, and consequently, the oxygen vacancies are removed through lattice relaxation [26].

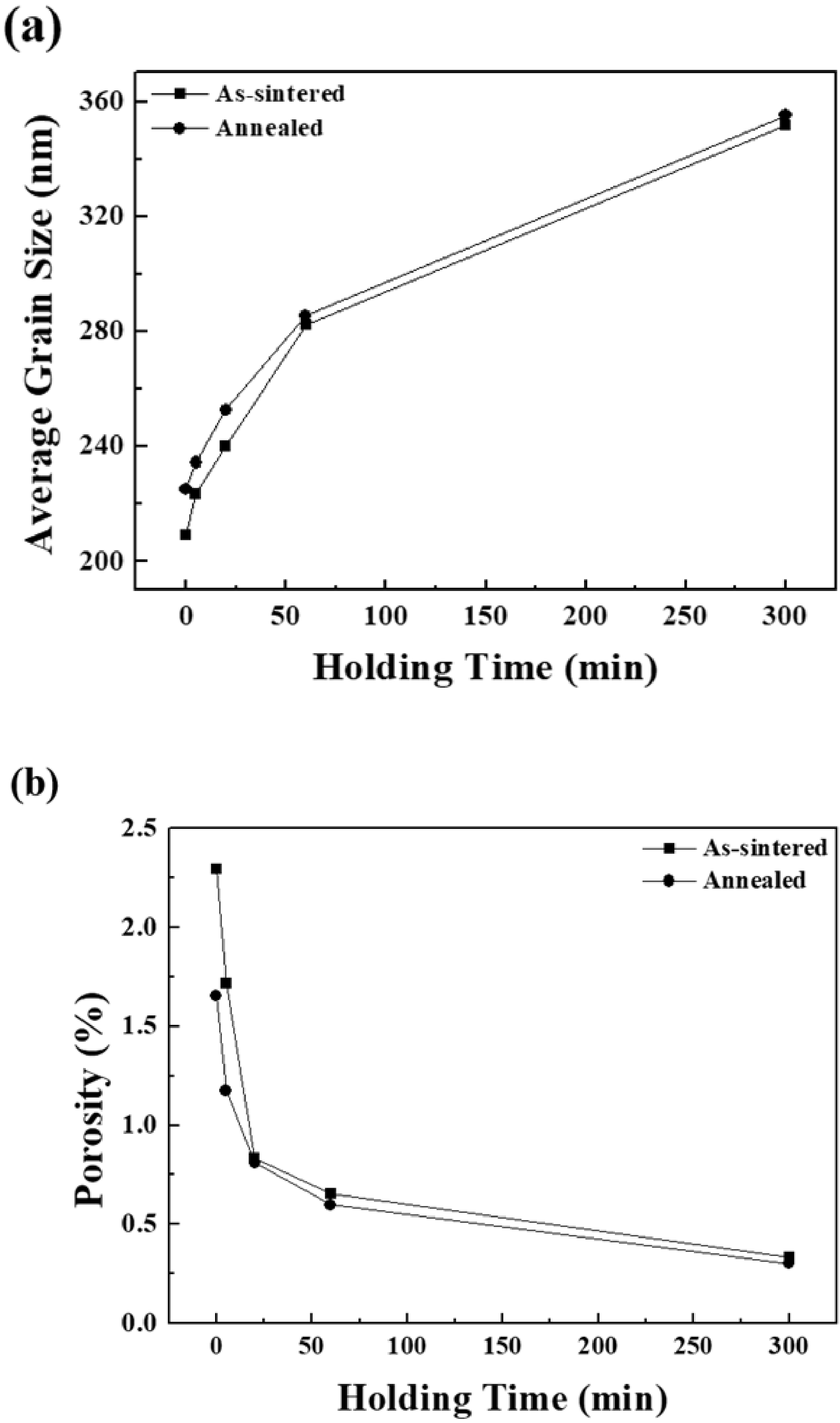

Fig. 35. (a) Average grain size and (b) porosity graph of sintered samples before and after annealing at 1300°C for 2 h in air atmosphere.

4.3.2. Optical Properties

The total transmittance results of as-sintered and annealed samples were summarized and presented as a graph in Fig. 36. In the transmittance results of the sintered sample, the transmittance tended to decrease with increasing holding time, and the distribution of the results was wide. After annealing, however, the distribution became significantly narrower. In general, the smaller porosity and larger grain size increased transmittance, but the results of this study were different. In the case of the SPSed oxides, it is known that carbon contamination and oxygen vacancies are produced during the sintering process under the reduction atmosphere [22,23]. Since most of the SPS equipment consists of carbon, such as a graphite die and punch, etc., carbon contamination is unavoidable. The proposed mechanism is that the carbon monoxide evaporation is enhanced due to the applied pulse current, which then enters the sintered sample through the open pore channels. The evaporated carbon is encapsulated in the closed pores during the sintering process and remains in the sintered sample [27]. Additionally, in the case of oxides, a lot of oxygen vacancies were produced due to the carbon-rich environment of SPS under the reduction atmosphere. The oxygen presented in the oxide materials, and carbon introduced in sintering process could react with each other due to the sufficiently high atomic diffusion energy and carbon-rich atmosphere. At this time, the CO or CO_2 gas is produced and evaporated from the sintered sample, and oxygen vacancies were produced consequently [28]. As the sintering continues, the carbon contamination and oxygen vacancies remaining in the sintered sample seem to increase. The carbon contamination and oxygen vacancies in the SPS process directly affects the appearance and discoloration of the sintered sample. When carbon contamination occurs, carbon materials other than diamond have a black color, so considerable light absorption occurs. Light absorption due to carbon contamination leads to darkening and discoloration of sintered sample. In addition, oxygen vacancies are belonging to defect and are a factor of light absorption in SPSed transparent ceramics. The decrease in transmittance by light scattering has some effect on the darkening of the sintered sample. As carbon contamination and oxygen vacancies occur, the darkening and discoloration of sintered sample were finally induced. Although light passes through the sintered sample, the transmittance is reduced by the dark sintered sample. Another factor for increased transmittance is the area of grain boundary. The grain boundary is created because the atomic arrangement direction of each grain is different, and it belongs to defects. When light passes through, the arrangement direction of each grain is different, so the refraction and scattering of light occur theoretically at grain boundaries [29]. In this chapter, more grain size increases occurred in the specimens with longer holding times, and the area of grain boundaries was further reduced accordingly. Therefore, although the effect of grain boundaries on light scattering is small, it was concluded that the effect of grain boundaries helped slightly to increase the transmittance. As a summary, although the porosity decreased and the grain size increased, the transmittance tended to decrease significantly with a longer holding time due to the increase in carbon contamination and oxygen vacancies. Because the annealing process could remove the carbon contamination and oxygen vacancies, the distribution of the transmittance results was significantly reduced, and some specimens showed improved transmittance.

Notably, it was confirmed that significant light absorption occurred around 340 nm and 420–500 nm, as shown in Fig. 36. When Ce^{3+} ions are doped, they absorb light having energy around 340 nm and 420–500 nm and then emits light. The strong absorption bands around 340 nm and 420–500 nm can be attributed to $4f \rightarrow 5d_2$ and $4f \rightarrow 5d_1$ transitions of Ce^{3+}, respectively [30]. Therefore, through the low transmittance around 340 nm and 420–500 nm on the total transmittance graph, it can be observed that Ce^{3+} ions were added.

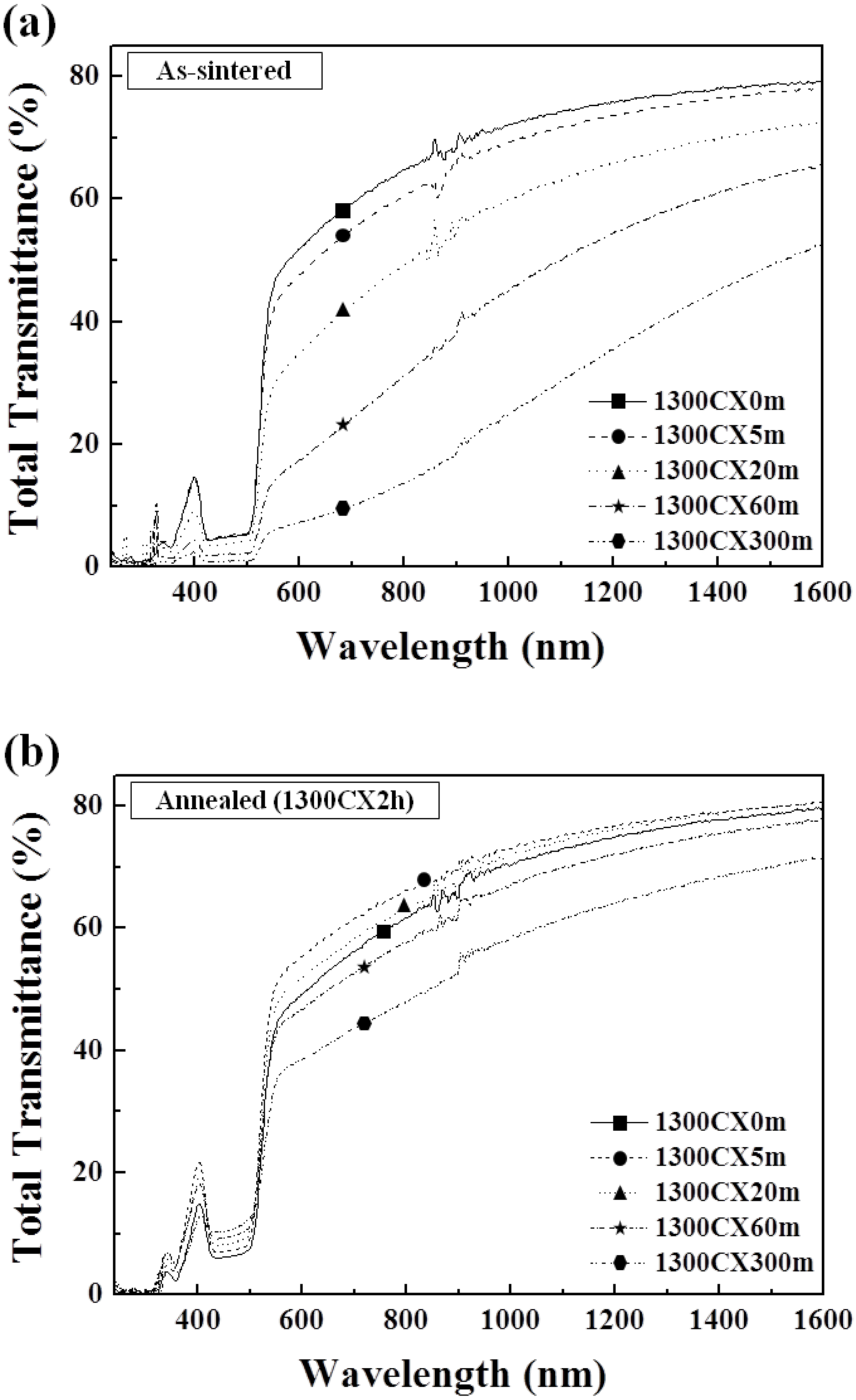

Fig. 36. Total transmittance results of the sintered samples (a) before and (b) after annealing at 1300°C for 2 h in air atmosphere.

4.3.3. PL Characteristics

The PL excitation and PL emission measurements of as-sintered and annealed samples were conducted using a spectrofluorometer (FP-6500, JASCO, Japan), and the results are summarized in Figs. 37 and 38. The excitation bands centered on 275, 342, 453, and 506 nm are identified on the PL excitation spectra in Fig. 37, with the latter being significantly stronger. The weak peak observed around 275 nm is due to the typical $^8S_{7/2} \rightarrow {}^6I_J$ intra f-f transition of Gd^{3+} [9,31]. The three bands (around 342, 453, and 506 nm) are the transition from the ground state ($^2F_{5/2}$) of Ce^{3+} $4f^1$ electron to the 5*d* excited state of T_{2g} composed of three individual bands and the transition from the ground state to the 5*d* excited state of E_{2g} composed of two individual bands [32]. This PL excitation process was presented in Fig. 39 as schematic diagrams. This chapter focused more on how annealing after the SPS process affects the luminescent behavior rather than a detailed description of the luminescence characteristics. After annealing, the positions of the three bands were identical, and the intensity of each spectrum increased significantly. The reason is that the grain size was increased, the porosity was decreased, and the estimated generation of carbon contamination and oxygen vacancies during the SPS process were efficiently removed through annealing. Because the amount of grain boundaries and pores belonging to defects, was reduced, the luminescence properties were improved. In addition, carbon contamination and oxygen vacancies as one of the defects mainly induce light absorption. So, in the photoluminescence test, the emitted light can be absorbed by carbon contamination and oxygen vacancies, respectively. As a result, the propagation of emitted light to outside was interrupted. For this reason, carbon contamination and oxygen vacancies interrupt the propagation of emitted light, and their removal through annealing thus improved the luminescence properties of the sintered sample. Specifically, as shown in Fig. 37, the increase in PL excitation intensity tends to expand. For example, the sintered sample kept at a sintering temperature for 300 min had the lowest PL excitation intensity before annealing but the highest PL excitation intensity after annealing. In general, in sintered samples of the same composition, the larger the grain size and the lower the porosity, the higher the PL excitation intensity. Sintered samples with larger grain sizes and lower porosity have less grain boundary area, which means that the number of defects in the sintered sample is small because grain boundaries are one type of defects. Since the number of defects were reduced, it was thus possible to improve the luminescence properties (PL excitation characteristics). In addition, more PL excitation intensity improvements by annealing occurred in the sintered sample kept for 20, 60, and 300 min with effectively removed carbon contamination and oxygen vacancies. Through the above results, as the holding time increased, the large grain size and low porosity also affected the PL excitation characteristics. However, it was determined that carbon contamination and oxygen vacancies more effectively affected the PL excitation characteristics. The more carbon contamination and oxygen vacancies that were produced, the darker the sintered sample became and the more drastic was the decrease in transmittance. Therefore, when using SPS as a sintering technique, controlling carbon contamination and oxygen vacancies rather than grain size and porosity is considered to be important for producing effective luminescent materials.

The transition from the ground state ($^2F_{5/2}$) of Ce^{3+} to the E_{2g} state has a higher emission intensity, of which the 453 nm band has a greater effect. Therefore, the PL emission characteristics were analyzed in the situation of being excited at 453 nm. It was widely emitted from about 500 nm to 750 nm and had the highest value around 571 nm. The schematic diagram of PL emission process of Ce^{3+} showed in Fig. 39. The PL emission peak was emission of Ce^{3+} arising from the electron transitions from the $4f^0 5d^1$ excited state to the two ground states of the $4f^1 5d^0$ orbital ($^2F_{5/2}$) for short wavelength of 571 nm caused by spin-orbit coupling. The emission centers of transparent Ce-doped YAG ceramics are generally reported to be located at 550 nm [33], while the obvious red-shift peak location observed for the Ce-doped

$(Gd,Lu)_3Al_5O_{12}$ sample was primarily owing to the host lattice effect on the crystal field splitting of Ce^{3+} $4f$–$5d$ energy levels [9]. The electronegativities of Gd, Y, Lu, and Ce are 1.21, 1.22, 1.27, and 1.12, respectively. Therefore, ternary Gd/Lu/Ce lanthanide cations have a higher average electronegativity (1.23) than binary Y/Ce systems (1.22). The increasing electronegativity of Ln^{3+} makes the centroid of the Ce^{3+} move to a higher energy level, ultimately leading to a longer emission wavelength. The sintered samples with a longer holding time tended to have a lower PL emission intensity. As with the PL excitation characteristic behavior, the PL emission intensity of whole sintered samples increased significantly after annealing. This is because annealing had effectively eliminated the more critical role of carbon contamination and oxygen vacancies, the same reason the PL excitation characteristics were improved. From the PL emission characteristic graph (Fig. 38), the full width at half maximum (FWHM) can be calculated and compared. In general, it is known that the lower the FWHM value in the luminescent materials, the higher the crystallinity and the more distinct the light that is emitted. In this study, the FWHM value of the sintered sample was about 107.5 nm and had an FWHM value of about 105 nm after annealing. After annealing, the FWHM value decreased slightly. Based on the decrease in the FWHM value after annealing, it was concluded that the crystallinity of the sintered luminescent samples had increased and had more outstanding PL emission characteristics. Because the defects (carbon contamination and oxygen vacancies) have been removed by annealing effectively, the quality of sintered sample was improved. Furthermore, it was concluded that the crystallinity was slightly increased because the grain size also increased, and the grain boundary, and oxygen vacancy, which belong to defects, were reduced. The increased crystallinity was also confirmed in the XRD patterns.

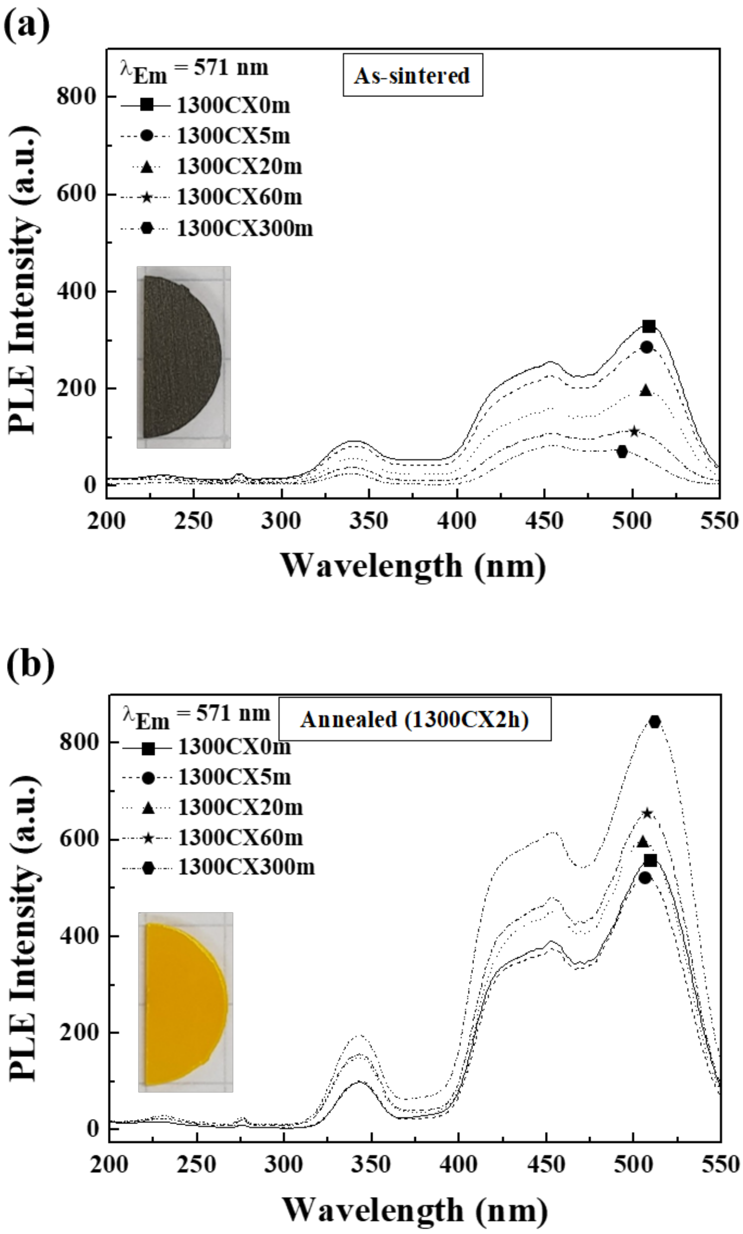

Fig. 37. PL excitation spectra of the sintered samples (a) before and (b) after annealing at 1300°C for 2 h in air atmosphere. The emission wavelength (λ_{Em}) of 571 nm was used for measurements. The inserted images are optical images of sintered sample at 1300°C for 300 min (a) before and (b) after annealing.

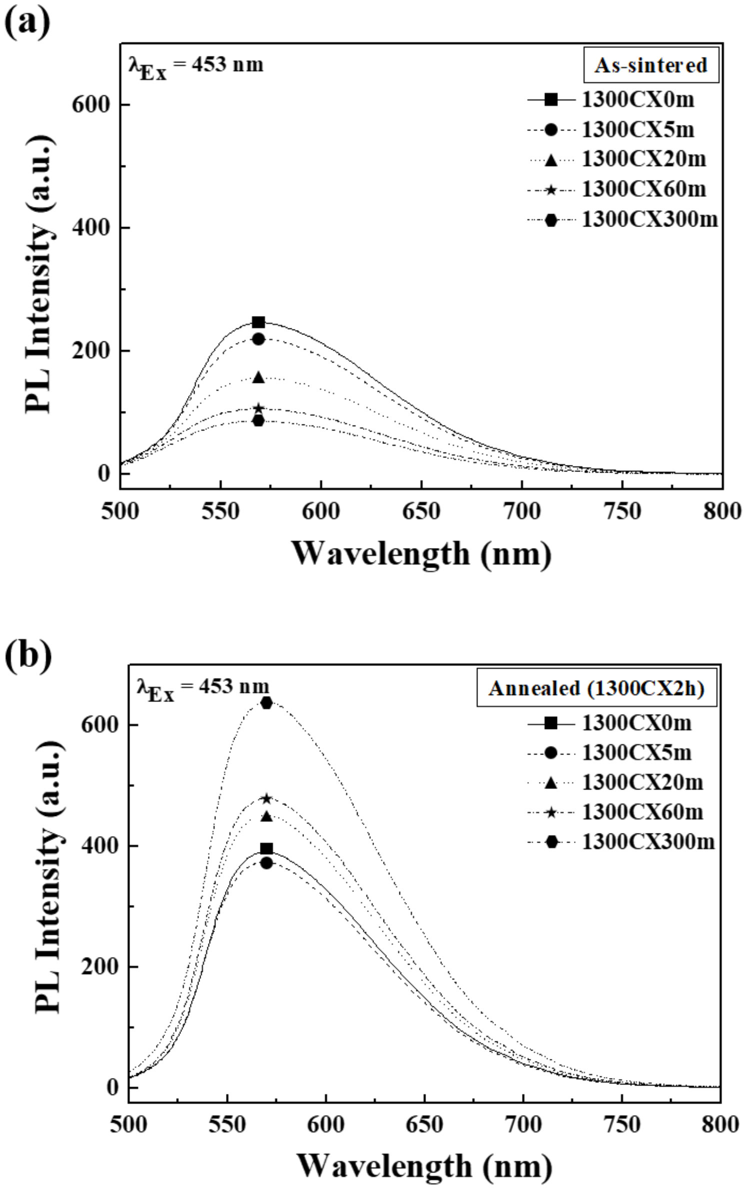

Fig. 38. PL emission spectra of the sintered samples (a) before and (b) after annealing at 1300°C for 2 h in air atmosphere. The excitation wavelength (λ_{Ex}) of 453 nm was used for measurements.

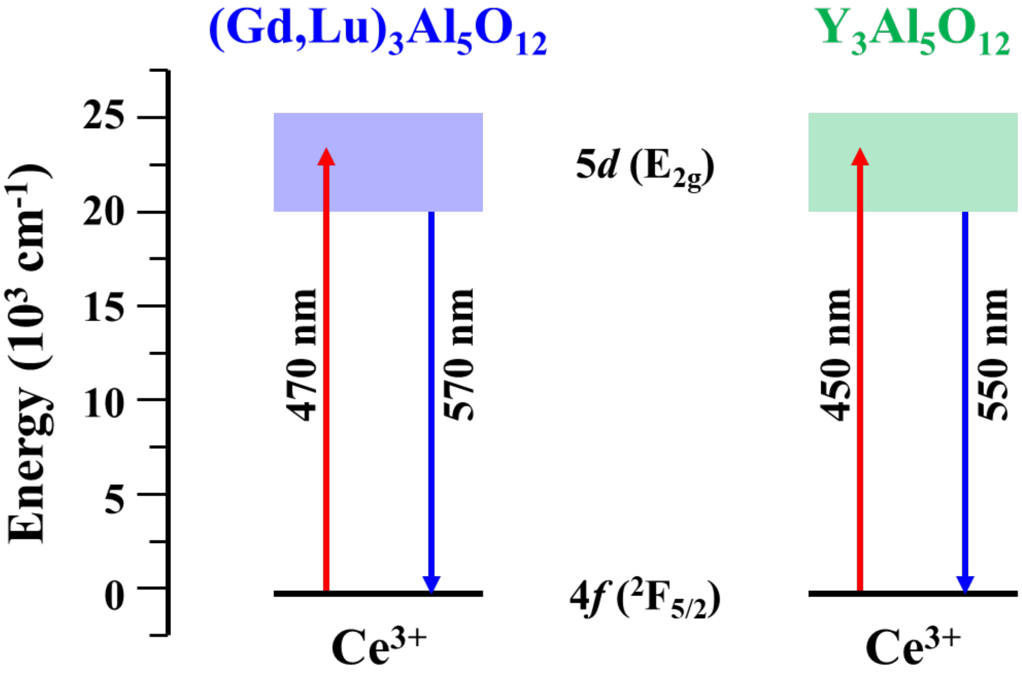

Fig. 39. The schematic energy levels and wavelengths of Ce^{3+} dopant in (Gd,Lu)$_3$Al$_5$O$_{12}$ and Y$_3$Al$_5$O$_{12}$ ceramics.

4.4. Conclusions

Among the SPSed luminescent materials, Ce^{3+}-activated $(Gd,Lu)_3Al_5O_{12}$ garnet powder was sintered at different holding times (0, 5, 20, 60, and 300 min) at 1300°C under 80 MPa to analyze the effect of annealing on the microstructure and luminescence characteristics. Due to the carbon contamination and oxygen vacancies induced during the SPS process, the transmittance of the sintered samples tended to decrease with holding time. After annealing, the reduced transmittance was mostly recovered. In the PL excitation characteristic results after annealing, the positions of three bands were identical, and the intensity of each spectrum increased significantly. This is because carbon contamination and oxygen vacancies induced during the SPS process had a more significant effect than grain size and porosity and were removed effectively by annealing. As a result, more PL excitation intensity improvements occurred in the sintered samples held for 20, 60, and 300 min, while carbon contamination and oxygen vacancies were effectively removed. The PL emission characteristic behavior was the same as that of the PL excitation, and increased crystallinity and improved PL emission intensities were obtained based on the decreased FWHM value after the annealing process.

References

[1] D.Y. Chen, Y. Liu, E. Jordan, Sol-Gel Combustion Synthesis and Photoluminescent Properties of YAG:Eu Phosphors, Sci. Adv. Mater. 2 (2010) 493–496.

[2] K. Guo, M.L. Huang, H.H. Chen, et al., Comparative study on photoluminescence of amorphous and nano-crystalline YAG:Tb phosphors prepared by a combustion method, J. Non Cryst. Sol. 358 (2012) 88–92.

[3] W.H. Chao, R.J. Wu, T.B. Wu, Structural and luminescent properties of YAG:Ce thin film phosphor, J. Alloy Comp. 506 (2010) 98–102.

[4] V. Schiopu, M. Alina, A. Dinescu, et al., Ce, Gd Co-doped YAG Nanopowder for White Light Emitting Device, J. NanoSci. Nanotech. 12 (2012) 8836–8840.

[5] A. Bhaskar, H.Y. Chang, T.H. Chang, S.Y. Cheng, Microwave annealing of YAG:Ce nanophosphors, Mater. Lett. 78 (2012) 124–126.

[6] K. Bando, K. Sakano, Y. Noguchi, Y. Shimizu, Development of High-bright and Pure-white LED Lamps, J. Light Vis. Environ. 22 (1988) 2–5.

[7] Y. Zorenko, T. Zorenko, V.V. Gorbenko, et al., Peculiarities of luminescent and scintillation properties of YAG:Ce phosphor prepared in different crystalline forms, Opt. Mater. 34 (2012) 1314–1319.

[8] E. Mihokova, M. Nikil, J.A. Mares, et al., Luminescence and scintillation properties of YAG:Ce single crystal and optical ceramics, J. Lumine. 126 (2007) 77–80.

[9] J.K. Li, J.G. Li, S.H. Liu, et al., The development of Ce^{3+}-activated $(Gd,Lu)_3Al_5O_{12}$ garnet solid solutions as efficient yellow-emitting phosphors, Sci. Technol. Adv. Mater. 14 (2013) 1–9.

[10] J.K. Li, J.G. Li, X.D. Li, X.D. Sun, Photoluminescence properties of phosphors based on Lu^{3+}-stabilized $Gd_3Al_5O_{12}$:Tb^{3+}/Ce^{3+} garnet solid solutions, Opt. Mater. 62 (2016) 328–334.

[11] S. Ghosh, A. H. Chokshi, P. Lee, R. Raj, A huge effect of weak dc electrical fields on grain growth in zirconia, J. Am. Ceram. Soc. 92 (2009) 1856–1859.

[12] D. Yang, R. Raj, H. Conrad, Enhanced sintering rate of zirconia (3Y-TZP) through the effect of a weak dc electric field on grain growth, J. Am. Ceram. Soc. 93 (2010) 2935–2937.

[13] S. Nekahi, F.S. Moghanlou, M. Vajdi, et al., Microstructural, thermal and mechanical characterization of TiB_2-SiC composites doped with short carbon fibers, Int. J. Refract. Hard Met. 82 (2019) 129–135.

[14] R. Chaim, Densification mechanisms in spark plasma sintering of nanocrystalline ceramics, Mater. Sci. Eng. A 443 (2007) 25–32.

[15] H. Yoshida, K. Morita, B.N. Kim, et al., Low-temperature spark plasma sintering of yttria ceramics with ultrafine grain size, J. Am. Ceram. Soc. 94 (2011) 3301–3307.

[16] R. Chaim, M. Levin, A. Shlayer, C. Estournes, Sintering and densification of nanocrystalline ceramic oxide powders: A review, Adv. Appl. Ceram. 107 (2008) 159–169.

[17] H. Zhang, B.N. Kim, K. Morita, et al., Fabrication of transparent yttria by high-pressure spark plasma sintering, J. Am. Ceram. Soc. 94 (2011) 3206–3210.

[18] R. Chaim, A. Shlayer, C. Estournes, Densification of nanocrystalline Y_2O_3 ceramic powder by spark plasma sintering, J. Eur. Ceram. Soc. 29 (2009) 91–98.

[19] H. Furuse, S. Nakasawa, H. Yoshida, et al., Transparent ultrafine Yb^{3+}:Y_2O_3 laser ceramics fabricated by spark plasma sintering, J. Am. Ceram. Soc. 101 (2018) 694–702.

[20] S.F. Wang, J. Zhang, D.W. Luo, et al., Transparent ceramics: Processing, materials and applications, Prog. Sol. Stat. Chem. 41 (2013) 20–54.

[21] L. An, A. Ito, T. Goto, Effect of sintering temperature on the transparency and mechanical properties of lutetium aluminum garnet fabricated by spark plasma sintering,

J. Eur. Ceram. Soc. 32 (2012) 3097–3102.

[22] B.N. Kim, K. Hiraga, K. Morita, et al., Dynamic grain growth during low-temperature spark plasma sintering of alumina, Scr. Mater. 80 (2014) 29–32.

[23] K. Morita, B.N. Kim, H. Yoshida, et al., Spectroscopic study of the discoloration of transparent $MgAl_2O_4$ spinel fabricated by spark-plasma-sintering (SPS) processing, Acta Mater. 84 (2015) 9–19.

[24] Q. Meng, X. Wang, Q. Zhu, J.G. Li, The effects of Mg^{2+}/Si^{4+} co-substitution for Al^{3+} on sintering and photoluminescence of $(Gd,Lu)_3Al_5O_{12}$:Ce garnet ceramics, J. Eur. Ceram. Soc. 40 (2020) 3262–3269.

[25] S. Grasso, C. Hu, G. Maizza, et al., Effects of pressure application method on transparency of spark plasma sintered alumina, J. Am. Ceram. Soc. 94 (2011) 1405–1409.

[26] B. Choundhury, P. Chetri, A. Choundhury, Annealing temperature and oxygen-vacancy-dependent variation of lattice strain, band gap and luminescence properties of CeO_2 nanoparticles, J. Exp. Nanosci. 10 (2015) 103–114.

[27] K. Morita, B.N. Kim, H. Yoshida, et al., Distribution of carbon contamination in oxide ceramics occurring during spark-plasma-sintering (SPS) processing: II – Effect of SPS and loading temperatures, J. Eur. Ceram. Soc. 38 (2018) 2596–2604.

[28] P. Palmero, B. Boneli, G. Fantozzi, et al., Surface and mechanical properties of transparent polycrystalline YAG fabricated by SPS, Mater. Res. Bull. 48 (2013) 2589–2597.

[29] T. Benitez, S.Y. Gomez, A. Oliveira, et al., Transparent ceramic and glass-ceramic materials for armor applications, Ceram. Int. 43 (2017) 13031–13046.

[30] S. Feng, H. Qin, G. Wu, et al., Spectrum regulation of YAG:Ce transparent ceramics with Pr, Cr doping for white light emitting diodes application, J. Eur. Ceram. Soc. 37 (2017) 3403–3409.

[31] Y.H. Li, G.Y. Hong, Synthesis and luminescence properties of nanocrystalline Gd_2O_3:Eu^{3+} by combustion process, J. Lumin. 124 (2007) 297–301.

[32] Z. Sun, Z. Chen, M. Wang, et al., Production and optical properties of Ce^{3+}-activated and Lu^{3+}-stabilized transparent gadolinium aluminate garnet ceramics, J. Am. Ceram. Soc. 103 (2020) 809–818.

[33] J.S. Li, X.M. Han, L. Wu, et al., Photoluminescence properties of $(Y_{1-x}Ce_x)_3Al_5O_{12}$ (x = 0.005–0.03) nanophosphors and transparent ceramic by a homogeneous co-precipitation method, J. Lumin. 206 (2019) 364–369.

Chapter 5. Fabrication of transparent Ce^{3+}:$(Gd,Lu)_3Al_5O_{12}$ by two-step SPS

5.1. Introduction

The lanthanide aluminate garnets ($Ln_3Al_5O_{12}$, LnAG), represented by $Gd_3Al_5O_{12}$ (GdAG) and $Lu_3Al_5O_{12}$ (LuAG), with high theoretical density are attractive candidates for scintillator applications. The LnAG group shows the proper characteristics for scintillator applications, such as wide bandgaps, chemical and thermal stabilities, and wide transparent range [1–4]. The high theoretical density of the scintillator is very important to assure high X-ray stopping power. Regretfully, YAG shows the relatively low stopping power by its low density (4.53 g/cm^3). Among the lanthanide elements with an atomic weight higher than Y (89), the Gd (157) and Lu (174) are considered suitable not only for increasing the density of the garnet structure. Based on the abundance of rare earth elements in the earth's crust, the Gd (0.21 ppm) and Lu (0.02 ppm) have lower abundance compared to Y (1.39 ppm) [5]. However, since Gd is more abundant than Lu, it is more suitable as a substitute for Y. Recently, research on transparent LnAG based on Gd has been actively conducted for scintillator applications. However, the GdAG has the disadvantage, which is thermally decomposed into $GdAlO_3$ perovskite and Al_2O_3 above 1300°C ($Gd_3Al_5O_{12} \rightarrow 3GdAlO_3 + Al_2O_3$) [6]. Especially, Ce^{3+} is doped for an activator of the yellow-emitting phosphors, and the ionic radius of Ce^{3+} is larger than that of Gd^{3+}. The larger Ce^{3+} ions cause destabilization of the garnet structure, thereby reducing the thermal decomposition temperature. In order to suppress the reduction of thermal decomposition, the reported research [7] proposed that the doping the much smaller Lu^{3+} in Ce-doped GdAG with reducing the average Ln^{3+} size for structural stabilization. Consequently, the doping of Lu^{3+} retains the photoluminescence (PL) characteristics of Ce^{3+} and increases the theoretical density of the Ce^{3+}:$(Gd,Lu)_3Al_5O_{12}$, and the advanced yellow-emitting phosphors was obtained [7].

Decreasing the sintering temperature can prevent thermal decomposition of GdAG above 1300°C and improve the mechanical properties with the dense microstructure. The spark plasma sintering (SPS) controlled by electric field and mechanical pressure can be considered [8,9]. In the SPS process, the electric field rapidly heats the mold and powder compact, improving the rapid densification by a number of microscopic mechanisms, including increased atom diffusivity and softening of particle surfaces, so that excessive grain growth is suppressed at low temperature [8,10]. Therefore, high densities and fine microstructures, which are advantages of SPS, improve ceramics' mechanical and optical properties. Recently, the fabrication and characterization of LuAG ceramics, such as Nd:YAG [11], LuAG [12], and Ce^{3+}:$(Gd,Lu)_3Al_5O_{12}$ [13], using the SPS process have been reported [11–13]. Sufficient transparency can be obtained by conventional sintering, hot pressing (HP), and hot isostatic pressing (HIP) [14–16], but fabrication of transparent LnAG using SPS process has not been sufficiently studied. In our previous work [13], the Ce^{3+}:$(Gd,Lu)_3Al_5O_{12}$ powder was fully densified using SPS process, but a transparent sample was not obtained. Therefore, it is considered that further research is required to improve transparency while retaining the intrinsic merits of the SPS technique.

Research to improve the optical properties and control the microstructure by applying the two-step sintering profile in conventional sintering, HP, and HIP have been steadily reported [16–19]. The reported papers on the two-step sintering profile suggested that preliminary experiments on microstructure control should be preceded to improve the optical properties [18,19]. Although the two-step sintering profile was applied in different ways, in common, the main objective was to achieve primary densification without excessive coarsening at the higher first-step temperature and full densification and removal of residual pores in the second-step sintering. As a result, full densification could be effectively achieved by dividing it into two steps with different objectives. In addition, some papers have been reported that the two-step profile is applied to improve the optical properties while retaining the intrinsic merits of the SPS process [20–24]. In the SPS process, the two-step profile is applied slightly differently since the amount of carbon contamination and residual pores inevitably increases with increasing the sintering time. Considerable research [22,23] divided each stage of the two-step profile in detail and investigated the microstructure and optical properties. After primary densification without excessive coarsening when the first-step temperature was lower than the second-step, sufficient densification and excellent transparency could be obtained by removing the residual defects at the second-step temperature. In our previous work [24], in transparent Y_2O_3 fabricated with lower first-step temperature, the microstructural control and improvement of optical properties could be achieved. Based on the reported two-step profile results, the achievement of fine and dense microstructure and improvement of transmittance can be expected in LnAG as well as at low temperatures by suppressing excess coarsening and dividing primary densification and full densification.

This study was focused on improving he optical property of transparent Ce^{3+}:$(Gd,Lu)_3Al_5O_{12}$ ceramics with microstructure control by a two-step SPS profile. In the two-step profile, the primary densification and the suppression of the excessive coarsening were achieved at first-step sintering, and the full densification and removal of residual pores were accompanied at the second-step sintering. The microstructure refinement or control depended on the first-step temperature, and as a result, high transparency with finer microstructure was able to be achieved compared to the single-step profile.

5.2. Experimental Procedure

The rare-earth and aluminum sources in the present work were Ln_2O_3 (Ln = Gd and Lu, 99.99%, Huizhou RUIER Rare-Chem. Hi-Tech, China), $Ce(NO_3)_3 \cdot 6H_2O$ (99.99%, Huizhou Ruier Rare-Chem. Hi-Tech, China) and alum ($NH_4Al(SO_4)_2 \cdot 12H_2O$, > 99%, Zhenxin Chemical Reagent Factory, China). The $Ln(NO_3)_3$ stock solution was prepared by dissolving the oxide powders in an appropriate amount of nitric acid. To precipitate the carbonate precursor, a mixed solution containing stoichiometric amounts of nitrates and alum was added dropwise to the ammonium bicarbonate solution. The precipitated carbonate precursor was dried in oven for 24 h. The $[(Gd_{0.6}Lu_{0.4})_{0.99}Ce_{0.01}]_3Al_5O_{12}$ powder was obtained by thermal decomposition of the precursor, through first calcination at 1100°C for 4 h in air. To suppress the oxidation of Ce^{3+}, second calcination was performed at 1000°C for 4 h in Ar/H_2 (5 vol% of H_2) [7,25].

The Ce^{3+}:$(Gd,Lu)_3Al_5O_{12}$ powder was consolidated using SPS equipment (LABOX-315, Sinter Land, Japan) under a vacuum atmosphere of 10 Pa. The powder was directly sintered without any pre-treatment, using a graphite mold of 10 mm diameter. Heating was performed with a pulse pattern of AC mode with a period of 5 s, and the temperature was measured using a pyrometer in the non-through hole of the mold. The whole SPS process were divided into a single-step profile and two-step profile. In case of the single-step profile, the powder compact was heated to sintering temperature of 1250°C with a heating rate of 50°C/min, and held for 20 min. In case of the two-step profile, to primary densification without excessive coarsening, the first-step sintering was performed to 900, 1000, and 1200°C with a heating rate of 50°C/min and held for 30 min. In the single-step profile, the shrinkage started around 1000°C, so the first-step temperatures for the two-step profile were considered based on 1000°C. For the full densification and removal of residual pores, further heating was conducted to second-step temperature of 1250°C at 5°C/min and held for 20 min. In whole SPS process, the mechanical pressure of 6.5 kN (80 MPa) was applied from the beginning and was kept until before cooling.

In addition, the cooling was sequentially proceeded to 1100°C for 10 min, to 800°C for 5 min, and to 25°C for 5 min. The detailed SPS conditions and specimen names were summarized in Table 5.

Table 5. Detailed conditions of SPSed Ce^{3+}:$(Gd,Lu)_3Al_5O_{12}$ ceramics.

No.	Specimen name	SPS profile		Heating rate	Range (°C)	Holding stage
1	SS-1250	Single-step profile		50°C/min	600–1250	@ 1250°C for 20 min
2	TS-900	Two-step profile	1st step 2nd step	50°C/min 5°C/min	600–900 900–1250	@ 900°C for 30 min @ 1250°C for 20 min
3	TS-1000		1st step 2nd step	50°C/min 5°C/min	600–1000 1000–1250	@ 1000°C for 30 min @ 1250°C for 20 min
4	TS-1200		1st step 2nd step	50°C/min 5°C/min	600–1200 1200–1250	@ 1200°C for 30 min @ 1250°C for 20 min

The annealing process was conducted at 1250°C for 10 h in air to remove the carbon contamination and oxygen vacancies. Both surfaces of Ce^{3+}:$(Gd,Lu)_3Al_5O_{12}$ ceramics were mirror polished with diamond paste of 9, 3, and 1 μm. Transmittance was measured using a double-beam spectrophotometer (SolidSpec-3700DUV, Shimazu, Japan) equipped with an integrating sphere. The PL measurements were conducted using a spectrofluorometer (FP-6500, JASCO, Japan) equipped with a 60 mm diameter integrating sphere (Model ISF-513, JASCO, Japan) and a 150 W Xe lamp as the excitation source. X-ray photoelectron spectroscopy (XPS, AXIS-165, Shimadzu, Japan) spectra were recorded at room temperature with Al-K_α radiation for excitation and with the binding energy referenced to the C-1 s line of adventitious carbon. The mirror polished surfaces were thermally etched at 1100°C for 2 h in air. The polished surfaces and fracture surfaces were observed using a scanning electron microscope (SEM, SU-8000, Hitachi, Japan). The porosity was obtained by measuring the porous area in SEM images. The grain and pore sizes were calculated by measuring the average cross-section area per grain and pore. The grain size is an apparent one in cross section, so that it was multiplied by 1.225 to determine the true grain size [26].

5.3. Results and Discussion

5.3.1. Shrinkage Behavior and Microstructure

Through our previous work, the stabilization of garnet structure of $(Gd,Lu)_3Al_5O_{12}$ was successfully achieved, and it well-indexed with the cubic structure of GdAG [13]. Single-step and two-step SPS profiles were applied to fabricate the transparent $(Gd,Lu)_3Al_5O_{12}$ ceramics with structure stabilization. The SPS curves (temperature, displacement, and pressure by the time) of single-step profile (SS-1250) was presented in Fig. 40 (a). In the displacement curve, thermal expansion by heating up to around 1000°C was observed, and shrinkage began to occur. No further shrinkage occurred during the holding period at 1250°C, and the shrinkage was sufficient. Based on the SPS curves of the single-step profile (SS-1250), a two-step profile (TS-1000) was designed, which is presented in Fig. 40 (b). At the relatively low first-step temperature of 1000°C, the powder compact was rapidly heated at a 50°C/min to suppress the excessive coarsening and primary densification was conducted for 30 min [20,22,24]. In addition, during the first-step holding time, since the shrinkage began and did not occur rapidly, a small amount of residual pore could be expected. Due to the achievement of the primary densification including a small amount of residual pore in the first-step sintering, the shrinkage of the two-step profile was completed at 1200°C, about 50°C lower than the 1250°C of the single-step profile, although the amount of shrinkage was the almost same. The improvement of the sintering behavior by the two-step profile not only enables microstructure control, but also can be expected to improve the optical properties.

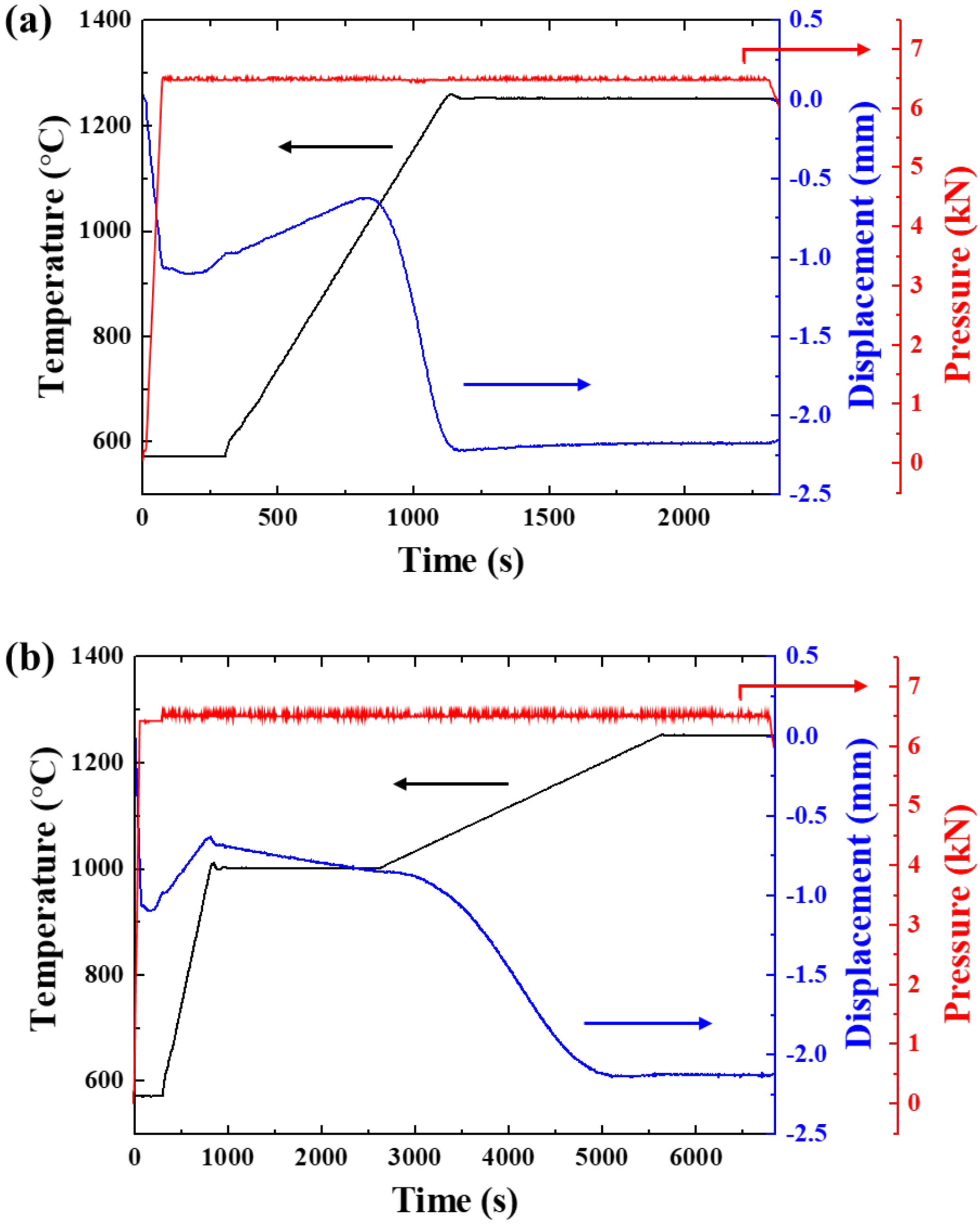

Fig. 40. SPS curves of the sintered Ce^{3+}:$(Gd,Lu)_3Al_5O_{12}$ ceramics depending on (a) single-step SPS profile (SS-1250) and (b) two-step SPS profile (TS-1000).

Fig. 41 shows the SEM images of cross-section of SPSed Ce^{3+}:$(Gd,Lu)_3Al_5O_{12}$ ceramics after annealing. All specimens were densified at final sintering temperature of 1250°C. However, the microstructure was different in grain size, pore size, and porosity on SPS profiles. The microstructural information (grain size, pore size, and porosity) calculated from SEM images was summarized in Table 6. By applying the two-step profile, it was possible to significantly lower the porosity at the same sintering temperature. All two-step SPSed specimens showed lower porosity compared to single-step SPSed specimen (SS-1250) (3.74%), in particular, specimen TS-1000 exhibited a porosity of 1.63% and a significant reduction in porosity was possible. Significant decrease in porosity was possible due to the improvement of shrinkage behavior, such as a smaller amount of residual pore and lower shrinkage completion temperature, as shown in Fig. 41. In addition, as the first-step temperature was lowered in the two-step profile, the grain size gradually decreased from 207 nm to 139 nm, and the pore size decreased from 72 nm to 43 nm. This microstructure change was made possible by microstructure control by the two-step profile [18,19]. In the present work, microstructure control by two-step profile is expected to enable the improvement of optical properties as well.

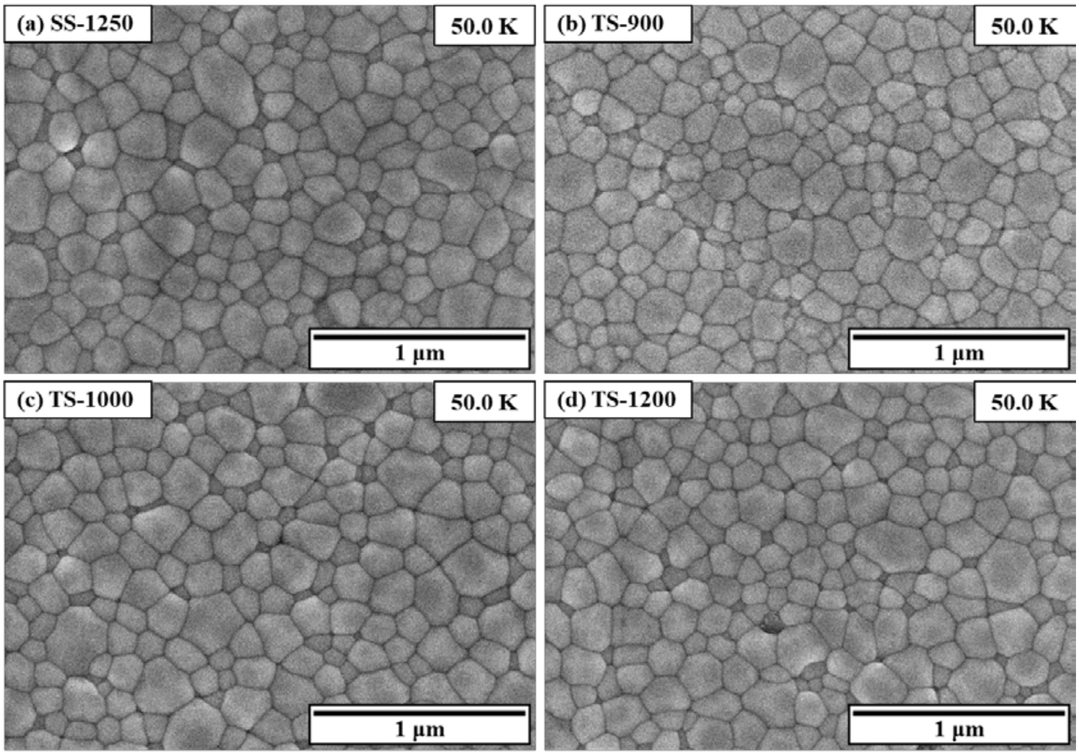

Fig. 41. SEM images of cross-section of SPSed Ce^{3+}:$(Gd,Lu)_3Al_5O_{12}$ ceramics. (a) is SS-1250, (b) is TS-900, (c) is TS-1000, and (d) is TS-1200.

Table 6. Microstructural information of SPSed Ce^{3+}:$(Gd,Lu)_3Al_5O_{12}$ ceramics.

No.	Specimen name	Grain size	Pore size	Porosity
1	SS-1250	221 nm	81 nm	3.74%
2	TS-900	139 nm	43 nm	2.29%
3	TS-1000	163 nm	69 nm	1.63%
4	TS-1200	207 nm	72 nm	2.96%

5.3.2. Optical Appearance and Transmittance

The optical appearances of Ce^{3+}:$(Gd,Lu)_3Al_5O_{12}$ ceramics after annealing were summarized in Fig. 42. In the previous chapter, to improve the optical transparency, the discoloration by carbon contamination could be recovered by annealing process. The elimination of carbon contamination and oxygen vacancies was significantly affected the improvement of optical transparency. Through the annealed specimens placed on the grid, the optical appearance and transparency can be easily compared briefly. Specimen SS-1250 showed the lowest optical transparency among all the specimens. As a result of applying the modified two-step profile based on the single-step profile (SS-1250), the optical appearance was improved. Of course, it could be determined that the optical appearance was improved by decreasing the heating rate in the second-step. However, among them, the most pronounced improvement was obtained at 1000°C as the first-step sintering temperature in the two-step profile. It means that a decrease in the heating rate at the critical temperature for densification had a more important effect rather than simply reducing the heating rate to improve the optical appearance. Therefore, as a result of setting the first-step sintering temperature of 1000°C, the porosity was the lowest and the optical appearance was also improved the most. Based on the results of the microstructure and optical appearance, it can be expected that the highest transmittance in the specimen TS-1000 will be obtained.

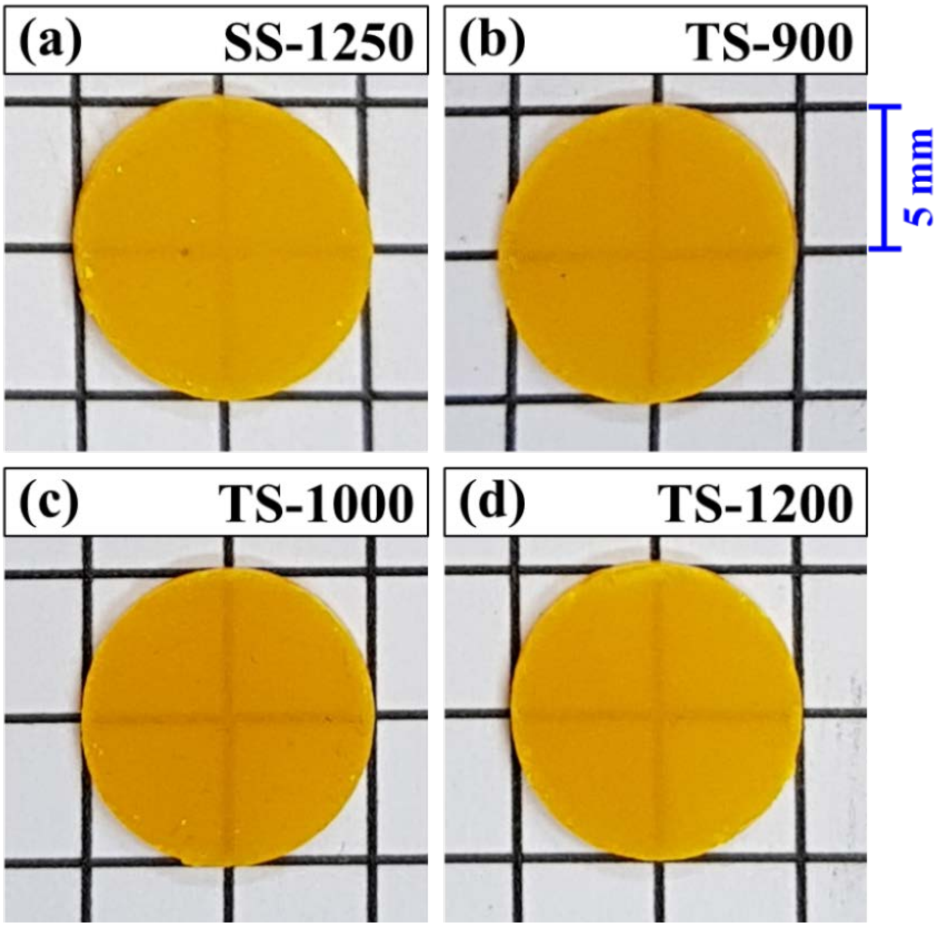

Fig. 42. Optical appearance of SPSed Ce^{3+}:$(Gd,Lu)_3Al_5O_{12}$ ceramics. (a) is SS-1250, (b) is TS-900, (c) is TS-1000, and (d) is TS-1200.

Fig. 43 shows the in-line transmittance (ILT) curves of sintered Ce^{3+}:$(Gd,Lu)_3Al_5O_{12}$ ceramics after annealing. Significant light absorption was observed around 340 nm and in the range of 420–500 nm. Due to the light absorption by the $4f \rightarrow 5d_2$ and $4f \rightarrow 5d_1$ transitions of Ce^{3+}, the strong absorption around 340 nm and in the range of 420–500 nm occurred, respectively [27]. As observed in optical appearances, the transmittance results also showed almost same trend. At the same sintering temperature of 1250°C, all the specimens sintered with the two-step profile compared to the single-step profile certainly showed improved transmittance curves. Among them, the specimen TS-1000 showed the most improved ILT of 56.5% at 1000 nm compared to the 50.1% of specimen SS-1250. In transparent ceramics, the area of the grain boundary also affects the transmittance, but the porosity is the most critical factor [28]. In the specimen TS-1000, which was conducted at the first-step sintering of 1000°C, where the shrinkage began, the porosity showed a significant decrease from 3.74% (SS-1250) to 1.63% (TS-1000), and this result had a profound effect on the transmittance. In addition, the porosity's trend presented in Table 6 exactly matched the trend of transmittance. The two-step profile of the specimen TS-1000 slightly reduced the grain and pore sizes through microstructure control and reduced the porosity the most. The decrease in porosity, which had the most critical effect on transmittance, resulted in the most noticeable improvement in transmittance. $(Gd,Lu)_3Al_5O_{12}$:Ce ceramics with a composition similar to that of the present work were fabricated with conventional sintering at 1750°C for 4 h under the vacuum atmosphere after cold isostatic press (CIP) at 240 MPa [14]. As a result, an ILT of about 72% at 1000 nm was achieved, showing excellent optical properties. Although there have been reported results of achieving full densification and high transmittance of the garnet material with the conventional sintering method, it was difficult to obtain high transmittance with the SPS method. It has been reported that Nd:YAG ceramics were fabricated by the reactive-SPS method to which a two-step heating profile was applied [29]. Nd:YAG powder was heated at 100°C/min to the first-step sintering temperature (1000°C) with an applied pressure of 70 MPa, and at 15°C/min to the second-step sintering temperature (1350°C), then 5 min were maintained. However, an ILT of about 36% at 1000 nm was obtained and excellent optical properties were not achieved. In the present work, although ILT is not close to the theoretical value of 84%, it has realized a very positive expectation that transmittance can be improved through the application of the two-step profile and the microstructure control accordingly.

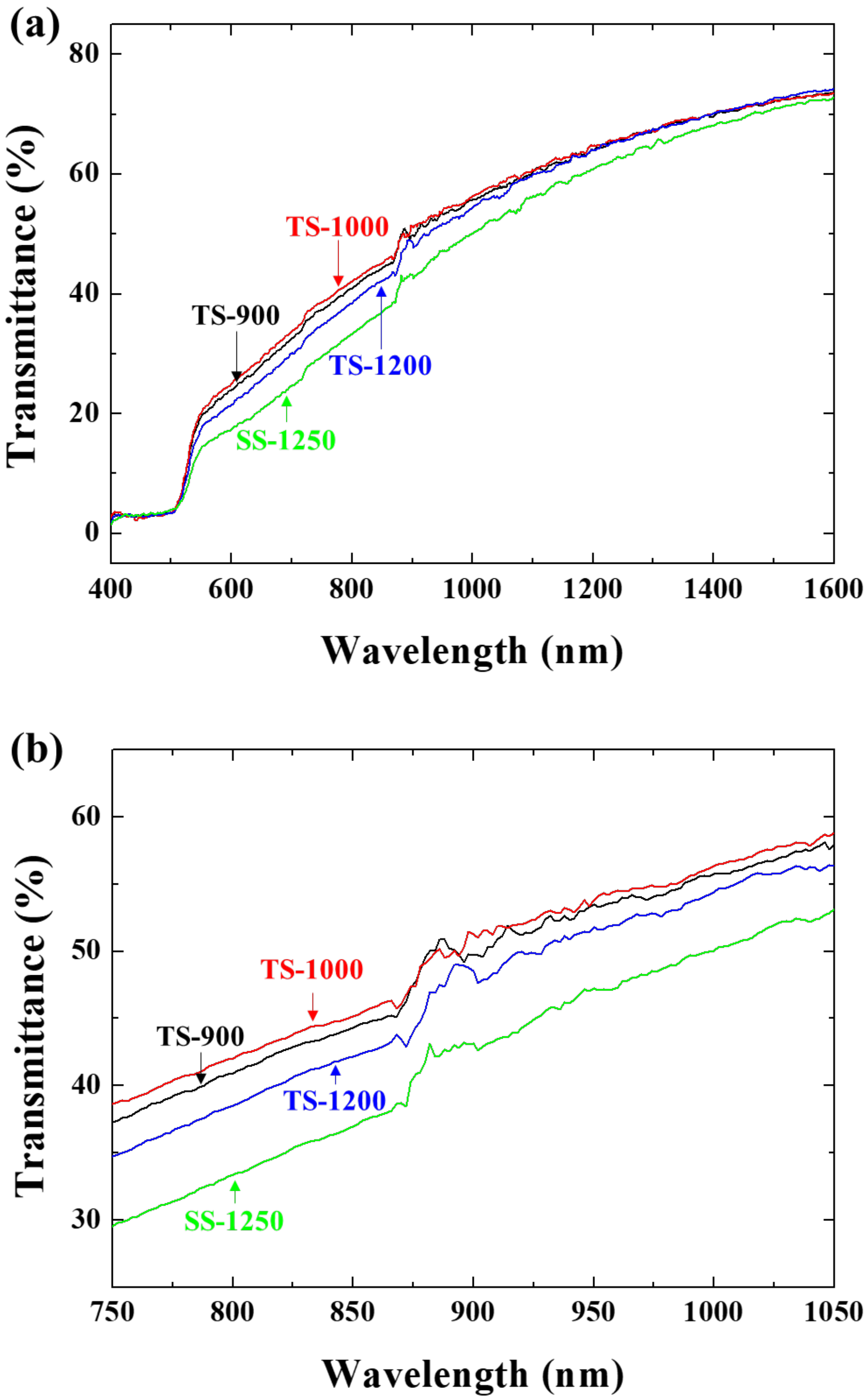

Fig. 43. Transmittance curves of SPSed Ce^{3+}:$(Gd,Lu)_3Al_5O_{12}$ ceramics after annealing. (b) is a graph magnified in the range of 750–1050 nm.

5.3.3. Oxidation State and PL Characteristics

To analyze the distribution of Ce dopant in vertical and horizontal directions of SPSed samples, SEM image and EDS mapping results of single-step profile (SS-1250) and two-step profile (TS-1000) were shown in Figs. 44 and 45, respectively. Since the electric current and temperature gradient may be induced by non-conductive ceramic powder compacts, the analysis of the distribution of Ce dopant is required. The Ce^{3+}:$(Gd,Lu)_3Al_5O_{12}$ powder was successfully synthesized so that the Ce dopant could be uniformly distributed, and its uniform distribution was well maintained even after both SPS profiles. Therefore, no difference in the PL characteristics by the concentration gradient of Ce dopant will be considered.

The XPS measurement was conducted to investigate the oxidation state of Ce dopant, the results of powder, single-step profile (SS-1250), and two-step profile (TS-1000) were summarized in Fig. 46. The red line belongs to the spectra of Ce^{3+} ion, the blue line is the spectra of Ce^{4+} ion, and fractions of Ce^{3+} and Ce^{4+} ion were calculated by the area of each spectrum. For comparison with samples sintered in single-step and two-step profiles, the fraction of Ce^{3+} in the as-synthesized powder was required. The fraction of Ce^{3+} in powder was 61.42% in Fig. 46 (a). In case of the specimen SS-1250, the fraction of Ce^{3+} was 61.73%, which was almost the same as that of the synthesized powder. However, in the specimen TS-1000, oxidation occurred slightly, and the fraction of Ce^{3+} was 60.66%. Since the SPS process is an oxidizing atmosphere by graphite components, the oxidation occurred in the two-step profile with a long sintering time, and the fraction of Ce^{3+} was slightly reduced. A slightly decreased fraction of Ce^{3+} in the two-step profile will affect the PL characteristics along with the microstructure.

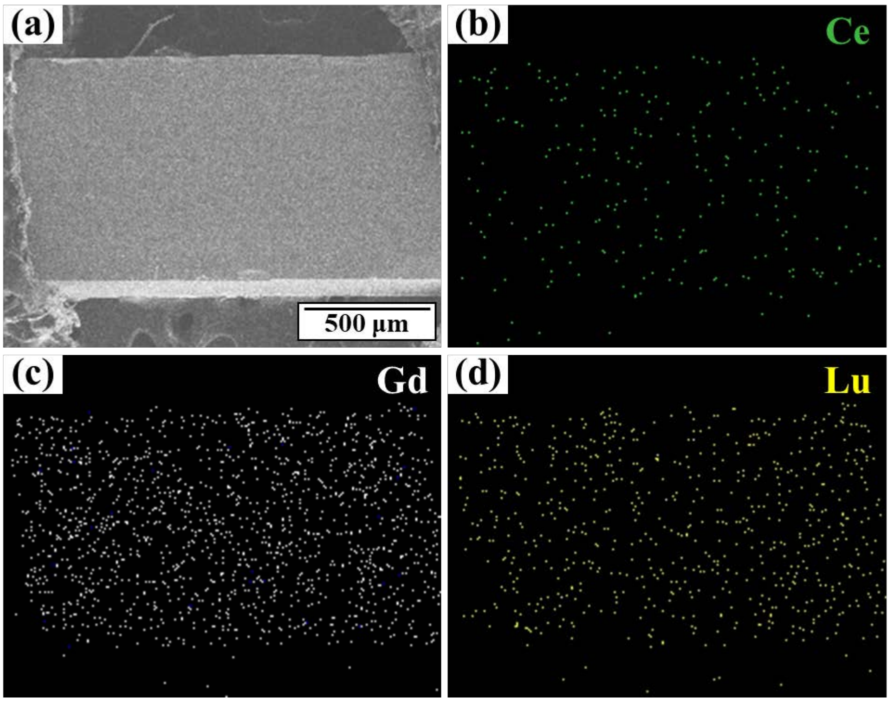

Fig. 44. (a) SEM image of cress-section of the SS-1250 sample sintered with single-step SPS profile, and EDS mapping images of (b) Ce, (c) Gd, and (d) Lu.

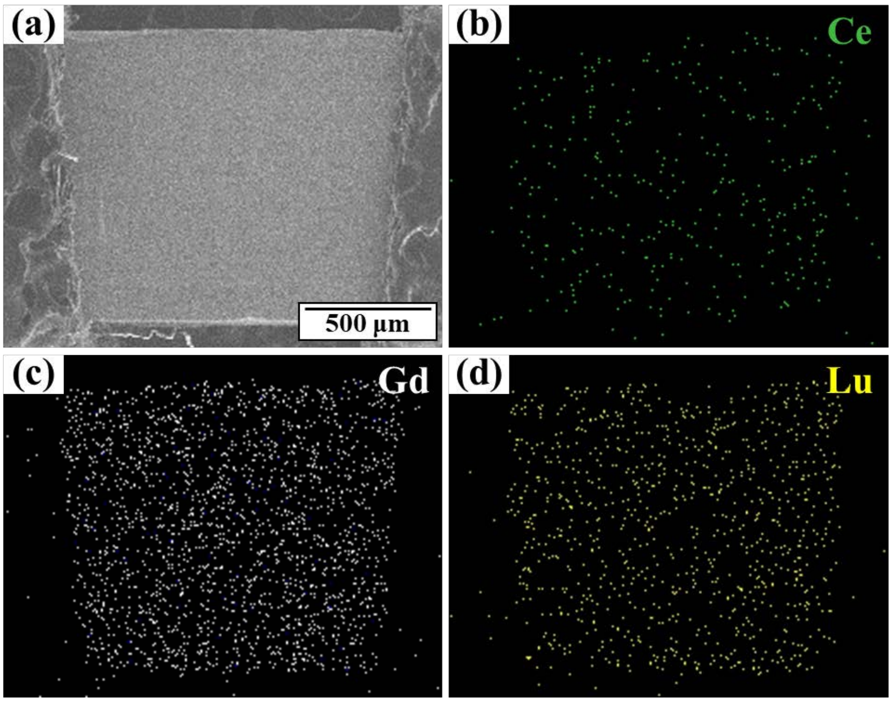

Fig. 45. (a) SEM image of cress-section of the TS-1000 sample sintered with two-step SPS profile, and EDS mapping images of (b) Ce, (c) Gd, and (d) Lu.

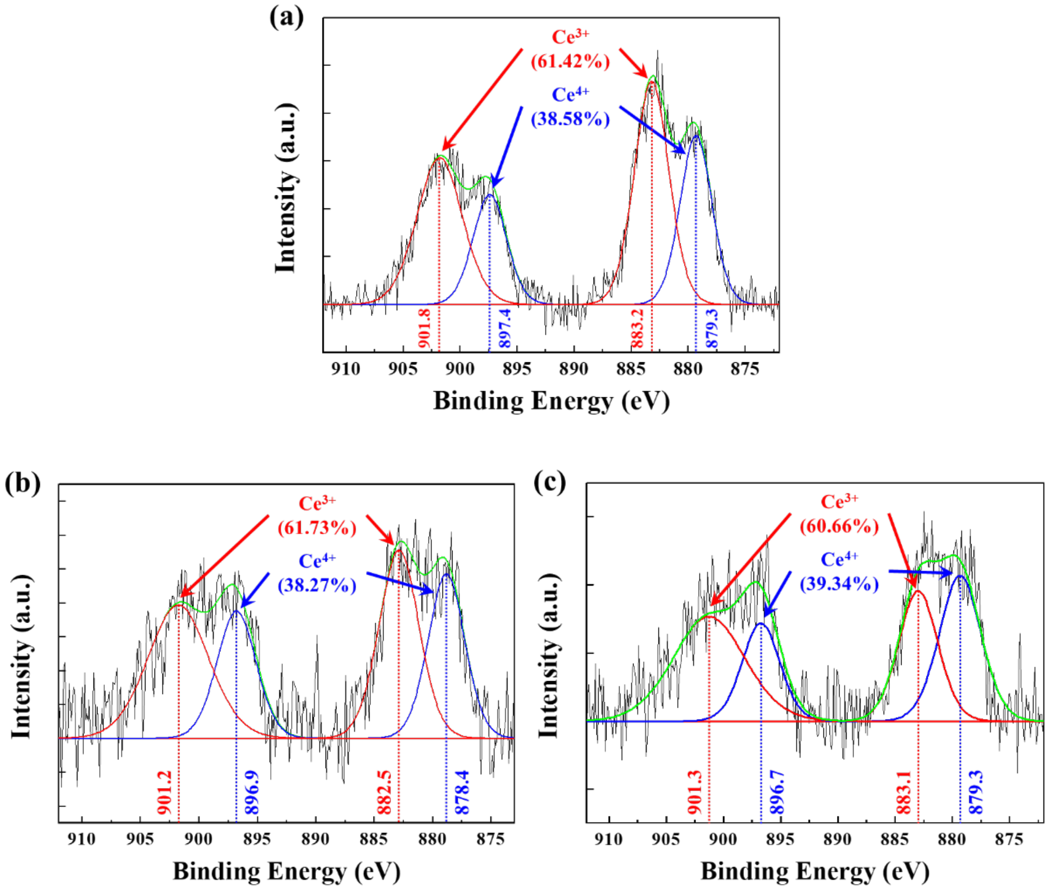

Fig. 46. XPS spectra of (a) Ce^{3+}:$(Gd,Lu)_3Al_5O_{12}$ powder, (b) single-step SPSed sample (SS-1250), and (c) two-step SPSed sample (TS-1000).

Fig. 47 (a) shows the PL excitation spectra of Ce^{3+}:$(Gd,Lu)_3Al_5O_{12}$ samples after annealing. The PL excitation measurement was performed to investigate wavelength-dependent excitation under the condition that light at 571 nm was emitted. The excitation bands around 342, 453, and 506 nm were detected, all of which belong to the excitation of Ce^{3+} [30,31]. The excitation around 342 nm occurred by the transition from the ground state ($2F_{5/2}$) of Ce^{3+} to the T_{2g} state, and the excitation around 453 and 506 nm was the transition from the ground state to the E_{2g} state composed of two individual bands [30,31]. The specimen SS-1250 sintered with the single-step profile exhibited evidently higher PL excitation intensity compared to the two-step profile. Independent of the first-step temperature in the two-step profile, the PL excitation intensity was lowest in the specimen TS-1000. The transmittance was strongly influenced by the porosity and two-step profile showed better results, but PL excitation characteristic was different. First, the fraction of Ce^{3+} in Fig. 46 directly affected the PL excitation characteristic. In the PL excitation spectra, since the excitation is caused by only Ce^{3+} [30,31], the fraction of Ce^{3+} contained in the Ce^{3+}:$(Gd,Lu)_3Al_5O_{12}$ is a very important factor. Next, the grain size of the specimen SS-1250 was the largest as 221 nm, and the grain size gradually decreased from 207 to 139 nm as the first-step temperature decreased. Compared to the two-step profile, the large grain size, and the small area of grain boundaries of the single-step profile might affect the PL excitation characteristics [32,33]. Fig. 47 (b) shows the PL emission spectra of Ce^{3+}:$(Gd,Lu)_3Al_5O_{12}$ ceramics after annealing. Through the PL emission measurement, wavelength-dependent emission under the condition that light at 453 nm was excited was investigated. The PL emission characteristics were showed completely identical trend with PL excitation characteristics. The full-width at half maximum (FWHM) values were almost same in whole specimens. It means that the crystallinity and light clarity of all specimens are almost the same, and that the two-step profile did not affect the PL emission characteristics.

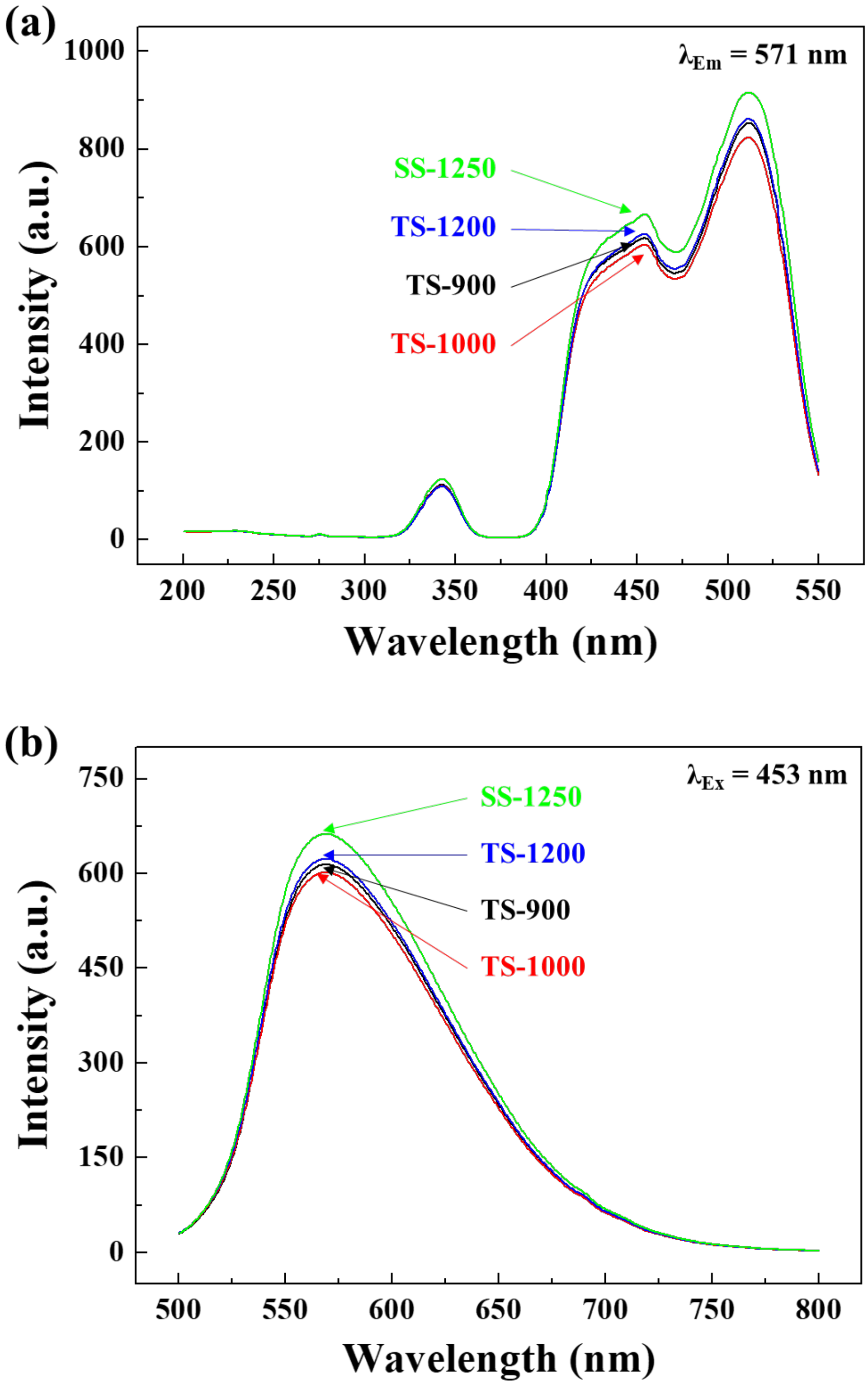

Fig. 47. (a) PL excitation and (b) PL emission spectra of Ce^{3+}:$(Gd,Lu)_3Al_5O_{12}$ ceramics depending on the SPS conditions after annealing.

5.4. Conclusions

In the present work, the two-step SPS profile was employed and investigated to improve the optical property of Ce^{3+}:$(Gd,Lu)_3Al_5O_{12}$ ceramics as attractive yellow-emitting phosphors. In the shrinkage curve of SPS process with a single-step profile, a significant reduction in porosity from 3.74% to 1.63% was achieved by first-step sintering of 1000°C in a two-step profile, where shrinkage began. As the first-step temperature decreased, the microstructure control of the two-step profile enabled the finer microstructure to reduce grain and pore sizes. As a result of the significant reduction in porosity in the two-step profile, the transmittance, which has the strong relationship with porosity, at 1000 nm could be improved from 50.1% to 56.5%. On the other hand, due to the long sintering time, oxidation occurred, and the fraction of Ce^{3+} decreased slightly in the two-step profile, so the PL excitation and PL emission characteristics were not improved.

References

[1] J.G. Li, Y. Sakka, Recent progress in advanced optical materials based on gadolinium aluminate garnet ($Gd_3Al_5O_{12}$), Sci. Technol. Adv. Mater. 16 (2015) 014902.

[2] M. Wang, B. Lu, Manufacture and Faraday magneto-optical effect of highly transparent novel holmium aluminum garnet ceramics, Scripta Mater. 195 (2021) 133729.

[3] M. Ayvacikli, A. Canimoglu, L.E. Muresan, L.B Tudoran, J.G. Guinea, Y. Karabulut, A. Jolge, T. Karali, N. Can, Structural and luminescence effects of Ga co-doping on Ce-doped yttrium aluminate based phosphors, J. Alloys. Compd. 666 (2016) 447–453.

[4] C. Kim, W. Lee, A. Melis, A. Elmughrabi, K. Lee, C. Park, J.Y. Yeom, A Review of Inorganic Scintillation Crystals for Extreme Environments, Crystals 11 (2021) 669.

[5] V. Balaram, Rare earth elements: A review of applications, occurrence, exploration, analysis, recycling, and environmental impact, Geosci. Front. 10 (2019) 1285–1303.

[6] T. Shishido, K. Okamura, S. Yajima, $Gd_3Al_5O_{12}$ Phase Obtained by Crystallization of Amorphous $Gd_2O_3{\cdot}5/3Al_2O_3$, J. Am. Ceram. Soc. 61 (1978) 373–375.

[7] J. Li, J.G. Li, S. Liu, X. Li, X. Sun, Y. Sakka, The development of Ce^{3+}-activated $(Gd,Lu)_3Al_5O_{12}$ garnet solid solutions as efficient yellow-emitting phosphors, Sci. Technol. Adv. Mater. 14 (2013) 054201.

[8] B.N. Kim, K. Morita, T.S. Suzuki, J.G. Li, H. Matsubara, Simulation of densification behavior of nano-powder in final sintering stage: Effect of pore-size distribution, J. Eur. Ceram. Soc. 41 (2021) 625–634.

[9] M. Tokita, Progress of Spark Plasma Sintering (SPS) Method, Systems, Ceramics Applications and Industrialization, Ceramics 4 (2021) 160–198.

[10] A. Wagner, Y. Meshorer, B. Ratzker, D. Sinefeld, S. Kalabukhov, S. Goldring, E. Galun, N. Frage, Pressure-assisted sintering and characterization of Nd:YAG ceramic lasers, Sci. Rep. 11 (2021) 1512.

[11] A. Wagner, B. Ratzker, S. Kalabukhov, S. Kolusheva, M. Sokol, N. Frage, Highly-doped Nd:YAG ceramics fabricated by conventional and high pressure SPS, Ceram. Int. 45 (2019) 12279–12284.

[12] S.F. Wang, J. Zhang, D.W. Luo, F. Gu, D.Y. Tang, Z.L. Dong, G.E.B. Tan, W.X. Que, T.S. Zhang, S. Li, L.B. Kong, Transparent ceramics: Processing, materials and applications, Prog. Solid. State. Chem. 41 (2013) 20–54.

[13] J.H. Lee, J.G. Li, B.N. Kim, Q. Meng, X. Sun, B.K. Jang, Effect of annealing on microstructure and luminescence characteristics in spark plasma sintered Ce^{3+}-activated $(Gd,Lu)_3Al_5O_{12}$ garnet ceramics, J. Eur. Ceram. Soc. 41 (2021) 1586–1592.

[14] Z. Sun, Z. Chen, M. Wang, B. Lu, Production and optical properties of Ce^{3+}-activated and Lu^{3+}-stabilized transparent gadolinium aluminate garnet ceramics, J. Am. Ceram. Soc. 103 (2020) 809–818.

[15] X. Chen, X. Liu, Y. Feng, X. Li, H. Chen, T. Xie, H. Kou, R. Kucerkova, Microstructure evolution in two-step-sintering process towardtransparent $Ce:(Y,Gd)_3(Ga,Al)_5O_{12}$ scintillation ceramics. J Alloys Compd. 2020;846;156377.

[16] J. Li, Q. Chen, G. Feng, W. Wu, D. Xiao, J. Zhu, Optical properties of the polycrystalline transparent Nd:YAG ceramics prepared by two-step sintering, Ceram. Int. 38S (2012) S649–S652.

[17] Z. Seeley, N. Cherepy, S. Payne, Two-step sintering of $Gd_{0.3}Lu_{1.6}Eu_{0.1}O_3$ transparent ceramic scintillator, Opt. Mater. Express. 3 (2013) 908–912.

[18] W.K. Jung, H.J. Ma, D.G. Kim, D.K. Kim, Two-step sintering behavior of titanium-doped Y_2O_3 ceramics with monodispersed sub-micrometer powder, Ceram. Int. 45 (2019) 510–515.

[19] H.J. Ma, W.K. Jung, C. Baek, D.K. Kim, Influence of microstructure control on optical and mechanical properties of infrared transparent Y_2O_3-MgO nanocomposite, J. Eur.

Ceram. Soc. 37 (2017) 4902–4911.

[20] H. Furuse, S. Nakasawa, H. Yoshida, K. Morita, T.S. Suzuki, B.N. Kim, Y. Sakka, K. Hiraga, Transparent ultrafine Yb^{3+}:Y_2O_3 laser ceramics fabricated by spark plasma sintering, J. Am. Ceram. Soc. 101 (2018) 694–702.

[21] K. Morita, B.N. Kim, H. Yoshida, H. Zhang, K. Hiraga, Y. Sakka, Effect of loading schedule on densification of $MgAl_2O_4$ spinel during spark plasma sintering (SPS) processing, J. Eur. Ceram. Soc. 32 (2012) 2303–2309.

[22] M. Nanko, K.Q. Dan, Two-step pulsed electric current sintering of transparent Al_2O_3 ceramics, Adv. Appl. Ceram. 113 (2014) 80–84.

[23] H.H. Nguye, M. Nanko, Densification and grain growth of large-sized polycrystalline Al_2O_3 during a two-step pulsed electric current sintering process, Mater. Trans. 59 (2018) 1610–1615.

[24] J.H. Lee, B.N. Kim, B.K. Jang, Fabrication of transparent Y_2O_3 ceramics by two-step spark plasma sintering, J. Am. Ceram. Soc. 104 (2021) 5501–5508.

[25] J. Li, J.G. Li, X. Li, X. Sun, Photoluminescence properties of phosphors based on Lu^{3+}-stabilized $Gd_3Al_5O_{12}$:Tb^{3+}/Ce^{3+} garnet solid solutions, Opt. Mater. 62 (2016) 328–334.

[26] S. Grasso, C. Hu, G. Maizza, B.N. Kim, Y. Sakka, Effects of pressure application method on transparency of spark plasma sintered alumina, J. Am. Ceram. Soc. 94 (2011) 1405–1409.

[27] S. Feng, H. Qin, G. Wu, H. Jiang, J. Zhao, Y. Liu, Z. Luo, J. Qioa, J. Jiang, Spectrum regulation of YAG:Ce transparent ceramics with Pr, Cr doping for white light emitting diodes application, J. Eur. Ceram. Soc. 37 (2017) 3403–3409.

[28] T. Benitez, S.Y. Gomez, A. Oliveira, N. Travitzky, D. Hotza, Transparent ceramic and glass-ceramic materials for armor applications, Ceram. Int. 43 (2017) 13031–13046.

[29] D.Y. Kosyanov, A.A. Vornovskikh, A.M. Zakharenko, E.A. Gridasova, R.P. Yavetskiy,

M.V. Dobrotvorskaya, A.V. Tolmachev, O.O. Shichalin, E.K. Papynov, A.Y. Ustinov, V.G. Kuryavyi, A.A. Leonov, S.A. Tikhonov, Influence of sintering parameters on transparency of reactive SPSed Nd^{3+}:YAG ceramics, Opt. Mater. 112 (2021) 110760.

[30] X. Su, K. Zhang, Q. Liu, H. Zhong, Y. Shi, Y. Pan, Combinatorial Optimization of $(Lu_{1-x}Gd_x)_3Al_5O_{12}:Ce_{3y}$ Yellow Phosphors as Precursors for Ceramic Scintillators, ACS Comb. Sci. 13 (2011) 79–83.

[31] A. Birkel, K.A. Denault, N.C. George, C.E. Doll, B. Hery, A.A. Mikhailovsky, C.S. Birkel, B.C. Hong, R. Seshadri, Rapid Microwave Preparation of Highly Efficient Ce^{3+}-Substituted Garnet Phosphors for Solid State White Lighting, Chem. Mater. 24 (2012) 1198–1204.

[32] B. Wen, D.F. Zhang, N. Zhang, J.K. Feng, B. Jiang, F.S. Pan, Y. Zhang, L. Yang, Effect of grain size on the luminescent properties of Ce^{3+} doped $Y_3Al_5O_{12}$ ceramic phosphor plates, Ceram. Int. 46 (2020) 10452–10456.

[33] Y. Kim, S. Jang, Effect of particle size on photoluminescence emission intensity of ZnO, Acta Mater. 59 (2011) 3024–3031.

Chapter 6. Conclusions

During the SPS process of various transparent ceramics, deteriorating the optical transparency and inducing the non-uniform microstructure have been occasionally reported. In addition, the discoloration by precipitated carbon as by-products of carbon contamination with the carbon-rich environment of SPS components may critically affect the deteriorating the optical transparency. Therefore, the first objective is to overcome the severe drawbacks of the SPS process such as non-uniform sintering behavior, residual pores, and carbon contamination to improve the optical properties of transparent ceramics. Then, applying the microstructure refinement of two-step SPS profiles with primary densification and coarsening suppression at first-step to improve optical properties with finer microstructures in transparent Y_2O_3 and $RE_3Al_5O_{12}$ ceramics is final objectives. The following are outlined conclusions of each chapter.

Chapter 2. Non-Uniform Sintering Behavior in Transparent Y_2O_3 during SPS

The non-uniform microstructure of SPSed Y_2O_3 was investigated by microstructural and spectroscopic analysis. During the SPS process, the defects under the electric fields led to increased grain boundary mobility and coarsening. At high heating rates with stronger electric fields and rapid densification, the relatively large number of defects in the center region accompanied the rapid grain growth and coarsened microstructure. Consequently, during the SPS process, the coarsening was more dominant than the densification in the center and, unlike in the periphery, dramatically coarsened microstructures were induced.

Chapter 3. Fabrication of Highly Transparent Y_2O_3 by Two-Step SPS

The fabrication of transparent Y_2O_3 ceramics was accomplished using a two-step SPS process. SEM results showed that densification occurred sufficiently in all specimens, but the distribution of the ILT was significant. Since densification behavior was improved and microstructure control was achieved, applying the two-step SPS process significantly improved the ILT (63.1% (single-step SPS) → 80.6% (two-step SPS)). In two-step SPS, high-temperature loading of 80 MPa improved densification behavior by suppressing considerable agglomeration and accelerating atomic diffusion at high temperatures.

Chapter 4. Fabrication of Transparent Ce^{3+}:$(Gd,Lu)_3Al_5O_{12}$ by SPS

Since the carbon contamination and oxygen vacancies are inevitably induced during the SPS process, the transmittance of the as-sintered Ce^{3+}:$(Gd,Lu)_3Al_5O_{12}$ ceramics tended to decrease with holding time, and it was mostly recovered by annealing process. In the PL excitation characteristics after annealing, the positions of three bands were identical and, each spectrum’s intensity increased significantly. The carbon contamination and oxygen vacancies had the most critical effects than microstructures and were removed effectively by annealing. As a result, more PL excitation intensity improvements occurred with increasing the holding time because microstructure coarsening positively affected PL excitation characteristics.

Chapter 5. Fabrication of transparent Ce^{3+}:$(Gd,Lu)_3Al_5O_{12}$ by two-step SPS

A significant reduction in porosity from 3.74% (single-step SPS) to 1.63% (two-step SPS) was achieved in Ce^{3+}:$(Gd,Lu)_3Al_5O_{12}$ ceramics sintered with first-step sintering at 1000°C during two-step SPS. As the temperature of first-step sintering decreased, the microstructure control with two-step SPS enabled the finer microstructure with a reduction in porosity, grain size, and pore size. Consequently, the transmittance, which has a strong relationship with porosity, was improved from 50.1% to 56.5%.

To achieve a fine microstructure with high transparency, it is necessary to lower the sintering temperature, but unexpectedly non-uniform sintering behavior occurred. Although the investigation of non-uniform sintering behavior through microstructural and spectroscopic analysis was successfully conducted, the sintering temperature could not be significantly lowered. As an alternative for the fine microstructure, a two-step profile was applied to the SPS process. Through the two-step profile, the SPS process was divided into the first-step and the second-step to suppress the microstructure coarsening and may achieve sufficient densification. A two-step SPS was applied to the transparent Y_2O_3 and $RE_3Al_5O_{12}$ ceramics to achieve worthful improvement in transparency and microstructure control. As a result, the SPS process with high efficiency in densification using an electric field was successfully applied to transparent ceramics, and meaningful results were obtained that simultaneously achieve excellent optical transparency and microstructure control. In the future, it is expected to make a positive contribution to improving and optimizing the FAST processes such as SPS and FS.

Research Achievements

1. List of published papers

[1] **J.H. Lee**, B.N. Kim, J.G. Li, C.A.J. Fisher, and B.K. Jang, “Fabrication of transparent Ce^{3+}-doped $(Gd,Lu)_3Al_5O_{12}$ ceramics by two-step spark plasma sintering”, Journal of the European Ceramic Society, (2021) in preparation.

[2] **J.H. Lee**, B.N. Kim, and B.K. Jang, “Fabrication of highly transparent Y_2O_3 ceramics by two-step spark plasma sintering”, Journal of the American Ceramic Society, 104 (2021) 5501–5508.

[3] **J.H. Lee**, B.N. Kim, S. Hata, and B.K. Jang, “Microstructural and spectroscopic analysis in non-uniform Y_2O_3 ceramics fabricated by spark plasma sintering”, Journal of the Ceramic Society of Japan, 129 (2021) 66–72.

[4] **J.H. Lee**, J.G. Li, B.N. Kim, Q.H. Meng, X.D. Sun, and B.K. Jang, “Effect of annealing on microstructure and luminescence characteristics in spark plasma sintered Ce^{3+}-activated $(Gd,Lu)_3Al_5O_{12}$ garnet ceramics”, Journal of the European Ceramic Society, 41 (2021) 1586–1592.

[5] **J.H. Lee**, B.N. Kim, and B.K. Jang, “Non-uniform sintering behavior during spark plasma sintering of Y_2O_3”, Ceramics International, 46 (2020) 4030–4034.

[6] B.K. Jang, **J.H. Lee**, and C.A.J. Fisher, “Mechanical properties and phase-transformation behavior of carbon nanotube-reinforced yttria-stabilized zirconia composites”, Ceramics International, 47 (2021) 35287–35293.

[7] **J.H. Lee**, Y.J. Lee, Y.H. Han, D.G. Shin, S.Y. Kim, and B.K. Jang, “Microstructural studies of core/rim structure of polycarbosilane-derived SiC consolidated by spark plasma sintering”, Ceramics International, 45 (2019) 12406–12410.

2. List of international academic conferences

[1] **J.H. Lee**, and B.K. Jang, "Densification Behavior of Transparent Y_2O_3 Ceramic in Two-Step Spark Plasma Sintering", IEICES-2021 (International Exchange and Innovation Conference on Engineering & Science), Kyushu University, Kasuga, Japan, 10/21–22 (2021).

[2] **J.H. Lee**, B.N. Kim, and B.K. Jang, "Qualitative Analysis on Non-Uniform Sintering Behavior of Y_2O_3 Fabricated by Spark Plasma Sintering", ICC 8 (8th International Congress on Ceramics), Online Conference, 04/25–30 (2021).

[3] **J.H. Lee**, and B.K. Jang, "Sintering Behavior in Polycarbosilane-Derived SiC Ceramics", ICC 8 (8th International Congress on Ceramics), Online Conference, 04/25–30 (2021).

[4] **J.H. Lee**, B.N. Kim, S. Hata, and B.K. Jang, "Contamination of carbon and carbonate phases during spark plasma sintering in non-uniformly sintered Y_2O_3 ceramics", ICACC 2021 (45th International Conference and Expo on Advanced Ceramics and Composites), Online Conference, 02/08–11 (2021).

[5] **J.H. Lee**, J.G. Li, B.N. Kim, and B.K. Jang, "Effect of Carbon Contamination on Luminescent Characteristics During Spark Plasma Sintering of Ce^{3+}:$(Gd,Lu)_3Al_5O_{12}$", The 22nd CSS-EEST (Cross Straits Symposium on Energy and Environmental Science and Technology), Online Conference, 12/02–03 (2020).

[6] **J.H. Lee**, J.G. Lee, B.N. Kim, B.K. Jang, "Relationship between carbon contamination and luminescent characteristics in spark plasma sintered Ce^{3+}:$(Gd,Lu)_3Al_5O_{12}$", The 5th Asian-APC (Asian Applied Physics Conference), Online Conference, 11/28–29 (2020).

[7] **J.H. Lee**, B.N. Kim, and B.K. Jang, "Characterization on Matter Diffusion and Microstructural Evolution of Y_2O_3 Fabricated by Spark Plasma Sintering", PACRIM 13 (The 13th Pacific Rim Conference of Ceramic Society), Okinawa Convention Center, Okinawa, Japan, 10/27–11/1 (2019).

[8] **J.H. Lee**, B.N. Kim, and B.K. Jang, "Non-homogeneous Sintering Behavior of Y_2O_3 Ceramics", IEICES-2019 (International Exchange and Innovation Conference on Engineering & Science), Kyushu University, Kasuga, Japan, 10/24–25 (2019).

[9] **J.H. Lee**, B.N. Kim, and B.K. Jang, "Effects of mold materials and heating rate on transparent Y_2O_3 fabricated by spark plasma sintering", UNITECR 2019 (United International Technical Conference of Refractories), Pacifico Yokohama, Yokohama, Japan, 10/13–16 (2019).

[10] **J.H. Lee**, Y.J. Lee, D.G. Shin, S.Y. Kim, and B.K. Jang, "Microstructural evolution of polymer precursor-derived SiC on Core/Rim Structure", ICACC 2019 (43th International

Conference and Exposition on Advanced Ceramics and Composites), Hilton Daytona Beach Oceanfront Resort, U.S.A., 1/27–2/1 (2019).

[11] **J.H. Lee**, Y.J. Lee, D.G. Shin, S.Y. Kim, and B.K. Jang, "Effect of liquid phase SiO_2 on the densification of polycarbosilane-derived SiC ceramics", CSS-EEST 20 (Cross Straits Symposium on Energy and Environmental Science and Technology), Haeundae Grand Hotel, Busan, Korea, 11/26–28 (2018).

[12] **J.H. Lee**, Y.J. Lee, H.M. Lee, T. Nishimura, Y.H. Han, D.G. Shin, S.Y. Kim, and B.K. Jang, "Study on the discrepancy of sintering behavior in polycarbosilane-derived SiC ceramics", KJ-Ceramics 35 (Korea-Japan International Seminar on Ceramics), Lakai Sandpine Resort, Gangneung, Korea, 11/21–24 (2018).

[13] **J.H. Lee**, and B.K. Jang, "Effect of Liquid Phase SiO_2 on the Densification of Polycarbosilane-derived SiC Ceramics without Additives", KJMST 2018 (Korea-Japan International Symposium on Materials Science and Technology), The Ocean Resort, Yeosu, Korea, 11/7–9 (2018). **[Best Presentation Awards]**

3. List of domestic academic conferences

［1］ 李址煥、金炳男、張炳國、“The influence of two-step spark plasma sintering on optical and luminescent properties in transparent $Ce^{3+}:(Gd,Lu)_3Al_5O_{12}$ ceramics”日本セラミック協会 第34回秋季シンポジウム、オンライン開催、9/1-3 (2021)。

［2］ 李址煥、金炳男、張炳國、“2段階放電プラズマ焼結法によって製作された透明 Y_2O_3 セラミックス”日本材料科学会、2021 年度学術講演大会、慶應義塾大学 日吉キャンパス 来往舎、05/20-21 (2021)。

［3］ 李址煥、金炳男、張炳國、“Fabrication of highly transparent Y_2O_3 ceramics by spark plasma sintering with two-step pressure and heating profile”日本セラミックス協会 2021 年年会、オンライン開催、03/23-25 (2021)。

［4］ 李址煥、李紙光、金炳男、張炳國、“放電プラズマ焼結で作られた $(Gd,Lu)_3Al_5O_{12}$ ガーネットにおける炭素汚染が光学および発光特性に及ぼす影響”日本セラミックス協会九州支部 2020 年度秋季研究発表会、オンライン開催、11/14 (2020)。

［5］ 李址煥、波多聰、森田孝治、金炳男、張炳國、“Microstructural study on non-uniformly sintered Y_2O_3 by spark plasma sintering”粉体粉末冶金協会 2020年度秋季大会、オンライン開催、10/27-29 (2020)。

［6］ 李址煥、金炳男、張炳國、“Microstructural and spectroscopic analysis for the carbon and carbonate in spark plasma sintered Y_2O_3”日本セラミック協会 第33回秋季シンポジウム、オンライン開催、9/2-4 (2020)。

［7］ 李址煥、李紙光、金炳男、張炳國、“Improvement of luminescence characteristics in $Ce^{3+}:(Gd,Lu)_3Al_5O_{12}$ garnet fabricated by spark plasma sintering after annealing”日本材料科学会、2020年度学術講演大会、機械振興協会 機械振興会館、7/16 (2020)。

［8］ 李址煥、李紙光、金炳男、張炳國、“Microstructure and luminescence characteristics by annealing in spark plasma sintered Ce^{3+}-activated $(Gd,Lu)_3Al_5O_{12}$ garnet”日本セラミック協会 2020 年年会、明治大学、3/18-20 (2020)。

［9］ **李址煥**、張炳國、“Microstructural evolution of polymer precursor-derived SiC fabricated by spark plasma sintering”日本材料科学会、2019年度学術講演大会、関東学院大学 5/23-24 (2019)。

［10］ **李址煥**、金炳男、張炳國、“Effects of heating rates and holding times on sintering uniformity in spark plasma sintered transparent yttria”日本材料科学会、2019年度学術講演大会、関東学院大学 5/23-24 (2019)。

［11］ **李址煥**、金炳男、張炳國、“Non-homogeneous sintering behavior during spark plasma sintering of yttria”日本セラミック協会2019 年年会、工学院大、3/24-26 (2019)。

Acknowledgments

I would like to express my sincere gratitude to Prof. Byung-Koog Jang as an advisor at Kyushu University, who put a lot of energy and effort into research, life, and faith life guidance to receive a Ph.D. successfully. My professor's guidance was something I had never received anywhere else, and it was by far the best. In a limited time during the doctoral course, guidance on how to efficiently plan the experiments and write the academic papers not only helped me grow but also gave me respect for Prof. Jang. In addition, it was an opportunity to grow as a doctoral student and a member of society through a firm mindset and overall personal education in leading the doctoral program. Thanks to the professor's constant guidance with passion and effort, I have learned a lot, and I am grateful that I could grow. As a result, I achieved significant research achievements and graduated proudly, leading to a post-doctoral fellowship.

I'd like to thank Prof. Satoshi Hata for his generous teaching and support regarding the TEM analysis and academic discussion. Through the analysis and discussion with Prof. Hata, I could understand more deeply and derive clear conclusions about the evolution of non-uniform microstructure during the SPS process. I'd like to express my deep appreciation to Prof. Satoshi Hata and Prof. Kengo Shimanoe for their informative comments and guidance as to the thesis committee despite their busy schedule.

During the NIMS dispatch research, Dr. Byung-Nam Kim as supervisor helped me successfully lead my own research theme with experimental support and academic discussion. As a supervisor, he genuinely guided me not only with basic assistance but also with fundamental questions and sometimes clear solutions to my research. I would like to thank Dr. Li who was provided with $Ce^{3+}:(Gd,Lu)_3Al_5O_{12}$ powder and helped lead the research theme through detailed discussion of the powder preparation process. I'd like to thank Dr. Je-Deok Kim, and Dr. Koji Morita helped me with experimental supports. Dr. Koji Morita considered

me to applying for the NIMS Post-doctoral Fellowship. Although definitive results have not been announced, I also learned and felt a lot in applying. Dr. Craig A.J. Fisher at Japan Fine Ceramics Center (JFCC) helped proofread the submitted academic papers in English, and I was able to learn a lot about deriving the conclusions and writing the papers.

In campus life, due to the kindness of Ms. Rumiko Ide and Ms. Kyoko Nozoe at the major office, I was able to communicate without difficulty in administrative procedures. I’m deeply grateful to Korean fellows in the Chikushi campus, particularly Seung-Hyeon Kim, Hwa-Jeong Seo, Ahrong Jeong, Hyeong-Seok Yi, Sung-Jin Kim, Sang-Won Seo, and Su-Hyeon Baek. I have enjoyed my campus life with their kind endurance and assistance.

Most of all, I’d like to express my infinite gratitude to my parents for their infinite care and support during Ph. D. course. As a Ph.D. in Materials Science and Engineering, my father (Dae-Yeol Lee) always suggested wonderful and worthful paths for me, and my mother (In-Ja Cho)'s frugal and devoted care will never be forgotten. Also, there were many ordeals for my younger brother (Ji-Bum Lee) but seeing him persevere and overcome it was able that I hold on to the will to endure to the end. I love you always, and the future will be full of only happy days.

I sincerely thank everyone for their consideration and kindness, and I will never forget them. Finally, for 3 years and 6 months, I will never forget the study, research, and academic activities at the Chikushi Campus. It was a very valuable and precious period in my life. I am very proud to have graduated at the Chikushi Campus in Kyushu University.

January, 2022

李 址煥

LEE JI HWOAN